Finite Element Assisted Prediction of Ductile Fracture in Sheet Bulging of Magnesium Alloys

David Hunt

ID: 9973189

Submitted in Fulfilment of M.Eng Thesis

Supervisor Dr. Bryan MacDonald

September 2008

Declaration

I hereby certify that this material, which I now submit for assessment on the programme of study leading to the award of Masters in Engineering (M.Eng) is entirely my own work, that I have exercised reasonable care to ensure that the work is original, and does not to the best of my knowledge breach any law of copyright, and has not been taken from the work of others save and to the extent that such work has been cited and acknowledged within the text of my work.

Signed: _____ (Candidate) ID No.: _____

Date: _____

Acknowledgements

I would like to express my gratitude to Dr. Bryan MacDonald for all his guidance and support during this work. I would also like to thank the members of staff in the School of Engineering, in particular Mr. Liam Domican and Mr. Chris Crouch.

I also wish to thank Mr. Damien Comiskey and Mr. Emmet Galvin for all their advice and feedback on the finite element model. Lastly I would like to thank my family and friends for all their support and encouragement throughout my time at DCU.

Finite Element Assisted Prediction of Ductile Fracture in Sheet Bulging of Magnesium Alloys

David Hunt B.Eng

ABSTRACT

There is currently a growing demand for energy efficiency, particularly in reducing the rate of oil consumption. One solution in this area is for the aerospace and automotive industries to produce lighter vehicles that are more fuel efficient. Magnesium alloys provide that solution as they have a high strength to weight ratio and can contribute to reducing the overall weight of the vehicle. Over the past few years many researchers have tried shaping these alloys using various forming techniques. These studies have shown however, that the formability of these alloys is very difficult to predict. The material properties of magnesium alloys would suggest that they are ideal for sheet metal forming, yet their formability is still inferior to many other alloys used in sheet metal forming. In order to overcome this unpredictability in shaping Mg alloys it is necessary to introduce a range of failure that will predict fracture over a range of draw depths rather than a single depth. It is difficult to make the leap from a process that is unpredictable to pinpointing the exact point of failure. It is more logical to firstly determine a range of formability where failure can occur. In this study a Finite Element Model of a sheet bulging process was built and validated with results obtained from physical testing. The FEA model uses Oyane's ductile fracture criterion to predict whether fracture has occurred in the material and also to predict the location of fracture if it occurs. This validated FEA model implements a failure range where failure is predicted over a range of draw depths, and sensitivity analysis provides a confidence level in this range by varying some of the material properties and examining the effects on the prediction of fracture.

Contents

Nomenclature

Symbol	Definition	Dimension
a	Oyane Constant	-
A	Material Constant	-
b	Oyane Constant	-
B	Strain displacement matrix	-
BHF	Blankholder Force	kN
BHP	Blankholder Pressure	MPa
c	Sonic wave propagation velocity	m/s
C	Material Constant	-
C	Global Damping Matrix	-
D	Material Constant	-
D	Damage Level	-
e	Engineering Strain	-
E	Young's Modulus	GPa
F	Force	N
H	Displacement Interpolation Matrix	-
I	Oyane's Integral	-
I	Identity Matrix	-
K	Global Stiffness Matrix	-
K	Bulk Modulus	-
L	Element characteristic length	m
m	Strain rate sensitivity coefficient	-
M	Global Mass Matrix	-
n	Strain hardening coefficient	-
P	Plastic modulus	-
r	Anisotropic parameter	-
R	Load Vector	-
R	Anisotropic hardening parameter	-
s	Engineering Stress	Pa
t_0	Initial blank thickness	mm
t	Time	seconds
T	Temperature	° Celsius
T	Period	-
U	Virtual Displacement	m
v	Element volume	m^3
w	Width of tensile sample	mm
$\bar{x}$	Mean	-

Greek		
a	Mass Damping Constant	-
b	Stiffness Damping Constant	-
e	Strain	-
s	Stress	MPa
s	Standard deviation	-
k	Viscous coefficient	-
r	Density	kg/m^3
t	Shear stress	MPa
m	Coefficient of friction	-
u	Poisson's ratio	-
Subscript		-
cr	Critical	-
d	Dynamic	-
eqv	Equivalent	-
f	Fracture	-
h	Hydrostatic	-
min	Minimum	-
max	Maximum	-
p	Plastic	-
o,y	Yield	-
s	Static	-
S	Surface	-
V	Volume	-
Superscript		
Eff	Effective	-
i	Points in space	-
t	Time	Seconds
B	Body	-
S	Surface	-
T	Transpose of a matrix	-
-	Equivalent	-
*	Triaxiality ratio	-

List of Figures

Chapter 1: Introduction

1.1 Magnesium Alloy AZ31B-O

High strength magnesium alloys and their possible applications in the automotive and aerospace industry have been the focus of much attention in the research community in recent years. Their high strength to weight ratio has made them an ideal material for industries which must constantly strive to improve fuel efficiency. The use of magnesium alloy parts would result in weight savings of 33% and 77% compared to aluminium and steel respectively for the same volume of material used [1]. Replacing components made from these materials with magnesium alloys would result in lighter vehicles which consumed less fuel during use.

There are however some problems associated with these alloys, namely their low ductility at room temperature and unpredictability during forming. Generally magnesium alloys are formed at a temperature range of 100˚ – 400˚C, where their ductility improves, but forming material at high temperatures incurs its own set of problems, the main issue of which is maintaining a constant temperature throughout the forming process. The material properties of the alloy also vary with increasing temperature and thus require material testing at each temperature to determine them, and from an industrial point of view this testing will incur more costs. Despite these problems, the benefits of using magnesium alloys rather than aluminium outweigh the extra costs involved in testing and forming. Research into improving the formability of magnesium alloys has received large financial backing.

Magnesium AZ31, which is currently investigated in this research, is a wrought magnesium alloy that consists of several other metals such as aluminium, zinc, copper, nickel and iron. The composition of AZ31 is shown in Table 1.1 while some mechanical and thermal properties of the material are sown in Table 1.2.

Table 1.1: Magnesium Alloy AZ31B Composition [2]

Element	Mg	Al	Ca	Mn	Zn	Cu	Fe.	Ni	Si.	Other
%	Bal.	2.5-3.5	0.04 max.	0.20 – 1.0	0.7-1.3	0.05	0.005	0.005	0.05	0.30

Table 1.2: Mechanical and Thermal Properties of AZ31 [3]

Material Properties AZ31	
Young's Modulus (GPa)	45
Yield Stress (MPa)	150
Tensile Strength (MPa)	250
Density (Kg/m^3)	1660
% Elongation at Fracture	10
Melting Temperature (°C)	605 - 630
Thermal Conductivity W/m-k	96

1.2 The Sheet Bulging Process

Sheet bulging generally refers to sheet metal forming processes that produce spherical bulges in sheet metal products. The use of the term "sheet bulging" in literature has been ambiguous. Wang et al. [4] refer to sheet bulging as a process involving viscous pressure to shape the material, while Namoco et al. [5] describe sheet bulging as a process where the material is formed using a spherical punch. This study uses the latter definition of this term.

The sheet bulging process is a widely used industrial process that is used to produce parts of complex and seamless geometries. Components are formed by constraining a blank around the entrance of a die with a blank holder and then forcing the blank into the die using the rounded punch. The shapes of parts formed by this process are axisymmetric with dome shaped profiles similar to that of the punch.

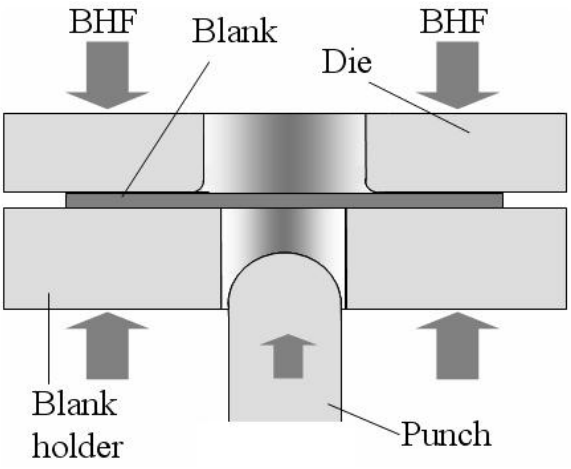

Figure 1-1: Overview of the Sheet Bulging Process

Sheet bulging is very similar to deep drawing with the major difference being the punch profiles. The draw depths achievable by both processes are limited by the same factors such as drawing ratio, onset of necking, wrinkling and fracture. Both are greatly influenced by the blank holder pressure exerted on the blank during forming. There is no great advantage of using sheet bulging over deep drawing as the processes are very similar, preliminary work in this study found little difference in terms of the stresses and strains involved in the two processes. The deciding factor in choosing which process to use is the geometry of the required piece.

1.3 Ductile Fracture Criteria

The objective of this study was to analyse sheet bulging both experimentally and numerically using LS-DYNA and implement Oyane's ductile fracture criterion [6]. This criterion is derived from plasticity theory for porous metals and is based on the macroscopic stress and strain during forming. The results of the finite element simulation contain the stress and strain histories of the material and inputting these values into the criterion will show the evolution of fracture throughout the material at each step of the process. The empirical hypothesis of the ductile fracture criteria is that fracture occurs where the damage done to the material exceeds a pre-determined critical damage value (CDV). Han and Kim [7] summarise these criteria as being of the form shown in Equation 1.1, where they are expressed in terms of an integral representing the effect of deformation history.

$$\int_0^{\bar{\varepsilon}_f} \textbf{F(process parameters) d}\varepsilon \textbf{ = CDV} \qquad (1.1)$$

Where $\bar{\varepsilon}_f$ is the equivalent strain at fracture and F is a function of the process parameters, usually an expression for stress or a stress ratio. The function is integrated with respect to the equivalent strain for each time step and the cumulative strain from every time step, or the strain history, is the total equivalent plastic strain. The equivalent strain has the greatest influence on the function and determines the rate at which it reaches the critical damage value (CDV) where fracture is predicted.

1.4 Statistical Methods

As previously stated the formability of magnesium can be unpredictable, especially at high temperatures over 200˚C, and so it is important to examine the effects of various changes in the mechanical properties and how they affect the draw depths at which fracture occurs. Material properties are generally listed as a range, not an individual value. All forming processes are performed to a degree of pre-defined set tolerances. These tolerances, like the range of material properties, provide a distribution of results. In finite element modeling however, the input parameters for material properties are singular values that will provide results for only one aspect of the formability of the material. The application of statistical methods in the finite element model will allow the study of variance in the formability of the magnesium alloy, and thus decrease the unpredictability surrounding its formability by defining a distribution of results rather than jumping ahead and seeking pin point accuracy.

Using probabilistic analysis, as outlined by Dar et al. [8], the material properties of the finite element model are defined as a statistical distribution of values rather than a singular value. The model is solved numerous times using various inputs from the distribution and the results of interest of the analyses are gathered and are defined in terms of their averages and standard deviations. From this, the confidence limits in the results can be obtained, and it can be stated with a 95% certainty, that any future

analysis randomly sampling an input from the distribution will produce results with the range determined by the confidence limits.

1.5 Project Objectives

The aim of this study was to achieve the following:

- Develop a finite element model of the sheet bulging process for magnesium AZ31 at 100 and 150 degrees Celsius.

- Implement a ductile fracture criterion that would accurately predict the depth and location of fracture.

- Determine a range of failure for magnesium alloys at each temperature to allow for variances in results from material and mechanical testing.

- Implement statistical methods that will provide a level of confidence in the range of failure determined by the finite element model.

- Hence, draw conclusions on the formability of AZ31 and make recommendations for successful forming.

1.6 Summary of Chapter 1

This chapter introduces magnesium alloy AZ31 and discusses its potential applications in the automotive and aerospace industries. Sheet bulging and its various definitions are also introduced and discussed. The basic theory behind fracture criteria and their numerical form are also briefly examined. The need for statistical analysis in the prediction of fracture is outlined, and the implementation of confidence limits to determine a range of response from various inputs has been discussed.

Chapter 2: Literature Review

2.1 Introduction

This chapter examines some of the current research trends in magnesium alloys and ductile fracture criteria. Brief descriptions of some specific papers are given and their influence on this current study is outlined. This review builds a foundation of modeling principals for use in the current finite element simulation. It was hoped that by examining the papers reviewed here, several new concepts could be developed to implement in this current work and provide some original and innovative insight into this field.

2.2 Magnesium Alloys

2.2.1 Material Properties and Potential Applications

Magnesium alloys have been the subject of numerous research projects throughout the world in recent years. Due to its lightweight and specific strength, magnesium alloys are widely used for structural components in the aerospace, electronics and automotive industry to replace some existing parts [9, 10]. Although the principal manufacturing process for magnesium alloys is die casting, the development of alloys such as AZ31 have improved the potential use of press forming [11]. Due to their hexagonal closely packed crystal structure however, magnesium alloys have low ductility at room temperature and require high temperatures to increase ductility and formability [12-16].

The US government commissioned a report [17] in the nineties on the potential applications of magnesium alloys in passenger vehicles. The research carried out in the Centre for Transportation Research at Argonne National Laboratory in the US examines thoroughly the characteristics of magnesium and its alloys as well as their strengths and weaknesses. The research is aimed purely at assessing the suitability of magnesium for use in the automotive industry. The positive aspects, as well as the

potential obstacles of using magnesium in industry were examined. The following are some notable observations made in the report:

Magnesium is 36% lighter per volume than aluminium and 78% lighter than iron and steel. When alloyed, magnesium has one of the highest strength to weight ratio of all structural metals. There are also other properties of magnesium, such as its coefficient of thermal conductivity, which can have a negative affect on its formability at high temperatures. Table 2.1 compares material data for magnesium alloy AZ31, aluminium 2024, iron and mild steel obtained from the material properties database, Matweb [3]. The figures in this table support the observations in the Argonne report [17].

Table 2.3: Comparison of Material Properties [3]

Material Properties	AZ31	Al 2024	Iron	Mild Steel
Density (kg/m^3)	1770	2780	7870	7870
Weight Saving Per Unit Volume (%)	-	36	77.5	77.5
UTS (MPa)	255	186	540	420
Ratio of Strength to Weight Per Unit Vol	144068	66906	68615	53367
Hardness - Brinell	56	47	146	121
Melting Point (˚C)	630	630	1535	1515
Thermal Conductivity (W/m-k)	96	193	76.2	52
Thermal Expansion (/˚C)	25.2	23.6	11.7	12

Magnesium is very reactive and the application of coatings would be required in its natural state. Magnesium alloys form a hydroxide layer when exposed to the atmosphere. This layer is vulnerable in acidic or neutral conditions but quite stable under alkaline conditions [18], which means that even under normal atmospheric conditions dissolution of the alloy can occur. It is necessary therefore to apply a coating to the surface of the alloy to reinforce this oxide film. Anodising is one of the most common procedures to reinforce the native oxide films and therefore improve the corrosion resistance of the magnesium alloy [18-20]. This method improves corrosion resistance by depositing a thin film over the oxide layer. Some of these films are obtained from treating the alloy in a solution containing rare earth salts [21]. Rudd et al. [22] found that treating the magnesium with salt films such as cerium, lanthanum and praseodymium reduced the effects of corrosion. These findings were supported by Montemor et al. [23].

Magnesium has a reputation for being highly flammable at temperatures above 478°C [1], and thus its safety in use is often questioned, however because of its high heat conductivity only small chips and shavings can sustain combustion and components with thicknesses greater than 3mm would cease burning as soon as the source of heat was removed [17]. As the range of temperatures used to form magnesium alloys are never high enough to cause combustion, this issue does not affect the forming process. The flammability of the material should not be a major cause of concern to the automotive industry as although thin strips of magnesium can be flammable above 478°C, gasoline and engine oil will ignite at a much lower temperature and therefore the flammability of magnesium parts in the vehicle would be inconsequential.

Table 2.2: Application of Magnesium Alloys in Auto Parts [25]

Application	Form	Mg Alloy
Bumper support beam	Extrusion	AZ31B
Steering-column support	Extrusion	AZ31B
Air-bag channel and end caps	Extrusion	AZ31B
	caps	AM60B
Two-way seat adjuster channel	Extrusion	AZ31B
Seat/channel guide	Extrusion	AZ61A
Electric-motor frame and bell ends	Extrusion	AZ31B
	Bell ends	AZ91D
Tubular bucket seat	Stamping	AZ61A
	Extrusion	AZ31B
Two-piece mini-spare	Stamped center	AZ31B
	Extruded rim section	AZ61A
X-ray cassette (2-piece folder)	Stamping	AZ31B
Valve cover	Deep drawn	AZ31B
Oil pan	Deep drawn	AZ31B
Battery tray	Stamping	AZ31B
Two-piece billet wheels	Spun rim	AZ61A
	Machined center	AZ61A
Forged wheel	Forging	ZK60A
Rolled rims	Formed sheet	AZ61A

Magnesium is in abundant supply; it is in fact the eighth most common element. Seawater is the main source of magnesium [17, 24] containing 0.13% Mg, which provides a vast resource of the element. There are manufacturing issues involving the high costs in purchasing and forming magnesium, but research and development in hot forming technology and superplastic forming could help ease these concerns. Any questions regarding magnesium's ability to withstand impact have proven to be

unfounded, as crash safety standards are maintained by magnesium alloy components [17]. Table 2.2 shows the application of magnesium alloys in various auto parts [25] and the forming processes required to produce them.

2.2.2 Forming Processes

The sheet bulging process used in this study is a relatively simple process. This work is more focused on the application of a ductile fracture criterion and statistical methods to improve the predictability of forming magnesium alloys in general, rather than optimising a specific process. This study aims to implement a fracture criterion that successfully predicts fracture in a simple sheet bulging process, and can then be used to predict fracture in more complex forming processes. There are currently numerous researches investigating more complex forming techniques of magnesium alloy sheets, many of which do not implement a ductile fracture criterion to predict failure.

One such method is the local heating and cooling technique. This was implemented by Yoshihara and MacDonald [26] to improve the formability of magnesium AZ31 in the deep drawing process. This method involves locally heating the blank flange to 300˚C while cooling the drawn cup wall directly by injecting water around the die. The temperature of the punch was also kept at room temperature using water. The finite element model divided the blank up into three temperature regions to simulate the temperature gradient in the blank. The physical results show a draw depth of 90mm can be achieved with this technique. The FEA model however predicted fracture at a depth of 52mm, which is a 42% deviation from the physical test result. No fracture criterion was implemented in the finite element model and fracture was determined from the Von Misses stress results. It can be concluded that without a ductile fracture criterion, it is very difficult to accurately predict fracture in a sheet metal forming process.

A variation of this work has also been conducted by El-Morsy and Manabe [27]. In this work there are two models, the first where the die and blank holder are heated to forming temperature while the punch is kept at room temperature. The second is

where the punch is also heated. The results found that when the temperature of the punch is maintained at room temperature there is no localised thinning in the blank and a greater cup height can be achieved. The formability of the magnesium was improved when the wall of the cup was cooled by the punch during forming. From this it was concluded that heat transfer has a strong effect on the final deformation profile of the drawn cup. The effects of punch speed were also examined with experiments conducted at three different speeds 135, 270 and 1350 mm/min. It was found that increasing the speed reduced the effects of heat transfer and so the benefits of this method were very limited at high speeds.

Superplastic forming is a process where sheet metal is forced into a die using gas induced pressure. In most cases Argon is the gas used in the process because of its nobility [28]. Under certain conditions some metallic alloys and ceramics display superplastic behaviour whereby they can achieve elongation of more than 100% without fracture. Even elongations of 5000% have been achieved [29]. Superplastic forming is used to produce parts with complex geometries in a single process and results in savings in material cost, machining and labour. This process would be the logical follow up to the work done in this project where the methods used to determine fracture in a simple process like sheet bulging, can be applied to superplastic forming, which is a similar but more complex process.

Draugelates and Schram [30] have undertaken research in the application of superplasticity in the forming of magnesium alloys. It was found that the productivity of the process is closely related to an increase in the forming velocity and a low formation temperature, which must be at least half the materials melting point. Samekto and Roll [28] also found discovered certain requirements for a successful superplastic forming process. The grain size must be fine and usually 10 m or less, and there must be a low and controlled strain rate, usually 10^{-4} to 10^{-2} per second.

Kumar et al. [31] concluded that the critical component in the superplastic process was the prediction of the final thickness distribution and the strain rate necessary to maintain superplasticity. The research involved bulge forming an aluminium alloy into a hemispherical die to produce a piece very similar in shape to that obtained in this current work. The results found that forming time decreased with increasing

pressure, as expected. There was also thinning at the centre of the blank as the bulge was formed and this was supported by FEA. Interestingly the initial strain rate was found to decrease at the start of the process but as the process continued it rose uniformly.

Superplasticity although being very attractive for industrial use also has disadvantages. Liew et al. [32] investigated the growth of cavities during the superplastic process. Cavity formation can lead to degradation of material properties such as tensile, creep, fatigue and stress corrosion behaviour [33-37]. Liew et al. [32] found that the damage caused by cavity growth increases with increasing strain and can result in early failure.

The forming processes previously outlined are just some of the complex forming processes that can be used to shape sheets of magnesium alloy AZ31. The methods involved in applying a ductile fracture criterion, failure range and probabilistic analysis to the current finite element model are generic and can be applied to more complex forming processes such as superplastic or incremental forming. The investigations into heat transfer have also concluded that superior formability can be achieved by keeping the punch at room temperature rather than heating it to the forming temperature. The work of Yoshihara and MacDonald [26] and El-Morsy and Manabe [27] verify this principal and so the punch was kept at room temperature during the physical testing in this current work.

2.3 Ductile Fracture Criteria

The idea of ductile fracture criteria to predict failure in a material has been around for the past fifty years since Freudenthal [38] derived a generalised plastic work criterion based on Von Mises stress and strain. With recent advances in numerical analysis, particularly in the finite element method, the use of ductile fracture criteria to predict the occurrence of fracture have become popular. The most common FEA programs incorporate accurate criteria for predicting yield, such as Von Mises, but do not provide a means for predicting or locating fracture. This provides the research community the need to investigate the various fracture criteria currently available

and to associate each one with the process that it is most suited to. This section examines the usefulness and relevance of some of the work currently being carried out. It is hoped that by studying current research trends some short comings may be unearthed and alternative solutions may be offered in this study.

There have been many ductile fracture criteria proposed over the years, several of which are based on the void growth relation reported by Rice and Tracey [39]. These include Cockcroft and Latham [40], who proposed a criterion that is based on the total plastic work per unit volume:

$$I = \int_0^{\bar{\varepsilon}_f} \sigma_{\max} \partial \bar{\varepsilon} = C_1 \tag{2.1}$$

Where σ_{max} is the maximum principal stress, $\bar{\varepsilon}$ is the equivalent strain and C_1 is a material parameter.

Clift et al. [41] proposed a criterion which differs slightly from Cockcroft and Latham by using an equivalent stress, $\bar{\sigma}$, rather than the max tensile stress.

$$I = \int_0^{\bar{\varepsilon}_f} \bar{\sigma}\, \partial \bar{\varepsilon} = C_2 \tag{2.2}$$

Oyane et al. [6] proposed a criterion which is derived from plasticity theory for porous materials

$$I = \int_0^{\bar{\varepsilon}_f} \left(\frac{\sigma_h}{\bar{\sigma}} + C_3\right) \partial \bar{\varepsilon} = C_4 \tag{2.3}$$

Where σ_h is the hydrostatic stress, $\bar{\sigma}$ is equivalent stress, $\bar{\varepsilon}$ is the equivalent strain and C_3 and C_4 are material parameters.

Others have modified existing fracture criteria to create their own criterion. Brozzo et al. [42] created a criterion which is a modified version of Cockcroft and Latham (Equation 2.1) and takes hydrostatic pressure into account:

$$I = \frac{2}{3}\int_0^{\bar{\varepsilon}_f} (1 - \frac{\sigma_h}{\sigma_{\max}})^{-1} \partial\bar{\varepsilon} = C_5 \tag{2.4}$$

Han and Kim [7] also took the Cockcroft & Latham criterion and combined with the maximum shear stress criterion [43] to form their own criterion.

$$I = \int_0^{\bar{\varepsilon}_f} \sigma_{\max}\ d\bar{\varepsilon} + A_1\tau_{\max} + A_2\varepsilon_t = A_3 \tag{2.5}$$

Many modified criteria are created with a specific process or material in mind. Yang and Yu [44] employed their own criterion specifically to evaluate the formability of automotive aluminium sheets. One can argue the case that a new criterion may not be the solution, that the problem may actually be the method used to implement the recommended criterion for the process. Credibility can be at stake if the general consensus is that an author has created a new criterion because the tried and trusted criterion has not validated his or her results.

There is also the aspect of the implementation of the research findings in industry. Each criterion has a number of material constants associated with it and various material tests have to be carried out to determine them. From an industrial point of view, it is vital that the number of material constants is minimised to reduce costs and time in material testing for each constant. Dey et al. [45] work on the projectile impact of steel plates was based on this concept and examined how a complex fracture criterion, in this case a modified Johnson – Cook [46] , which consists of five material parameters compared to the results obtained from Cockcroft and Latham, which is a single parameter criterion. The modified Johnson – Cook criterion is based on damage evolution where fracture occurs when the damage level, D reaches unity.

$$D = \sum \frac{\Delta \varepsilon_{eq}}{\varepsilon_f} \leq D_C = 1 \tag{2.6}$$

where $\Delta\varepsilon_{eq}$ is the increment of the accumulated (equivalent) plastic strain.

The strain rate and temperature effects are taken into account when determining the fracture strain.

$$\varepsilon_f = (D_1 + D_2 \exp(D_3 \sigma^*))(1 + \varepsilon_{eq}^*)^{D_4} (1 + D_5 T^*) \tag{2.7}$$

where $D_1, \ldots, D_5$ are material constants determined from material tests, $\sigma^* = \sigma_H/\sigma_{eq}$ is the stress triaxiality ratio and T^* is the homologous temperature.

Several studies on metals [46-51] show that failure strain increases with temperature and decreases with increasing strain rate. This is why more advanced criteria such as Johnson – Cook are required in order to include other aspects of the material behaviour, such as the effects of strain rate and temperature. The results from Dey et al. [45] show that both criteria accurately predicted fracture in the plates and in this case it was unnecessary to use the more complex fracture criterion. There is a question of a trade off in terms of accuracy of a criterion compared to its number of material parameters. It is possible that a simpler yet less accurate criterion could be incorporated by a manufacturer and a range, or statistical confidence level in its performance could be associated with its results.

Current research shows that ductile fracture criteria are employed in a wide range of material processes. Goijaerts et al. [52] applied various criteria to predict failure in a metal blanking process. The aim was to show that the material constants associated with each criterion could be determined from the actual forming process itself and not from the usual methods such as tensile tests. This would then provide more accurate results from the criteria, but would be more expensive from an industrial point of view. Takuda et al. [53] successfully implement Oyane's criterion to predict fracture in bore expanding of sheet metals as shown in Figure 2-1, where C.P., H.P. and F.P. indicate conical, hemispherical and flat-headed punches, respectively.

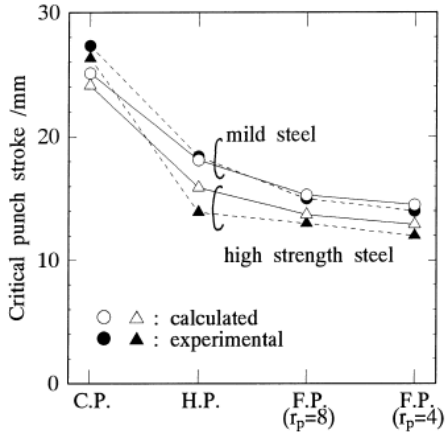

Figure 2-1: Bore Expanding Results from Takuda et al. [53]

Takuda has also implemented fracture criteria in a finite element analysis of a deep drawing process [54]. The main trend however in the application of fracture criteria appears to be in forming limit curves (FLC) of sheet metals.

2.3.1 Forming Limit Diagrams

Forming limit diagrams (FLD's) are commonly used in evaluating the formability of sheet metals [55]. Since Keeler and Backofen [56] introduced the concept of forming limit diagrams in 1963 it has been a widely accepted criterion for fracture prediction in sheet metal forming [57]. Keeler collected data on principal strains at the onset of fracture from stamping and biaxial stretching experiments. From this data Keeler concluded that the major principal strain was a function of the minor principal strain, and plotted values of major strain against minor strain to create the forming limit diagram. Goodwin [58] extended this work to include values where the minor principal strain is negative. The diagram obtained was termed the Goodwin-Keeler Forming limit diagram and is the most common FLD in use today and is shown in Figure 2-2, while a more simple explanation of the regions of the diagram is shown in Figure 2-3. The FLD for a particular material is a graphical representation of the limits of principal strain, which it may undergo without failure, during forming. The criteria of failure are wrinkling, localised necking and fracture [59]. Forming limit curves (FLC) can be made to the onset of necking (FLCN) or progress all the way to fracture (FLCF).

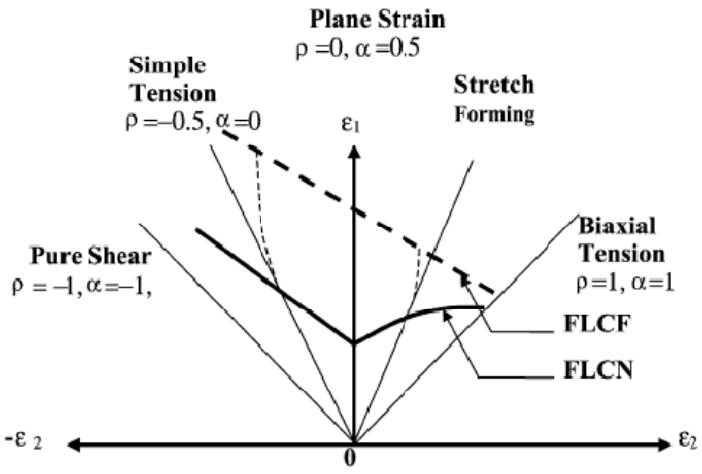

Figure 2-2: Forming Limit Diagram [7]

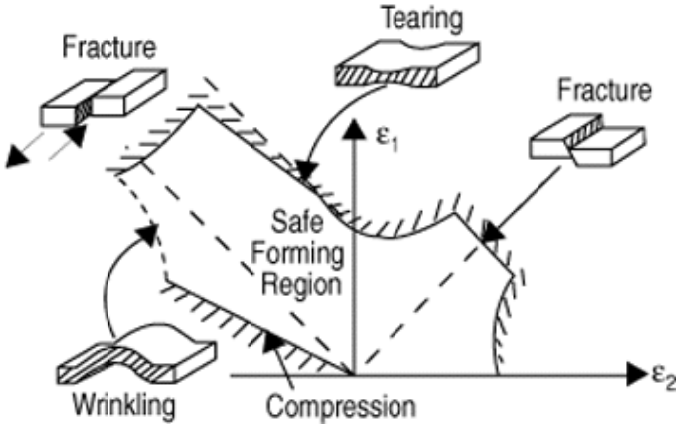

Figure 2-3: Forming Limit Diagram Regions [60]

The formability of sheet metal is limited by localised strain along narrow bands. These bands grow into sharp necks along which fracture will occur [7]. In the case of materials with low ductility, fracture occurs without obvious necking phenomenon. Magnesium AZ31 has limited ductility unless heated and fractures suddenly without necking. Han and Kim [7] investigated the formability of various metal sheets with various ranges of ductility. The study found that the sheets of high ductility produced FLCs that were linear while the sheets that had low ductility resulted in FLCs that were complex. The application of fracture criteria accurately predicted the failure of the linear FLCs but none could accurately match the FLCs for the complex ones. It was found that a modified ductile fracture criterion was required to correctly analyse

the FLCs of both linear and complex materials. A new fracture criterion, as shown previously in Equation 2.5, was derived which was a combination of Cockcroft and Latham and the maximum shear stress criterion and was successful in predicting fracture for both shapes. This view was also shared by Ozturk and Lee [55] although that work did not derive a suitable fracture criterion.

Chen et al. [57] performed biaxial stretching tests using a semi-spherical punch on sheets of magnesium alloy AZ31 at 100˚C, 200˚C and 300˚C. The engineering major and minor strains were measured at the locations of fracture and used to create the forming limit curves at each temperature as shown in Figure 2-4.

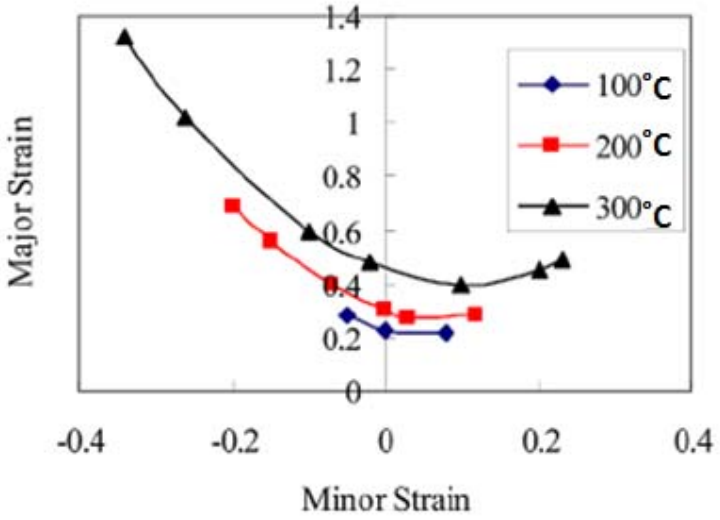

Figure 2-4: Forming Limit Diagram of AZ31 at 100˚C, 200˚C and 300˚C [57]

Generally the higher the position of the forming curve on the forming limit diagram the better the formability. Chen [57] concluded from the forming limit diagram that the formability of magnesium alloy AZ31 improved with increasing temperature. Chen supported this claim with results from tensile testing. Siegert et al. [61] also created a forming limit diagram for magnesium AZ31, as seen in Figure 2-5, at three different temperatures; 200˚C, 235˚C and 280˚C. Siegert's conclusions from the FLD diagram matched that of Chen [57] and reported that for a constant strain rate the formability of AZ31 improves with increasing temperature. Any attempt to compare the difference in terms of strain values obtained by Chen and Siegert is futile as both studies were carried out using different experimental conditions.

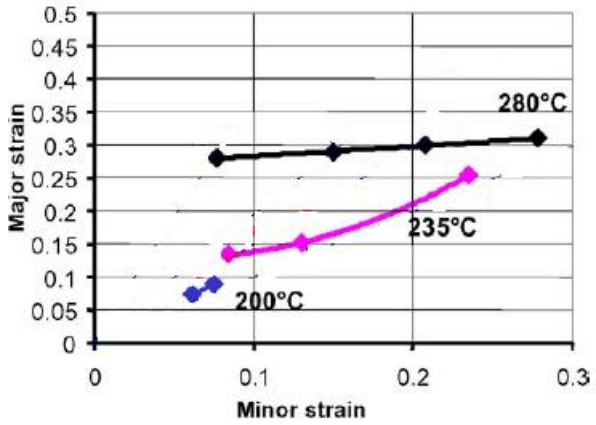

Figure 2-5: Forming Limit Diagram of AZ31 at 200˚C, 235˚C and 280˚C [61]

2.3.2 Takuda's Research into Ductile Fracture Criteria

Takuda et al. [54] has had some success in implementing ductile fracture criteria into sheet metal forming. This was one of the earliest examples of fracture criteria being implemented into the sheet forming process. Up to that point fracture criteria were only ever used to create forming limit curves. Takuda's work compares the Cockcroft and Latham, Brozzo, Oyane and Clift criteria in predicting fracture in various sheet metals and various ranges of ductility. The sheets were formed using deep drawing and the evolution of the fracture integrals during the draws were examined.

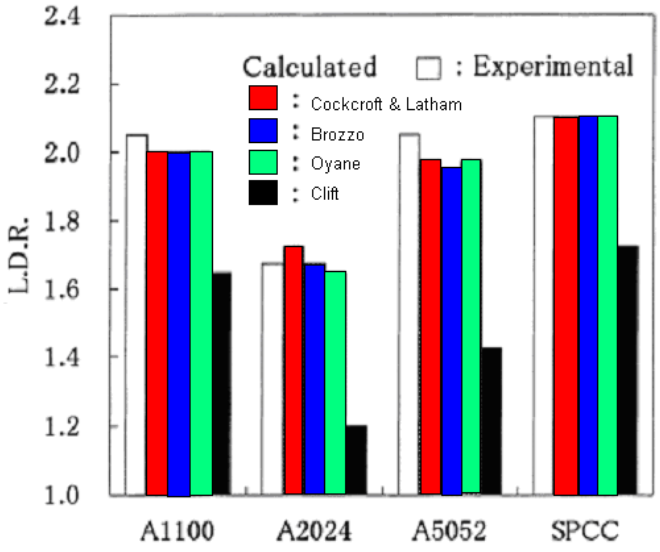

Figure 2-6: Results from Takuda et al. [54]

Figure 2-6 shows the comparison of FEA and experimental drawing ratios for the four materials using the four fracture criteria. Takuda usually represents his results graphically without elaborating on exact figures or percentages of error. The results showed that the Cockcroft and Latham, Brozzo and Oyane criteria provided good predictions even for aluminium sheets with low ductility, while the Clift criterion was unsuitable for predicting fracture in sheet metal forming.

Takuda has also investigated fracture prediction in magnesium AZ31 sheets for the deep drawing process [62]. By implementing Oyane's criterion, fracture was successfully predicted for a range of punch profiles. The most significant observation however is the comparison between the results obtained using different material constants for Oyane's equation. Tensile tests showed that the ductility of the material in the 90˚ direction to rolling was very small in comparison to the 0˚ and 45˚ directions. Traditionally tensile tests on anisotropic materials consist of samples being taken from 0˚, 45˚ and 90˚ and the average of these results are used as the material properties and constants. Takuda realised from the results that failure would occur sooner in the 90˚ direction due to the low ductility and the constants from these tensile tests were used in Oyane's equation. By comparing the two Oyane's integrals, one using the mean values and the other using the values from the 90˚ direction it was found that average values failed to predict fracture while the Oyane integral using the 90˚ values predicted fracture very accurately for each punch profile.

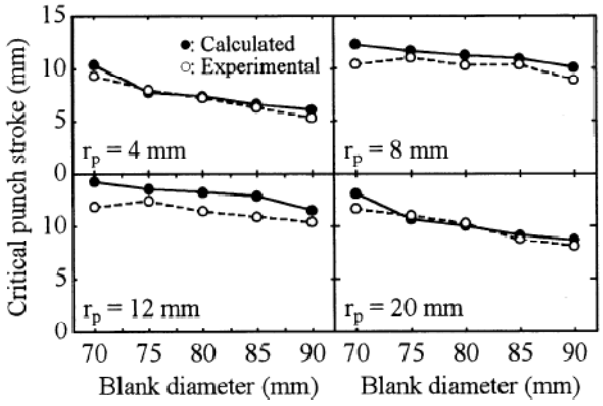

Figure 2-7: Results from Takuda et al. [62]

Figure 2-7 shows the comparison of Takuda's experimental deep drawing results and the FEA predicted values for various blank and punch geometries. It can be seen that

Takuda has once again successfully implemented Oyane's criterion and accurately predicted failure. Once again however, no percentage of error or confidence in the model is given.

There has been much focus on magnesium alloys by the Japanese auto industry and hence much impetus on Japanese researchers to predict failure in magnesium alloy forming. The Oyane criterion has generally been found by Japanese researchers to be the most accurate for predicting ductile fracture, and is used almost exclusively by them [63]. The research undertaken in this study integrates Oyane's criterion into a finite element model. From previous research [54] it was clear that a number of criteria were suitable, namely Oyane, Cockcroft and Latham and Brozzo. The reason Oyane's criterion has been chosen is mainly due to the fact that Takuda uses it so often in numerous studies. Whether its bore expanding of sheet metals [53], creating forming limit curves [64] or deep drawing of magnesium [62], Takuda has successfully implemented Oyane's criterion in sheet metal forming and has produced successful predictions of fracture.

Reviewing the results of the aforementioned papers it can be seen that the predicted fracture obtained from the finite element simulation is only ever compared to one set of physical test results. There are cases where numerous FEA and experimental results are compared under different conditions, but a set of FEA results is never compared to multiple results obtained experimentally. The reason this point is so important is because of the issue of repeatability. A finite element simulation will always produce the same results when run indefinitely if the same conditions are maintained throughout. A physical experiment will produce a range or distribution of results when carried out repeatedly. Therefore it is possible for an author to take one result from the set of experimental results, generally the one that compares most favourably to the FEA result and publish that comparison in a paper. This does not necessarily give a true representation of what is happening in the process. The finite element method is a numerical method that is an estimate of what occurs in reality, it is rarely 100% accurate. Takuda's work [53-54, 62,64] shows that the fracture criterion tends to over predict failure slightly. So failure can occur in reality while the FE model is on the threshold of fracture but not quite failed. To allow for this and the issue of repeatability this study incorporates a failure range where failure is detected

when the integral is between 0.9 and 1. Each experimental result from every set is accounted for and compared to the range of failure determined by the FE model. In this way this study will not ignore the issue of repeatability and give a more accurate prediction of failure rather than trying to pinpoint a single depth where failure occurs.

2.4 Summary of Chapter 2

Assessing the work cited in this chapter the following conclusions were reached.

- Research at the Argonne National Laboratory shows that magnesium alloys with their high strength to weight ratio and abundant supply have significant potential in the automotive and aerospace industries, and at the time of publication were already used to manufacture numerous auto parts.

- Heat transfer is a major factor in the formability of magnesium alloys. The work of Yoshihara and MacDonald [26] and El-Morsy and Manabe [27] found that by heating the die and blank holder and leaving the punch at room temperature localised thinning is reduced in the cup and formability is improved. This principle is implemented in the current work.

- Various fracture criteria including Cockcroft and Latham, Brozzo and Oyane were demonstrated by Takuda et al. [54] to be accurate at predicting fracture in sheet metal forming. Oyane's criterion was chosen for use in this current work as it is almost exclusively used by Japanese researchers who are investigating the formability of magnesium alloys for use in the auto industry.

- Takuda's work [53-54, 62,64] displays results graphically rather than numerically. There is no percentage of error between the experimental and FEA predicted fracture. There is also only one set of experimental results compared to the FEA results. No statistical analysis is ever given and no confidence in the FE model is ever given. This aspect will be examined in this current work.

Chapter 3: The Finite Element Method

3.1 Introduction

This chapter outlines the basic theory behind the finite element method used to model the sheet bulging process in later chapters. The essential steps used in every finite element model are examined, including; the material model, contact algorithm, element formulation and friction coefficient.

3.2 The Finite Element Method

The common steps involved in any finite element analysis are as follows:

1. Discretization

   In the discretization phase the problem domain is divided up into a finite number of regularly shaped elements. Each element consists of nodal points which have known coordinates within the global coordinate system of the problem. The shape of each element is defined in relation to its nodal point coordinates and interpolation or shape functions.

2. Element Formulation

   An interpolation function is assumed for the variation of the unknown across each element. This unknown can vary, but that is dependant on the nature of the analysis. In some analysis the unknown may be temperature, in others displacement and so on. Coefficient matrices are determined for each element which describe the responses of the element in question. In a stress analysis this matrix corresponds to the element stiffness matrix.

3. Transformation of Element Equations

   The element stiffness matrices are naturally aligned with their corresponding element local coordinate system. In order to solve the entire problem, these

matrices must be transformed so that they are aligned with the global coordinate system.

4. Assembly of Global Element Equations

   The transformed element matrices are now gathered together to form a global stiffness matrix that describes the behaviour of the entire problem domain.

5. Application of Boundary Conditions

   In order for the problem to be solved, some of the nodal unknowns must be constrained. Usually some if not all degrees of freedom of these particular nodes are restricted.

6. Solution Phase

   The nodal unknowns are determined by simultaneously solving the set of linear or non-linear algebraic matrix equations. The solution phase obtains values of the dependant variable at the location of each node.

7. Post Processing

   Further manipulation of nodal values and interpolation functions obtains secondary or derived quantities such as stresses and strains.

3.2.1 General Theory

This section elaborates further on the theory behind the finite element method and draws its references from [65] and [66].

There are a number of methods available for the determination of governing equations. One such method commonly employed to describe the equilibrium of a body, is the Principle of Virtual Displacements. This principle states, that the sum of the internal virtual work in the body and the external virtual work acting upon the body, due to external forces, is equal to zero. The internal virtual work is equal to the actual stresses going through the virtual strains. The external work is given by the

actual forces going through the virtual displacements. The virtual displacements must be kinematically admissible, that is, they are continuous functions of the spatial coordinates and satisfy kinematic boundary conditions on the portion of the surface for which such conditions are prescribed [59]. For a three-dimensional body with body forces f^B, surface traction f^S and concentrated forces F^i, resulting in virtual displacements U, virtual stress σ and virtual strain ε, the principle can be stated as:

$$\int_V \{\bar{\varepsilon}\}^T \{\sigma\} dV = \int_V \{\bar{U}\}^T \{f^B\} dV + \int_S \{\bar{U}\}^T \{f^S\} dS + \int_i \{\bar{U}\}^T F^i \qquad (3.1)$$

where:

$\{\bar{\varepsilon}\}^T = \left[\bar{\varepsilon}_{xx}\, \bar{\varepsilon}_{yy}\, \bar{\varepsilon}_{zz}\, \bar{\gamma}_{xx}\, \bar{\gamma}_{yy}\, \bar{\gamma}_{zz}\right]$

$\{\sigma\}^T = \left[\sigma_{xx}\sigma_{yy}\sigma_{zz}\sigma_{xy}\sigma_{yz}\sigma_{zx}\right]$

$\{\bar{U}\}^T = \left[\bar{U}\bar{V}\bar{W}\right]$ and $\bar{U}$, $\bar{V}$, and $\bar{W}$ are displacements in global directions.

$\{f^B\}^T = \left[f_x^B f_y^B f_z^B\right]$ where superscript B indicates body

$\{f^S\}^T = \left[f_x^S f_y^S f_z^S\right]$ where superscript S indicates surface

$\{F^i\}^T = \left[F_x^i F_y^i F_z^i\right]$ where superscript i indicates points

In the finite element analysis the body is approximated as an assembly of finite elements which interconnected at nodal points on the element boundaries. The displacements calculated within each element are assumed to be a function of the nodal point displacements. Thus, for element m:

$$u^{(m)}(x,y,z) = H^{(m)}(x,y,z)\hat{U} \qquad (3.2)$$

where $H^{(m)}$ is the displacement interpolation matrix or shape function for element m, and $\hat{U}$ is a vector for the three global displacement components U_i, V_i, and W_i at all nodal points (that is, if there are N nodes, then $\hat{U}$ will be of dimension 3N). Using the assumption on the displacements within each element, equilibrium equations corresponding to the nodal point's displacements of the elements within the assembly can be constructed from equations 3.1 and 3.2:

$$\sum_m \int_{V(m)} \varepsilon^{(m)T} \sigma^{(m)} dV^{(m)} = \sum_m \int_{V(m)} \overline{U}^{(m)T} f^{B(m)} dV^{(m)} + \sum_m \int_{S(m)} \overline{U}^{S(m)T} f^{S(m)} dS^{(m)} + \sum_M \overline{U}^{iT} F^i \qquad (3.3)$$

The corresponding element strains can be determined as:

$$\varepsilon^{(m)}(x,y,z) = B^{(m)}(x,y,z)\hat{U} \tag{3.4}$$

where $B^{(m)}$ is the strain-displacement matrix for element m. The rows of $B^{(m)}$ are obtained by appropriately differentiating and combining rows of matrix $H^{(m)}$.

The stresses within a finite element are related to the element strains and initial stresses by:

$$\sigma^{(m)} = D^{(m)}\varepsilon^{(m)} + \sigma^{I(m)} \tag{3.5}$$

where $D^{(m)}$ is a matrix which relates stress to strain in element m and $\sigma^{I(m)}$ is the element initial stresses. $D^{(m)}$ is a matrix that describes the material behavior and can be isotropic or anisotropic and can vary according to element type. Using equations 3.2, 3.4 and 3.5, equation 3.3 can be rewritten as:

$$\overline{U}^T\left[\sum_m \int_{V(m)} B^{(m)T} D^{(m)} B^{(m)} dV^{(m)}\right]\hat{U} = \hat{U}^T\left[\begin{array}{l}\left\{\sum_m \int_{V(m)} H^{(m)T} f^{B(m)} dV^{(m)}\right\} + \\ \left\{\sum_m \int_{S(m)} H^{S(m)T} f^{S(m)} dS^{(m)}\right\} - \\ \left\{\sum_m \int_{V(m)} B^{(m)T} \sigma^{I(m)} dV^{(m)}\right\} + F\end{array}\right] \tag{3.6}$$

where $H^{S(m)}$ is the surface displacement interpolation matrix for element m and is obtained from the volume displacement interpolation matrix, $H^{(m)}$, in equation 3.2 by substituting the element surface coordinates. F is a vector of the externally applied forces to the nodes of the finite element assemblage. It may be noted that, in equation 3.6 the nodal point displacement vector, $\hat{U}$ is outside the summation sign as it is independent of the element considered.

In order to obtain the equations for the unknown nodal point displacements from equation 3.6, the virtual displacement theorem is utilised by imposing unit virtual

displacements in turn, at all displacement components. This results in $\hat{U}^{T} = \mathbf{l}$ (where **l** is the identity matrix) and by denoting by $\hat{U} = \mathbf{U}$, the equilibrium equation of the element assemblage corresponding to the nodal point displacements is:

$$KU = R \tag{3.7}$$

The matrix K is the global stiffness matrix and is given by:

$$K = \sum_{m} \int_{V(m)} B^{(m)T} D^{(m)} B^{(m)} dV^{(m)} \tag{3.8}$$

The load vector $R = R_B + R_S - R_l + R_C$, where R_B is the effect of element body forces:

$$R_B = \sum_{m} \int_{V(m)} H^{(m)T} f^{B(m)} dV^{(m)} \tag{3.9}$$

R_S is the effect of element surface forces and is given by:

$$R_S = \sum_{m} \int_{S(m)} H^{S(m)T} f^{S(m)} dS^{(m)} \tag{3.10}$$

R_i is the effect of element initial stresses and is given by:

$$R_i = \sum_{m} \int_{V(m)} B^{(m)T} \sigma^{I(m)} dV^{(m)} \tag{3.11}$$

and $R_C = F$ (i.e. the concentrated loads).

Equation 3.7 is a statement of the static equilibrium of the finite element mesh. In equilibrium considerations, applied forces may vary with time, in which case the displacements may also vary with time. In such a case equation 3.7 is a statement of equilibrium for a specific point in time. If in reality the loads are applied rapidly, inertia forces must be considered and a dynamic problem must be solved. Using d'Alembert's Principle, the element inertia forces may be included as part of the body forces and in such a case equation 3.9 becomes:

$$R_B = \sum_m \int_{V(m)} H^{(m)T} \left[f^{B(m)} - \rho^{(m)} H^{(m)} \ddot{U} \right] dV^{(m)} \tag{3.12}$$

where $f^{B(m)}$ no longer includes inertial forces, $\ddot{U}$ gives nodal point accelerations and $\rho^{(m)}$ is the mass density of element m. In this case the equilibrium equations are:

$$M\ddot{U} + KU = R \tag{3.13}$$

where K is the global stiffness matrix, M is the global mass matrix and R and U are time dependant. The global mass matrix is given by:

$$M = \sum_m \int_{V(m)} \rho^{(m)} H^{(m)T} H^{(m)} dV^{(m)} \tag{3.14}$$

However, in a dynamic analysis, some energy is dissipated during vibration. In vibration analysis this is usually taken account of by introducing velocity-dependant damping forces. Introducing the damping forces as additional contributions to the body forces changes equation 3.12 as follows:

$$R_B = \sum_m \int_{V(m)} H^{(m)T} \left[f^{B(m)} - \rho^{(m)} H^{(m)} \ddot{U} - \kappa^{(m)} H^{(m)} \dot{U} \right] dV^{(m)} \tag{3.15}$$

where $\dot{U}$ is a vector of the nodal point velocities and $\kappa^{(m)}$ the damping property parameter of element m. In this case the equilibrium equations become:

$$M\ddot{U} + C\dot{U} + KU = R \tag{3.16}$$

where C is the global damping matrix and can be written as:

$$C = \sum_m \int_{V(m)} \kappa^{(m)} H^{(m)T} dV^{(m)} \tag{3.17}$$

3.2.2 Non-linearities

In the above formulation it was assumed that the displacements of the finite element assembly are small, that the material is linearly elastic and that the boundary conditions remain unchanged during the application of loads. These assumptions have entered the equilibrium equation in the following manner:

i. The fact that all integrations have been performed over the original volume of the finite elements implies that the displacements must be small.

ii. The strain displacement matrix, B, of each element was assumed to be constant and independent of element displacements.

iii. The assumption of a linear elastic material is implied in the use of a constant stress strain matrix D.

iv. The unchanged boundary conditions are implied by keeping constant constraint relations for the complete response.

The assumptions listed above point to the different types of non-linearity that may arise in a finite element analysis:

(1) Non-linearity due to large displacements, large rotations and large strains;
(2) Non-linearity due to large displacements, large rotations and small strains;
(3) Material non-linearity;
(4) Non-linearity due to contact.

3.2.3 Solution Methodology

The basic problem in a general non-linear analysis is to determine the state of equilibrium of the body due to the applied loads. Assuming that the external loads are described as a function of time, the equilibrium condition of the finite element assembly can be written as:

$$ {}^{t}R - {}^{t}F = 0 \tag{3.18} $$

where ${}^{t}R$ gives the externally applied nodal point forces at time t and the vector ${}^{t}F$ lists the nodal point forces corresponding to the element stresses, where:

$$ {}^{t}R = {}^{t}R_B + {}^{t}R_S + {}^{t}R_C \tag{3.19} $$

$$ {}^{T}F = \sum_{m} \int_{{}^{t}V(m)} {}^{t}B^{(m)T}\, {}^{t}\sigma^{(m)t}\, dV^{(m)} \tag{3.20} $$

It may be noted that in a dynamic analysis the vector ${}^{t}R$ would also include the inertial and damping forces. Equation 3.18 must express the equilibrium of the system in the current defined geometry by taking account of all non-linearities and must be satisfied throughout the complete history of load application. The solution process is carried out using a step by step incremental analysis. The basic approach in an incremental solution is to assume that the solution for the discrete time t is known and that the solution for a discrete time $t+\Delta t$ is required, where Δt is a suitably chosen time increment. Thus, at time $t+\Delta t$, equation (3.18) can be written as:

$$ {}^{t+\Delta t}R - {}^{t+\Delta t}F = 0 \tag{3.21} $$

As the solution at time t is known, it can be written that:

$$ {}^{t+\Delta t}F = {}^{t}F + F \tag{3.22} $$

where F is the increment in nodal point forces corresponding to the increment of element displacements and stresses from time t to time $t+\Delta t$. This vector can be approximated using a tangent stiffness matrix ${}^{t}K$ that corresponds to the geometric and material condition at time t.

$$ F \cong {}^{t}KU \tag{3.23} $$

where U is the vector of incremental nodal point displacements. Combining equations 3.21, 3.22 and 3.23 gives the following:

$$ {}^{t}KU = {}^{t+\Delta t}R - {}^{t}F \tag{3.24} $$

Upon solving this equation for U an approximation to the displacements at time t+Δt can be calculated:

$$^{t+\Delta t}U = {}^{t}U + U \tag{3.25}$$

Having evaluated an approximation to the displacements corresponding to time t+Δt an approximation for stresses and corresponding nodal point forces at time t+Δt can be obtained. However, because of the approximation expressed in equation (3.24), such a solution may be subject to significant errors and may be unstable. In practice it is frequently necessary to iterate until equation 3.21 is satisfied to sufficient accuracy.

Different solution procedures exist for the solution of equation 3.24. In this work the explicit time integration method was used and will be briefly outlined. The most common explicit time integration operator used in non-linear dynamic analysis is the central difference operator. The equilibrium of the finite element assembly is considered at time t in order to calculate the displacements at time t+Δt. Solution is sought for each time step for the equilibrium equation neglecting the effect of damping, which may be expressed as:

$$M\,{}^{t}\ddot{U} = {}^{t}R + {}^{t}F \tag{3.26}$$

where the nodal point force vector ^{t}F is evaluated on the basis of the methods used to formulate the material and geometric non-linearities. This involves the choice of element-type, the kinematic description and the kinetic description, all of which are problem-dependant. The solution for the nodal point displacements at time t+Δt is obtained using the central difference approximation for the accelerations as follows:

$$\ddot{U} = \frac{1}{\Delta t^2}\left\{ {}^{t-\Delta t}U - 2\,{}^{t}U + {}^{t+\Delta t}U \right\} \tag{3.27}$$

Combining this with equation (3.26) gives:

$$\frac{M}{\Delta t^2}\left\{ {}^{t-\Delta t}U \right\} = {}^{t}R - {}^{t}F - \frac{M}{\Delta t^2}\left\{ {}^{t-\Delta t}U - 2\,{}^{t}U \right\} \tag{3.28}$$

Thus, if $^{t-\Delta t}U$ and ^{t}U are known, $^{t+\Delta t}U$ can be determined from equation 3.28. A disadvantage in the use of this method is that, for stability, the time step size Δt must

be smaller than a critical time step size Δt_{CR}, which is equal to T_n/π, where T_n is the smallest period in the finite element assembly.

3.3 LS-DYNA 3D Theoretical Methods

3.3.1 Solution Methodology

LS-DYNA3D is an explicit dynamic finite element code for analysing highly non-linear transient dynamic problems. Metal-forming is a quasi-static process and can therefore be simulated using a dynamic analysis process, provided the kinetic energy of the process does not become too high, relative to the internal energy during the analysis.

The equilibrium equation of a dynamic problem and the solution process, using the central difference method was given above in equations 3.26, 3.27 and 3.28. As previously mentioned, calculation of the critical time step Δt_{CR} is of the utmost importance in a dynamic analysis, as the stability of the problem is dependent upon the use of a suitable time step. LS-DYNA calculates the time step using the equation:

$$\Delta t = 0.9\frac{l}{C} \tag{3.29}$$

where, l is the characteristic length of the smallest element, and C is the sonic wave propagation velocity through the element material. In order to ensure stability of the problem the value of time step is reduced using a scale factor of 0.9. The characteristic length, l, and the wave propagation velocity, c, are calculated differently depending on the element type used. In this work, a 4-node shell element was used where the characteristic length, l, is given by the equation:

$$l = \frac{A}{\max(l_1, l_2, l_3, l_4)} \tag{3.30}$$

and the sound wave propagation speed, C, is given by:

$$C = \sqrt{\frac{E}{\rho\left(1-\nu^2\right)}} \tag{3.31}$$

3.3.2 Element Formulation

The finite element model in this work consists of 4 node shell elements in each part. The Shell 163 element is used exclusively for explicit dynamic analyses and is mainly used to model thin structures such as sheet metals. Shell 163 has both bending and membrane capabilities and both in-plane and normal loads are permitted. There are 12 degrees of freedom associated with this element; translations, velocities and accelerations along the nodal x, y and z directions, and rotations about the nodal x, y and z axes. The shells must be assigned real constants, in this case thickness and a number of integration points, or points of calculation through the thickness. The minimum number of integration points available is two while the maximum is five. Increasing the number of integration points results in a more accurate analysis and reduces the risk of hour glassing modes, but consumes more time and processing memory.

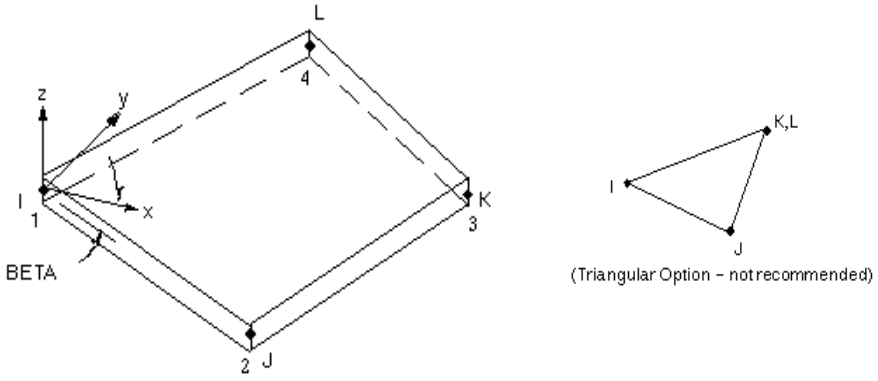

Figure 3-8: Shell 163 Element Configuration [67]

There are twelve formulations to choose from when using Shell 163 elements. The default formulation is the Belytschko-Tsay formulation which consists of two integration points through the thickness of the shells and this was used to model the tooling of the sheet bulging rig which were modelled as rigid bodies. The

Belytschko-Wong formulation calculates any warping effects in the elements and this was used to formulate the blank as it could model the evolution of wrinkles should they occur.

3.3.3 Material Model

ANSYS LS-DYNA has an extensive library of material models to the behaviour of many different materials under numerous conditions. As previously stated the tooling of the sheet bulging rig was modeled as rigid bodies, which consisted of a simple bilinear isotropic material formulation, which included density, Young's modulus and Poisson's ratio. Constraints were also applied to the rigid bodies during formulation to restrict their motion during the analysis. Typically parts modelled as rigid bodies are not the areas of interest in the solution, and so the rigid body model helps to reduce computation time during solving by minimising the number of calculations performed on parts using this formulation.

The AZ31 blank was modeled as a transversely anisotropic hardening model, which is available for shell and 2D elements. It cannot however be applied to a 2D axisymmetric analysis which meant that a 3D model was required to simulate the sheet forming of the anisotropic blank. In this model the yield function was based on Hill's criterion [68].

$$F(\sigma_y - \sigma_z)^2 + G(\sigma_z - \sigma_x)^2 + H(\sigma_x - \sigma_y)^2 + 2L\tau^2_{yz} + 2M\tau^2_{xx} + 2N\tau^2_{xy}$$
$$= 2/3\ (F + G + H)\ \overline{\sigma}^{\,2} \qquad (3.32)$$

Where F, G, H, L, M and N are the anisotropic parameters. Equation 3.32 was derived from Hill's initial quadratic equation where the same yield stress values are predicted for tension and compression. In Hill's initial criterion, the quadratic was equal to one, but in ANSYS the material anisotropy is assumed to be orthogonal and so Hill's initial quadratic can be rewritten in the form shown in equation 3.32.

In the finite element material model the yield function provided by Hill's criterion was reduced to give the following for the case of plane stress:

$$F(\sigma) = \sigma_y = \sqrt{\sigma_{11}^2 + \sigma_{22}^2 - \frac{2R}{R+1}\sigma_{11}\sigma_{22} + 2\frac{2R+1}{R+1}\sigma_{12}^2} \tag{3.33}$$

Where R is the anisotropic hardening parameter which is the ratio of the in-plane to out of plane plastic strain rate.

3.3.4 Contact Algorithm

Unlike implicit analyses where contact is defined using contact elements, explicit analyses define contact using contact surfaces between parts. ANSYS LS-DYNA includes twenty four different contact types to define the interaction between surfaces in an explicit analysis. Although this wide choice of contact options can be beneficial it is crucially important that the various contact options are understood in order to accurately describe the physical interaction of the parts. There are three basic contact algorithms available: single surface contact, nodes to surface contact and surface to surface contact. The surface to surface contact algorithm was used to define interaction between each of the parts in this study.

The surface to surface contact algorithm is the optimum choice for sheet metal forming processes such as sheet bulging. This algorithm is most commonly used to define contact for bodies that have large contact areas and is very efficient for bodies that experience large amounts of relative sliding with friction. Contact is detected when the surface of one body penetrates the surface of another. When using automatic surface to surface contact (ASTS), the contact surface orientation for shell elements is automatically determined by the automatic contact algorithms. Both sides of the shell elements are checked to determine if contact takes place rendering the need to specifically assign target and contact surfaces subjective.

The ASTS algorithm is based on the penalty method. A stiffness or resistance between the two contacting bodies must be established or the bodies will pass through one another. This stiffness relationship is established by placing “elastic springs” between the two bodies, where the master surface stiffness, k, is calculated as follows:

$$k = \frac{(SFSI)KA^2}{V} \tag{3.34}$$

Where A is the surface area, V is the volume of the element, K is the bulk modulus of the element and SFSI is the scale factor that is used to control the stiffness and generally has a default value of 0.1.

3.3.5 Friction

As two come in contact with each other their surfaces tend to either stick or slide across one another. LS-DYNA employs a Coulomb friction law to calculate any slipping or sticking effects and also to determine the transition from sticking to sliding and vice versa. There are two coefficients of friction that must be defined for the contact model; static friction and dynamic friction. Normally static friction is greater than dynamic friction and LS-DYNA uses an exponential function to smooth the transition between these two values. The relationship between the coefficient of friction and the relative surface velocity is defined by the equation:

$$\mu = \mu_d + (\mu_s - \mu_d)\, e^{-cv} \tag{3.35}$$

Where μ_s and μ_d are the static and dynamic coefficients of friction respectively, c is the decay constant and $v = \Delta e / \Delta t$ where Δt is the time step. Relating the coefficient of friction to the forces involved, if f* is the trial force, f_n is the normal force, k is the interface stiffness, μ is the coefficient of friction and f^n is the frictional force at time n, then;

$$f^* = f^n - \mu\, k\, \Delta e \tag{3.36}$$

where:

$$\Delta e = r^{n+1}(\zeta_c^{n+1},\ \eta_c^{n+1}) - r^{n+1}(\zeta_c^{n+1},\ \eta_c^{n+1}) \tag{3.37}$$

In which (ζ_c, η_c) are the contact coordinates and r represents the master segment that has a unique normal, the orientation of which depends on the points of the corresponding master segment. The shear stress that develops at the interface of the surfaces as a result of Coulomb friction can be large and in some cases exceed the

ability of the material to withstand the level of stress. To prevent this from happening the following limit is placed on the tangential force:

$$f^{n+1} = \min\left(f_{coulomb}^{n+1},\ \kappa A_{master}\right) \tag{3.38}$$

where A_{master} is the area of the master segment and κ is the viscous coefficient.

3.3.6 Mass Scaling

Mass scaling is a technique used to shorten the solution phase of a transient analysis by adding a small amount of mass to certain elements thus increasing the minimum time step. The minimum time step size for explicit time integration is dependant on the minimum element length l_{min} and the sonic speed, c through the material. Mass scaling adjusts the element density to achieve a desired time step size for element i according to the equation:

$$\rho_i = \frac{(\Delta t_{specified})^2 E}{l_i^2 (1 - v^2)} \tag{3.39}$$

The mass scaling value can be applied to the model in one of two ways: if the mass scaling input value is positive then the same step size is used for all elements, if the value is negative, mass scaling is only applied to elements whose time step size is smaller than the specified value. The second method is more efficient and was applied in this work. As previously stated the use of mass scaling increases the mass of elements introduces a very small amount of error into the model.

3.4 Summary of Chapter 3

This chapter details the theoretical equations behind the finite element method and also outlines the theory behind certain modeling features in ANSYS LS-DYNA such as contact, friction and mass scaling and how they are implemented into the finite element model.

Chapter 4: Mechanical Testing

4.1 Introduction

This chapter examines the mechanical or physical testing of the magnesium alloy AZ31. There were three types of tests performed on the material; tensile tests, biaxial tests and sheet bulging. The tensile test provided the material properties of the magnesium alloy for use in the finite element model. The biaxial test determined the fracture strains and material constants required for the ductile fracture criterion, while the sheet bulging tests involved the actual forming of AZ31 sheets. The results of both the tensile and biaxial tests are presented in this chapter while the results of the sheet bulging process are presented together with the finite element results in Chapter 7.

4.2 The Tensile Test

The tensile test is one of the most important and widely used material tests as it provides basic mechanical properties on the strength of materials. The results from these tests demonstrate the elastic and plastic behaviour of materials over complex loading histories. Normally this form of testing is carried out at room temperature with a strain rate in the order of 10^{-2} to 10^{-4} / sec. Figure 4-1 shows the geometry of the tensile test specimen used in the mechanical testing of this current work. The thickness of the specimen was 0.56mm. The thin bar section is known as the gauge, and this is the region where measurements of stress and deformation are made. The tensile test is a form of destructive testing where during the test a specimen is subjected to an increasing uniaxial load until fracture occurs. The rate of increase of the load is dependant on the strain rate. From this failure data many observations can be made with regards to the materials strength and ductility. This data is usually presented in the form of a stress strain curve.

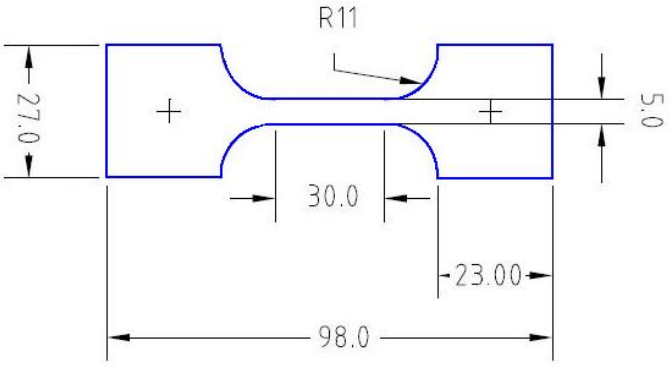

Figure 4-1: Tensile test specimen (Dimensions in millimeters)

The results of the tensile test are presented graphically using a stress strain curve where the tensile stress is plotted against the strain of the specimen. Important material properties such as Young's modulus, yield stress, ultimate tensile stress and failure strain can be obtained from this curve.

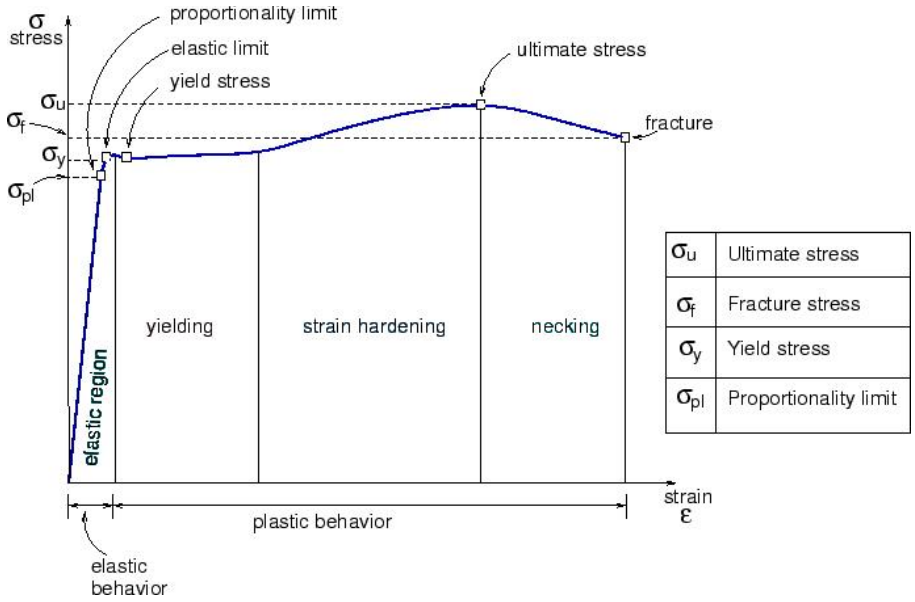

Figure 4-2: Engineering Stress - Strain Curve [69]

Figure 4-2 shows an example of such a curve and highlights the regions of interest. The elastic region is where the material undergoes non-permanent deformation and will return to its normal shape after the load is removed. Once the elastic limit is reached the material undergoes permanent or plastic deformation. The strain

hardening zone involves continued plastic deformation with increasing plastic strain until the onset of necking, or thinning of the specimen gauge. This thinning continues until fracture finally occurs.

There are two types of stress strain curves; engineering stress - strain curves and true stress strain curves. Engineering stress is calculated using the original cross sectional area of the specimen throughout the tensile test. The true stress during plastic deformation is calculated using the deformed cross sectional area which is continuously measured during the test, and is therefore more accurate than the engineering stress curve. It is possible to convert from engineering stress to true stress using the equation:

$$\sigma = s\,(e + 1) \tag{4.1}$$

where s is the engineering stress and e is the engineering strain.

A similar equation exists to convert to true plastic strain:

$$\varepsilon = \ln\,(e + 1) \tag{4.2}$$

Both of these equations are valid until the onset of necking.

4.3 Tensile Test Results

Ten tensile tests were performed at both 100˚ and 150˚ C using specimens with the dimensions shown in Figure 4-1. Tables 4.1 and 4.2 show the results from both sets of tests respectively. The stress / strain results in these tables are the true stress / strain results calculated from the engineering stress and strain using equations 4.1 and 4.2. As expected the Young's modulus, yield stress and tensile strength decrease with increasing temperature, while the material is more ductile at 150˚ C and on average has a higher elongation at fracture. The average values from these tables were used in the finite element model to define the material properties of the alloy at both temperatures.

Table 4.1: Tensile Test Results at 100˚ C

Specimen No	Young's Modulus (GPa)	Yield Stress (MPa)	Tangent Modulus (MPa)	Elongation %	UTS (MPa)
1	29.4	57	2261.26	11.3	308
2	48.3	99	2703.13	6.6	272
3	69.2	134	3113.64	4.6	271
4	16.9	36.5	1906.72	13.6	292
5	23.6	50	1761.19	13.6	286
6	26.43	46	1852.27	9	209
7	37.42	67	1581.63	10	222
8	25.82	50	1503.82	13.3	247
9	29.98	61.5	984.76	16.6	223
10	35.99	63.8	1184.73	13.3	219
Average	34.3	66.48	1885.31	11.19	254.9
Std Dev	14.98	29.06	656.21	3.66	35.39

Table 4.2: Tensile Test Results at 150˚ C

Specimen No	Young's Modulus (GPa)	Yield Stress (MPa)	Tangent Modulus (MPa)	Elongation %	UTS (MPa)
1	24.6	49	690.22	18.6	176
2	30.99	62	1091.6	13.3	205
3	43.97	83	1179.49	8	175
4	26.72	48.5	787.16	15	165
5	25.55	48	742.69	17.3	175
6	27	48.5	722.22	17.3	172
7	26.5	48.5	733.92	17.3	174
8	25.5	48.5	1040.54	11.3	164
9	27.2	48	737.8	16.6	169
10	24.6	46	848.48	20	214
Average	28.26	53	857.41	15.47	178.9
Std Dev	5.81	11.44	178.29	3.65	16.79

There was a large deviation in the material properties, particularly in Table 4.1. This deviation was caused by one or two samples producing inaccurate results at both temperatures. It is probable that these inaccuracies were the result of human error during testing. Specimens number two and three for instance, produced results that deviated significantly from the other values at both temperatures. Apart from these two specimens the other values were fairly consistent. The tangent modulus values consisted of the largest deviation, mainly because they were calculated from other

values which were in turn subjected to variance. The tangent modulus values were calculated using equation 4.3

$$\text{Tan Mod} = (\sigma_{uts} - \sigma_y) / (\varepsilon_f - 0.002) \quad (4.3)$$

Where ε_f is the fracture strain. The tangent modulus can also be calculated using the strain corresponding to the ultimate tensile stress, but in this study the strain at fracture was used. Although the large spread of the results influenced the average values which were used to define the finite element material model, the probabilistic analysis examined the response of the model over the entire range of material property values.

Figures 4-3 and 4-4 show the true stress strain curves from specimens tested at 100˚ and 150˚ C respectively. Both graphs are taken from specimens whose results are very close to the overall average for their respective temperature. These plots help to illustrate the earlier observations made when reviewing the tables of results; namely the lower yield point, lower tensile strength and improved ductility of the magnesium alloy at higher temperatures.

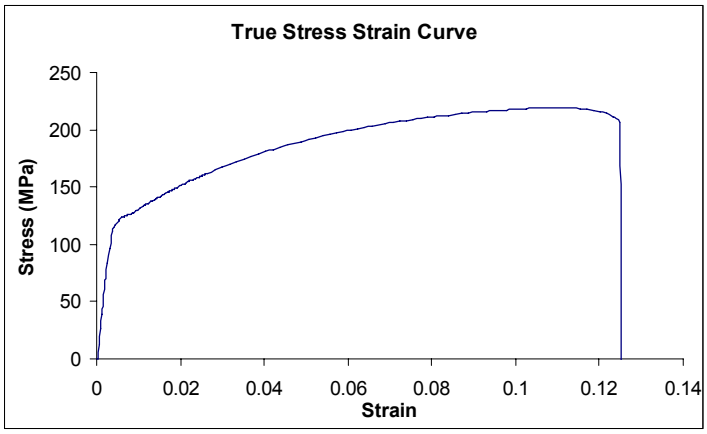

Figure 4-3: Stress Strain Curve for Specimen No. 10 at 100˚ C

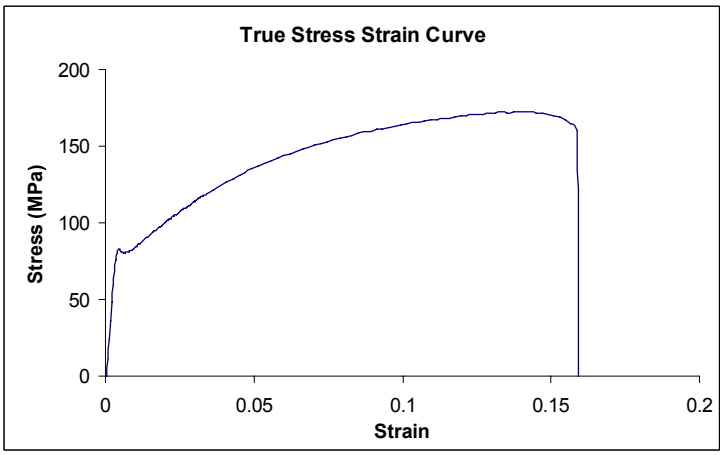

Figure 4-4: Stress Strain Curve for Specimen No. 6 at 150˚ C

4.4 Calculation of Material Constants for Ductile Fracture Criterion

Uniaxial and plane strain tests of magnesium alloy AZ31 were conducted in collaboration with the team of Dr. Yoshihara at Tokyo Metropolitan University in order to determine the material constants required for Oyane's ductile fracture criterion as shown in Equation 4.4.

$$\int_0^{\bar{\varepsilon}_f} \left(\frac{\sigma_m}{\bar{\sigma}} + a\right) d\bar{\varepsilon} = b \tag{4.4}$$

The various terms in Equation 4.4 can be written in terms of the material's anisotropy, r, for both uniaxial and plane strain as follows:

Uniaxial Strain:

$$\frac{\sigma_m}{\bar{\sigma}} = \frac{1}{3}\sqrt{\frac{2(2+r)}{3(1+r)}} \tag{4.5}$$

$$d\bar{\varepsilon} = \sqrt{\frac{2(2+r)}{3(1+r)}}\, d\varepsilon_1 \tag{4.6}$$

Plane Strain:

$$\frac{\sigma_m}{\bar{\sigma}} = \frac{1}{3}\sqrt{\frac{2(2+r)(1+2r)}{3(1+r)}} \tag{4.7}$$

$$d\bar{\varepsilon} = \sqrt{\frac{2(2+r)(1+r)}{3(1+r)}}d\varepsilon_1 \tag{4.8}$$

Substituting these terms into Oyane's equation results in a pair of simultaneous equations that describe the fracture criterion in terms of uniaxial and plane strain. These are shown in Equations 4.7 and 4.8 respectively. Solving this set of equations determines the values of the a and b material parameters required for Oyane's criterion.

$$(\frac{1}{3}\sqrt{\frac{2(2+r)}{3(1+r)}} + a)\sqrt{\frac{2(2+r)}{3(1+r)}}\varepsilon_f = b \tag{4.9}$$

$$(\frac{1}{3}\sqrt{\frac{2(2+r)(1+2r)}{3(1+r)}} + a)\sqrt{\frac{2(2+r)(1+r)}{3(1+r)}}\varepsilon_f = b \tag{4.10}$$

The fracture strain ε_f is calculated from measurements of the materials thickness and width at failure. This relationship is given as:

$$\varepsilon_f = -(\varepsilon_b + \varepsilon_t) \tag{4.11}$$

Where ε_b is the strain across the width of the sample and is given as the logarithmic ratio of the final width to the original width:

$$\varepsilon_b = \ln(\frac{W_1}{W_0}) \tag{4.12}$$

Similarly ε_t is the strain through the thickness and is given as:

$$\varepsilon_t = \ln(\frac{t_1}{t_0}) \tag{4.13}$$

4.4.1 Uniaxial Testing

The uniaxial testing conducted in collaboration with Dr. Yoshihara's team [70] measured the material strain at two points across the width of the sample and at three points through the thickness as shown in Figure 4-5. The strain at each measurement across the width of the sample was calculated using Equation 4.12, while the strain through the thickness at each point was calculated using equation 4.13. The average of the two strains measured across the width together with the average of the three strains measured through the thickness were used in Equation 4.11 to calculate the fracture strain of the specimen.

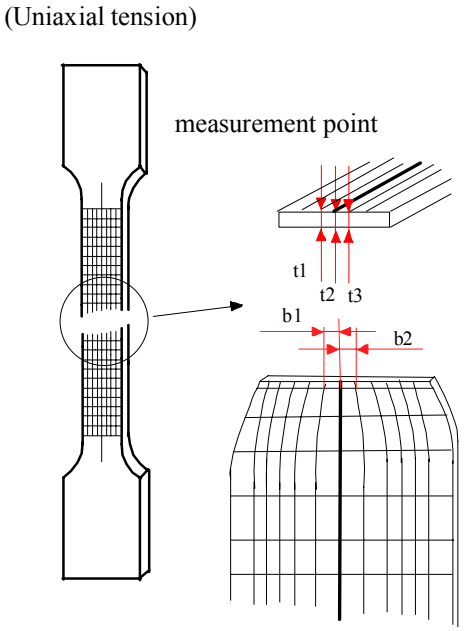

Figure 4-5: Points of Strain Measurement in Uniaxial Testing

4.4.2 Plane Strain Testing

A plane strain test is a variation on the uniaxial tensile test where strains in biaxial directions are determined. Like the tensile test the test specimen is held in place at one end while an axial load is applied to the opposite end. The plane strain test can be performed in a universal Instron testing machine similarly to the uniaxial tensile test, although the clamps used to fix the specimens to the base and the crosshead are a different type. The specimen in a plane strain test, as shown in Figure 4-6, is different from the usual tensile specimen as it has a notch in the centre of the gauge section where failure will occur. As the specimen is pulled apart high stress concentrations build up around the plastic region resulting in large stresses in the z direction. These large stresses result in strain only in the x-y plane, and this is known as plane strain.

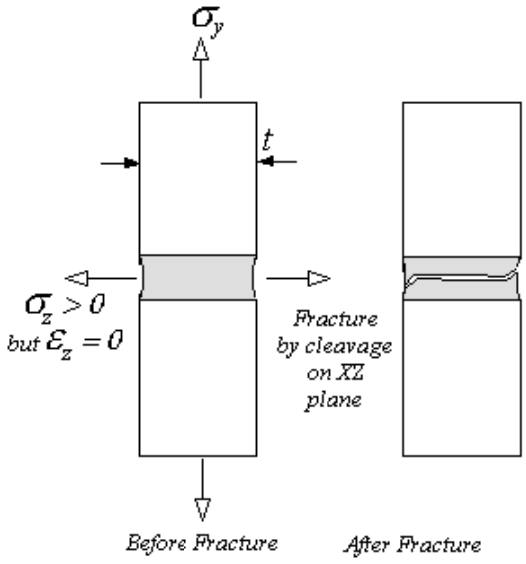

Figure 4-6: Plane Strain Test Specimen

Plane strain testing was conducted to determine the plane strain values used to determine the Oyane constants. The plane strain testing carried out at the Tokyo Metropolitan University measured the material strain at fourteen points through the thickness of the specimen and twice across the width as shown in Figure 4-6. Again the strain at each measurement across the width of the sample was calculated using Equation 4.12, while the strain through the thickness at was calculated using

Equation 4.13. In plane strain testing the specimen fails through its thickness and this value greatly influences the overall fracture strain, hence it was more beneficial to increase the number of measurements through the thickness rather than concentrating on the width. The average of the two strains measured across the width together with the average of the fourteen strains measured through the thickness were used in Equation 4.11 to calculate the fracture strain of the specimen.

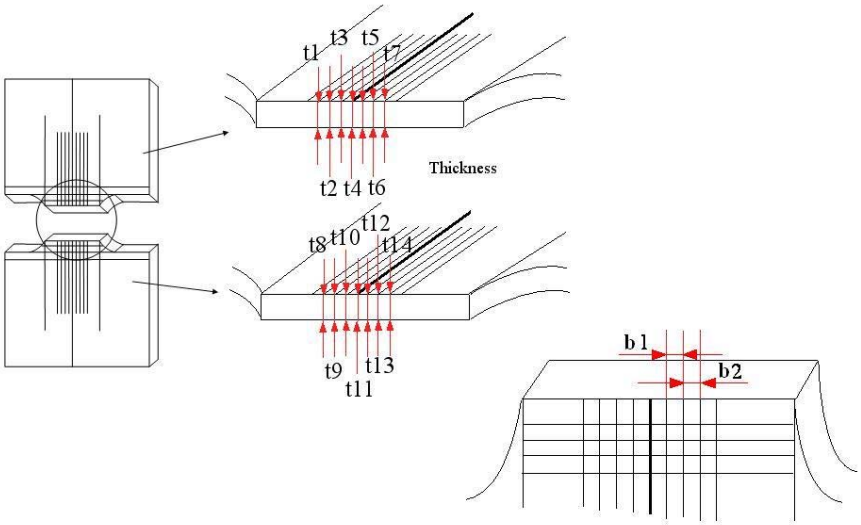

Figure 4-7: Measurement Points in Plane Strain Testing

4.4.3 Material Parameter Test Results

The plane strain tests to determine the Oyane's fracture constants were conducted by Dr. Yoshihara's team. Two samples at each temperature were tested and the test results are shown in Tables 4.3 and 4.4. The average uniaxial and plane strain fracture strains together with the normal anisotropy were substituted into equations 4.9 and 4.10 and the set of simultaneous equations were solved to determine the material parameters a and b.

Table 4.3: Oyane Constants at 100°C from Plane Strain Testing [70]

100° C	ε_f Uniaxial	ε_f Plane Strain	Anisotropy	a	b
Set 1	0.643	0.082	2.14	-0.226	0.0516
Set 2	0.568	0.113	2.21	-0.155	0.0831
Difference	0.075	0.066	0.07	0.071	0.0315

Table 4.4: Oyane Constants at 150°C from Plane Strain Testing [70]

150° C	ε_f Uniaxial	ε_f Plane Strain	Anisotropy	a	b
Set 1	0.8	0.09	1.97	-0.24	0.051
Set 2	0.75	0.13	2.08	-0.19	0.086
Difference	0.05	0.04	0.11	0.05	0.035

There were slight differences between the results from both sets of tests. The Oyane Constants were sensitive to variance as any deviation between the strain and anisotropy values were amplified when they were substituted into the equations used to calculate the constants. Although both sets of strain values at each temperature were reasonably close, the second set of data was used in the finite element model, as in this set of tests there were fourteen strain measurements made for each sample, compared to just three measurements per sample in data set 1. It was determined that the best way to verify the data was to use them to predict fracture in a finite element model and compare the results to a set of experimental data. Therefore the second set of Oyane Constants were used in some early finite element models which very accurately predicted fracture when compared to some experimental sheet bulging data provided by Dr. Yoshihara [70]. These values for the Oyane constants were then deemed to be valid and were used in the present study.

4.5 Experimental Sheet Bulging Apparatus

Magnesium AZ31 blanks, 76mm in diameter were bulged at both 100° and 150° Celsius, using a rig built previously for cold-work processing [71], that was modified to conduct sheet bulging experiments at high temperatures. Changes made to the original design included a hemispherical punch to produce the desired bulge profile of the formed blank and a heater band that heated the die and the blank holder to the desired forming temperature which was maintained at a constant level during forming using a thermocouple. Figure 4-7 shows the components of the sheet bulging rig, while Figure 4-8 illustrates its schematics.

Figure 4-8: Sheet Bulging Apparatus

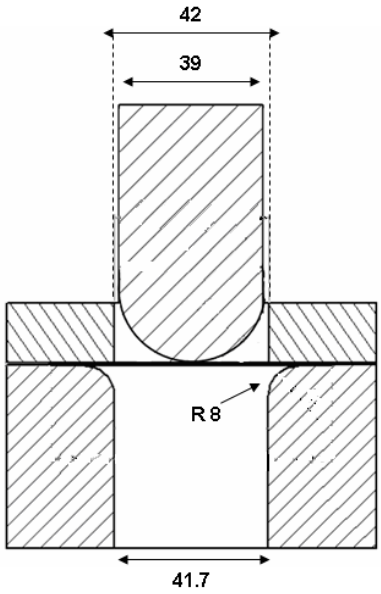

Figure 4-9: Schematic Cross Section of Sheet Bulging Apparatus

The blank holder force was controlled using four springs that when in compression exerted a force on the blank holder which in turn exerted force on the blank. The blank holder apparatus is shown in more detail in Figure 4-9. The level of compression of each spring was controlled using a threaded bolt that pressed directly into a steel cap fitted at the end of each spring (Figure 4-10). As the bolts were

tightened the steel caps were pushed downwards and forced the springs to compress, thus exerting a force on the blank holder.

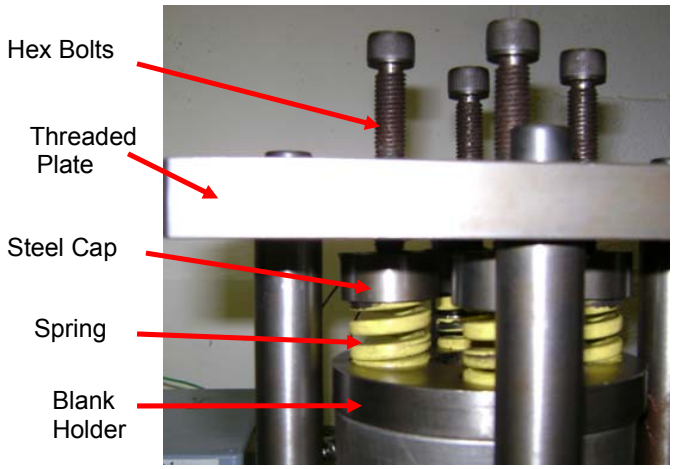

Figure 4-10: Blank Holder Mechanism

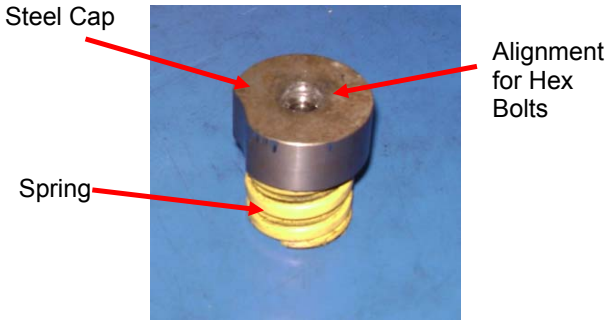

Figure 4-11: Compression Spring & Cap

A relationship was established between the level of compression of the springs and the resultant force exerted on the blank holder. Table 4.4 shows the displacement of the threaded bolts and the corresponding resultant force of the four springs. The maximum compression of the springs was 12mm which corresponded to a maximum blank holder force of 20.4 kN.

Table 4.4: Blank Holder Force / Pressure (BHF / BHP) per mm of Compression

Deflection (mm)	2	3	4	5	6	8	10	12
BHF (kN)	3.4	5.1	6.8	8.5	10.2	13.6	17	20.4
BHP (MPa)	0.914	1.371	1.828	2.285	2.742	3.656	4.57	5.484

The testing itself was conducted using the Instron 4200 series laboratory testing machine which consisted of an adjustable crosshead arm whose motion was restricted to vertical displacement. The hemispherical punch was attached to the crosshead and its displacement and force exerted on the blank were recorded during testing. The punch speed was kept constant throughout testing at a rate of 50 mm/min. This forming speed was chosen as previous bulged samples of magnesium alloy provided by Dr. Yoshihara [70] were formed using a similar punch velocity and results compared favourably to early finite element simulations of the process. Initial sheet bulging experiments conducted at higher punch velocities resulted in samples forming without fracture. It was necessary to obtain a suitable punch velocity for the experiments where fracture may occur in order to compare the results with those from the finite element simulation.

The aim of the physical testing was to examine the conditions in which fracture would occur. If all the samples were to form without fracture then there would be no results to verify the finite element fracture model. Therefore several preliminary samples were formed in order to determine the conditions under which fracture would occur. The conditions examined included the blank holder force, the punch velocity and the amount of lubricant used. It was determined that at both temperatures the maximum blank holder force of 20.4kN was required to induce fracture of the blank without wrinkling. A copper based lubricant, Rocol, was applied to the blank, punch and die. It was important to accurately judge the appropriate level of lubricant applied as too little would result in early fracture, while too much would result in the lubricant's oil base burning and damaging the sample.

4.6 Summary of Chapter 4

This chapter outlined the various testing involved in obtaining the material properties for the magnesium AZ31. The tensile tests together with the uniaxial and plane strain tests conducted to determine the material constants for the ductile fracture criterion were outlined and the results listed. Finally the experimental apparatus and procedure used to bulge the AZ31 sheets was examined in detail

Chapter 5: The Finite Element Model

5.1 Introduction

This chapter examines the methods involved in creating the finite element model to simulate the sheet bulging process of magnesium alloy AZ31 at 100˚C and 150˚C. In this study the model was created and solved using the explicit finite element software ANSYS LS-DYNA. All aspects of the model including material models, element formulation, meshing, damping, boundary conditions and loading are examined. There were various options available for many of these features, and these are discussed together with the reasons behind implementing some of them into the model.

5.2 Parametric Modeling

Every command used to build the model was stored in an input file. The code in the input file was adjusted so that the model was defined in terms of parameters. All aspects of the model such as the geometry, material properties, mesh size, contact and loading conditions were defined as parameters which were created at the beginning of the input file.

Often when making adjustments to a model in ANSYS, it is necessary to delete numerous features before an adjustment can be made. For example for a fully meshed model, to make any changes to the geometry the mesh must be cleared together with any loads or boundary conditions on its nodes. Then once the change has been made, all these features must be reapplied. This can be considerably frustrating and time consuming. Parametric modeling makes it very simple to adjust any feature without having to backtrack or even create a new model from scratch. Changes can be made to the parametric values and the input file can be read into the ANSYS processor over and over again recreating the model in seconds.

In this current work the sheet bulging process was simulated at 100˚C and 150˚C. This involves creating two different models, but many features were common to both models such as the geometry, mesh and boundary conditions. Without parametric modeling these models would have had to be made separately from scratch, but with changes to some of the features of the 100˚C model, a new model was quickly created for 150˚C.

Parametric modeling was also essential in the implementation of the ductile fracture criterion into the model. The fracture criterion was implemented into the ANSYS LS-DYNA post processor using the ANSYS Parametric Design Language (APDL) which is discussed in more detail in Chapter 6. Without the original FE models being written in parametric form it would have been very difficult to calculate the location of fracture in the blank. The macro used to predict failure in the model was generic and with slight adjustments could be used to detect fracture in other sheet metal forming simulations. Without a parametric model to build and solve the problem the macro would have had to use very specific parameters which could have been stored in the original parametric model.

5.3 Geometry

The sheet bulging process at 100˚C and 150˚C was simulated using the explicit finite element software, ANSYS LS-DYNA 9.0. Using measurements taken from CAD drawings of the rig and taking advantage of symmetry, it was possible to model a quarter of the experimental apparatus. Initially the profile of each part was defined in 2D using lines created on the x-y plane. These lines were then revolved about the y axis to form a 3D model of the apparatus, as shown in Figure 5-1.

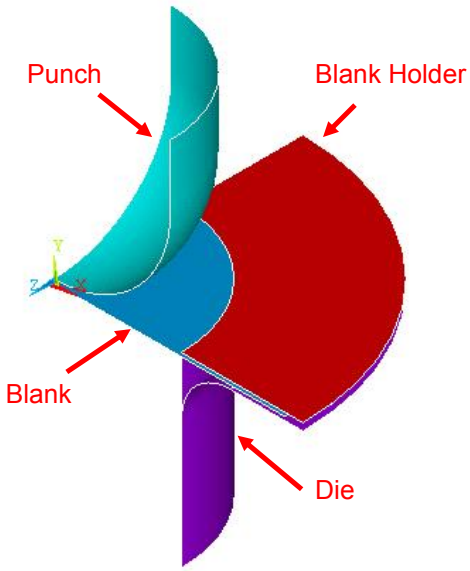

Figure 5-1: Geometry of the finite element model

In sheet bulging, as is the case with many other metal forming operations, the tooling is a lot more rigid than the part that is to be formed. Generally any stresses or strains on the tooling during the process are irrelevant as the tooling is designed to easily withstand the high forces associated with the particular forming process. Using this assumption the parts comprising the tooling were modelled as rigid bodies. In LS-DYNA parts that are modelled as rigid bodies have a reduced amount of nodal and elemental data calculated for them during the solution phase, thus reducing the computational time needed to solve the model. In these models, the reaction of the blank during forming was the focus of the analysis, so greater attention was focused on modeling that part in more detail.

5.4 Element Formulation

Each part in the model was discretised using four node shell elements (shell 163). No thermal elements were used in the model, instead the material properties were adjusted to represent behaviour at different temperatures. Shell elements are widely used to simulate sheet metal forming processes as they have a greater flexibility than solid elements and can more accurately simulate bending during forming. The shells have a thickness associated with them and also consist of a number of layers or integration points through the thickness. The number of integration points is variable,

but generally increasing the number of integration points improves the accuracy of the results, yet simultaneously increases the computational time required to solve the model. The element thicknesses and integration points used in this study is shown in Figure 5-2.

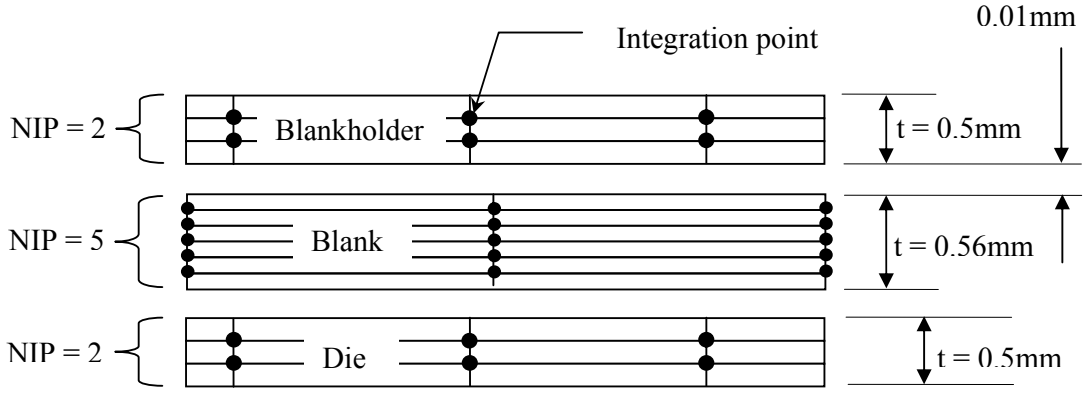

Figure 5-2: Shell element thickness and integration points

The tooling was modelled using a shell thickness of 0.5mm and two integration points, while the blank was modelled using a shell thickness of 0.56mm, (the thickness of the AZ31 sheets) and five integration points. It was found that the accuracy did not improve with any more than five integration points. A gap of 0.01mm between the surfaces was recommended [72] to reduce initial forces between the parts. The stress and strain results used in the fracture criterion to predict fracture in the blank were taken from the middle layer of the shell element. Although higher stresses and strains can occur on the surface layers of the element due to stretching of the blank during forming, fracture may not actually occur, and a false detection of fracture may be given due to the high strain values. Oyane's criterion is based on the strain history of the material, and large strains caused by material stretching at the surface layer can result in a premature detection of fracture. By using the values from the middle layer of the shell element, the effect of large surface strains can be avoided. It is also important to note that should true fracture occur then the crack must propagate through the whole thickness of the blank and so would be detected in the middle layer.

Shell 163 elements have twelve different element formulations associated with them. In this model two different formulations were used. The tooling was modelled using

the default Belytschko-Tsay formulation. This formulation provides the quickest solution time than any of the other explicit shell formulations. The blank was modelled using the Belytschko-Wong formulation which is similar to Belytschko-Tsay but calculates warping effects in the elements. This formulation was the optimum choice for the blank as it could simulate any warping or wrinkling of the blank, which is a quite common defect in sheet metal forming.

5.5 Material Models

As previously stated the tooling of the sheet bulging rig were modelled as rigid bodies which consisted of a simple bilinear isotropic elastic material formulation, which included density, Young's Modulus and Poisson's ratio. These values came from previous work on the same test rig by Galvin [71] Table 5.1 lists the material properties used for the punch, die and blank holder.

Table 5.5: Material Data used for the Punch, Die and Blankholder

Mild Steel	
Density (Kg/m^3)	8190
Poisson's Ratio	0.3
Young's Modulus (GPa)	210

These values were used at both 100˚C and 150˚C because the parts were modelled as rigid bodies and the results from these parts were irrelevant, the only concern being that the parts had an adequate stiffness to withstand the forces during forming. The punch however was at room temperature during forming and so these figures accurately described its material properties.

The magnesium alloy blank was modelled as a transversely anisotropic hardening model whose yield function was based on Hill's criterion [68]. This material model was chosen because Oyane's ductile fracture criterion was also derived using Hill's yield criterion, and the anisotropic parameter required for this material model is also used in the equations to calculate the material constants in Oyane's equation (see equations 4.4 – 4.9 in Chapter 4). Early models built to validate the work of Takuda

[62] also found that greater accuracy was achieved with an anisotropic material model than with a more general power law model.

Table 5.6: Material Data Used for the AZ31 Blank

Magnesium AZ31	100˚C	150˚C
Density (Kg/m^3)	1660	1660
Poisson's Ratio	0.27	0.27
Young's Modulus (GPa)	34.3	28
Yield Stress (MPa)	66	53
Tangent Modulus (MPa)	1885	857
Anisotropy	2.21	2.08

Table 5.2 lists the material properties used in the material model for AZ31 at both 100˚C and 150˚C. These properties were the average values obtained from tensile tests performed at both temperatures; the full list of the results from testing is displayed in Chapter 4. The values for density, anisotropy and Poisson's ratio were obtained from tests conducted by Dr Yoshihara's team [70]. These values were validated against the work of Takuda [62].

5.6 Meshing

Figure 5-3 shows the discretised finite element model of the entire problem. Each part was meshed using a global element edge length of 1.2mm. The mapped mesh option was used in the meshing of each part as it resulted in a more manageable mesh which would allow contact to be detected more easily between the bodies. Tests of mesh convergence showed that the accuracy of the results did not show any significant improvement with a finer mesh than 1.2mm, hence the mesh was deemed to have converged at this point.

The meshed model consisted of 5,331 elements in total. The number of elements for the punch, die, blank holder and blank were 867, 1671, 918 and 1875 elements respectively. The highest number of the mesh elements occurred in the blank as this was the area of interest in the analysis. A more detailed view of the mesh in the blank can be seen in figure 5-4.

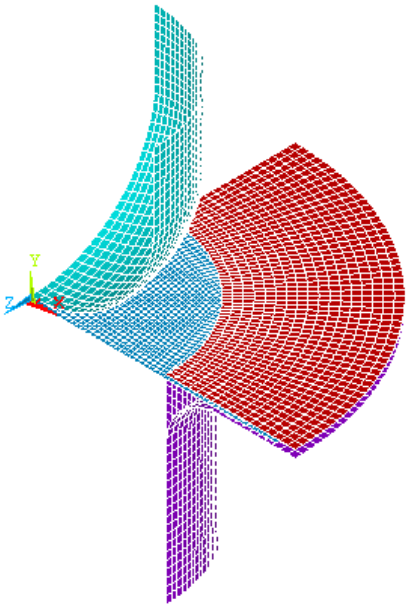

Figure 5-3: Fully Meshed Finite Element Model

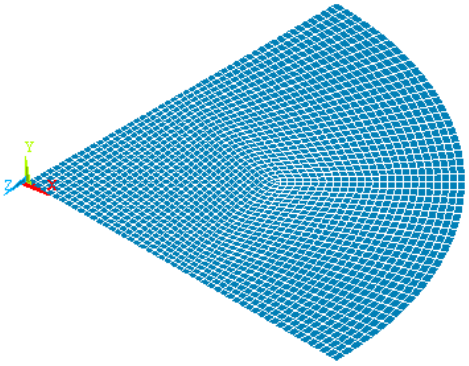

Figure 5-4: Meshed Blank

5.7 Hourglassing Modes and Dynamic Effects

Often during dynamic analyses the stiffness of a part can be dramatically reduced resulting in dynamic effects, or "chatter" in results. Examples of these dynamic effects can be seen in Figures 5-5 and 5-6. Damping systems are often employed in these types of analyses to limit dynamic effects. For this study, a Rayleigh Damping law was used to define the damping constants in the system. The recommended damping constants were found to be 20% mass damping (α) and 1 x 10^{-5} stiffness damping (β) [73]. Damping also eliminates hourglassing effects as the addition of

extra stiffness to the system resists hourglass modes of deformation which can give spurious results.

5.8 Contact and Friction

An automatic surface to surface contact algorithm was used to define the interfaces between the surfaces of the tooling and the blank. This algorithm is based on the penalty method and creates a stiffness between the surfaces to establish contact. This concept is described in more detail in Chapter 3.

As part of the contact algorithm coefficients of static and dynamic friction between the two interacting surfaces were defined in order to accurately simulate the sliding of contact surfaces across each other. An elastic coulomb friction law was assumed and the recommended coefficients of static and dynamic friction were 0.2 and 0.07 respectively [62]. The model was also simulated using dry friction conditions, to simulate the process without lubrication. In that instance the recommended coefficient of static friction was 0.6 [74].

5.9 Boundary Conditions and Loading

As only one quarter of the problem was modelled through symmetry, the nodes of the symmetry edges of the blank were constrained in the appropriate directions. The tooling having been modelled as rigid bodies were constrained during the material model stage. The punch was fixed about all rotations and restricted to only move downwards in a vertical direction along the y-axis, while the die was constrained in all degrees of freedom. The blank holder was constrained in exactly the same way as the punch. As the bulging process was simulated the blank holder moved downwards and exerted the blank holder pressure on the blank. Therefore like the punch, the blank holder was only required to move vertically downwards along the y axis and was constrained in all other degrees of freedom.

When using an explicit dynamic code like LS-DYNA it is often necessary during analyses of metal forming processes to use a non-representative solution time in order to reduce the computational effort required to obtain a solution. This must be balanced by ensuring that the solution time is not reduced to a level where artificial dynamic effects are introduced into the system. It is also important to develop a load profile whereby loads are not suddenly applied at any point, as sudden loading will cause the model to become unstable. Figures 5-5 and 5-6 show dynamic effects in the contact forces resulting from suddenly applied loads to the punch and blank holder respectively.

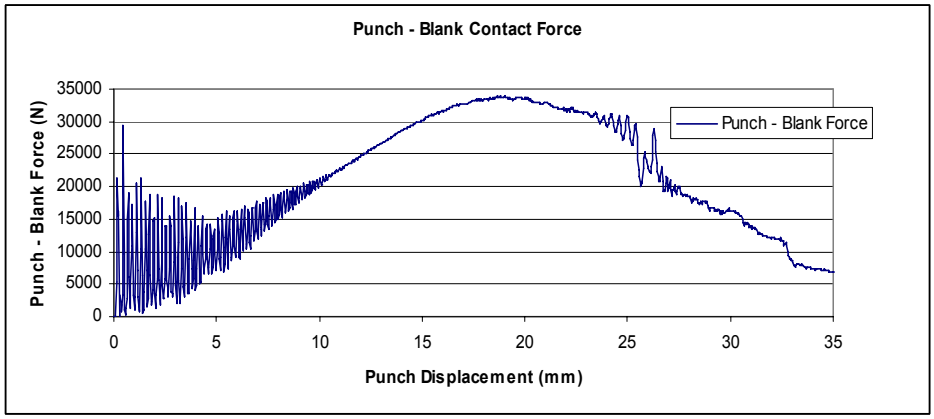

Figure 5-5: Dynamic Effects in the Punch Load [70]

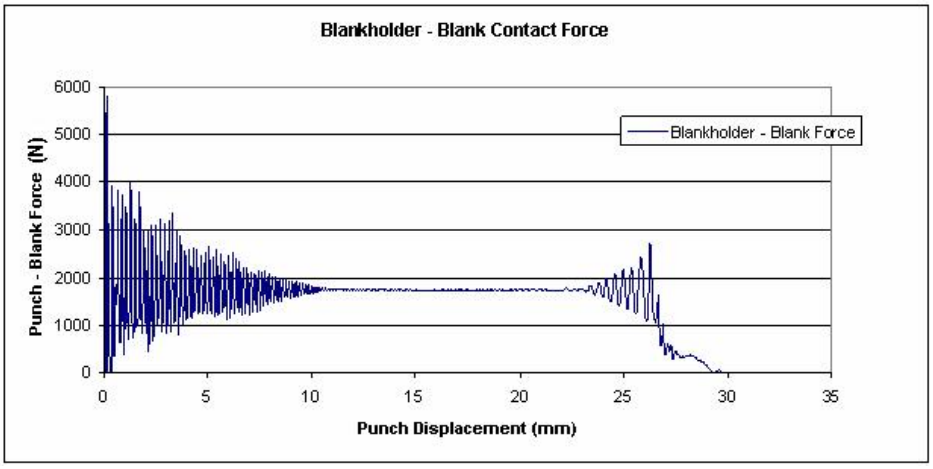

Figure 5-6: Dynamic Effects in the Blank Holder Force [70]

Previous work by Maker and Zhu [73] derived an equation to calculate an appropriate solution time, in milliseconds, for metal forming simulations:

$$\text{Solution Time, } T = 2 + D/2 \qquad (7.1)$$

Where D is the required draw depth in millimetres. A trapezoidal load profile, as shown in Figure 5-7, with a 2ms rise and fall time is recommended. This allows for a "soft start, soft finish" approach which will limit dynamic effects in the system.

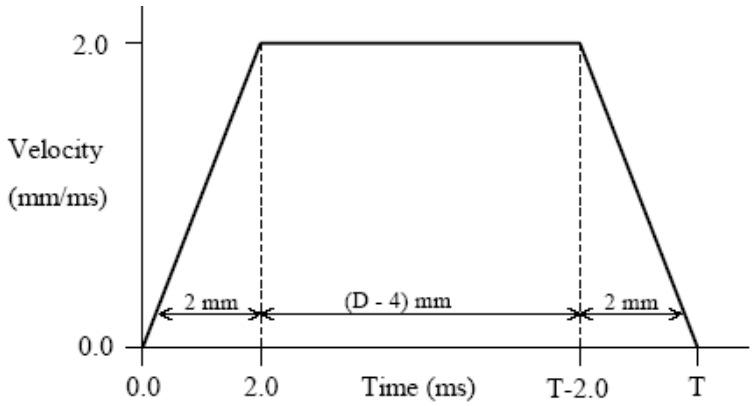

Figure 5-7: Trapezoidal Load Profile as recommended by Maker and Zhu [71]

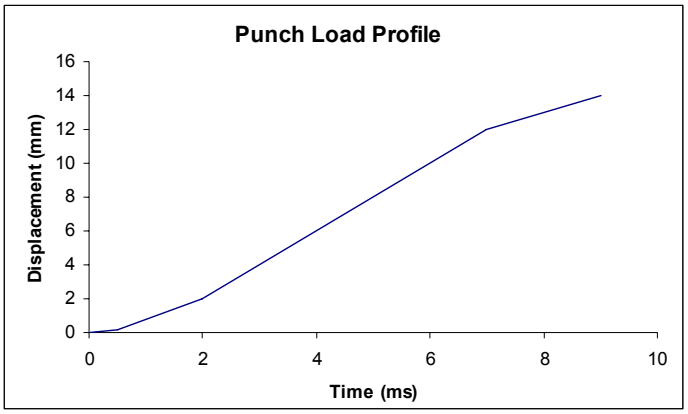

Figure 5-8: Load Profile used in the Finite Element Models

Nielsen [75] stresses the importance of avoiding high velocities when the first point of contact between the materials is reached. In metal forming this occurs when the punch and blank holder make contact with the blank. In this study, a prescribed displacement, equivalent to the punch stroke, was applied to the punch, and a cosine

shaped function was used to incorporate the "soft start, soft finish" as shown in Figure 5-8.

The blank holder force was applied using a trapezoidal load profile similar to that shown in Figure 5-7. In the sheet bulging experiments the blank holder force (BHF) was applied to the blank before the tests began, therefore a 2ms rise time in applying the BHF in the model would result in an inaccurate simulation. A rise time of 0.5ms in the application of the BHF was recommended by Galvin [71], who incorporated trapezoidal load profiles in his work. The blank holder load profile applied in this study is shown in Figure 5-9.

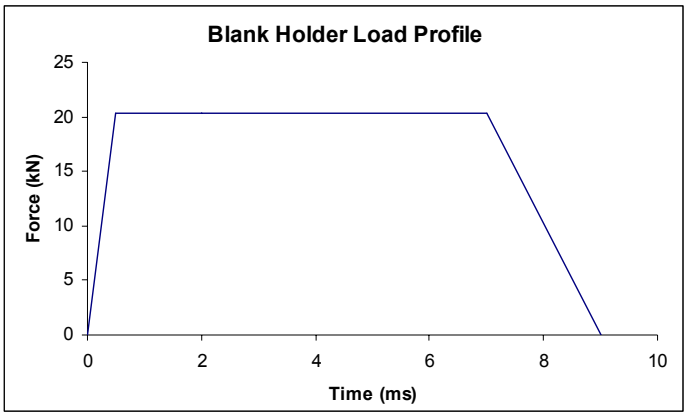

Figure 5-9: Load Profile Used to apply the BHF

5.10 Summary of Chapter 5

This chapter outlined the procedures involved in building a finite element model to simulate the sheet bulging experiments at 100˚C and 150˚C. The modeling methods were described and recommendations were made in choosing various parameters for some of the features, such as coefficients of friction, damping constants and mesh size. The loading profiles and their effect on the dynamic response were examined and the methods behind calculating an appropriate solution time and delay in applying loads were discussed.

Chapter 6: APDL Algorithm

6.1 Introduction

This chapter examines the programming techniques used to implement Oyane's ductile fracture criterion [6] into the ANSYS LS-DYNA post processor. Using ANSYS Parametric Design Language (APDL) a macro was written to predict fracture in a 2D finite element simulation of a sheet bulging process. This macro then evolved into an algorithm that could accurately predict fracture in a 3D model and could also organize and present results in an efficient manner. Some lines of programming code are presented in this chapter to elaborate on the main differences between the various programming techniques used. A full list of the code can be found in Appendix A.

6.2 Takuda 2D Program

In order to calculate the integral value, I, for each element a macro was written using ANSYS Parametric Design Language (APDL) to post process the results from the simulation. Initially a macro was written for a 2D finite element model and validated against previous work done by Takuda [62], who is a respected author in the field of ductile fracture criteria. Figure 6-2 shows the steps involved in the macro in order to calculate the integral. The process is divided into two stages, the first where the stress / strain terms required for Oyane's equation are gathered, and the second stage where the data is sorted and the integral is calculated.

The first stage requires the user to enter the number of result sets in the analysis and the number range of the elements in the blank. The macro loops through each element and gets the numbers of its corresponding nodes. The equivalent and principal stresses as well as the equivalent strain values at each node are obtained. Figure 6-1 shows a section of the code used to obtain the element node numbers (highlighted in blue) and the stress values (highlighted in red). The *GET command

is used to obtain specific data from the model or solution, such as stress values or element numbers. This command is limited to obtaining stress / strain results at nodes only; it cannot be used to directly obtain these results for elements.

```
!finds the node number for particular element
*GET,z_node1,ELEM,%u%,NODE,1
*GET,z_node2,ELEM,%u%,NODE,2
*GET,z_node3,ELEM,%u%,NODE,3
*GET,z_node4,ELEM,%u%,NODE,4

!finds the 3 Principal and Equiv Stresses for each node
*GET,SIG1%z_node1%,NODE,z_node1,S,1
*GET,SIG1%z_node2%,NODE,z_node2,S,1
*GET,SIG1%z_node3%,NODE,z_node3,S,1
*GET,SIG1%z_node4%,NODE,z_node4,S,1

*GET,SIG2%z_node1%,NODE,z_node1,S,2
*GET,SIG2%z_node2%,NODE,z_node2,S,2
*GET,SIG2%z_node3%,NODE,z_node3,S,2
*GET,SIG2%z_node4%,NODE,z_node4,S,2

*GET,SIG3%z_node1%,NODE,z_node1,S,3
*GET,SIG3%z_node2%,NODE,z_node2,S,3
*GET,SIG3%z_node3%,NODE,z_node3,S,3
*GET,SIG3%z_node4%,NODE,z_node4,S,3

*GET,EQUIVSTRESS%z_node1%,NODE,z_node1,S,eqv
*GET,EQUIVSTRESS%z_node2%,NODE,z_node2,S,eqv
*GET,EQUIVSTRESS%z_node3%,NODE,z_node3,S,eqv
*GET,EQUIVSTRESS%z_node4%,NODE,z_node4,S,eqv
```

Figure 6-1 Code used to determine Nodal Stress / Strain Values

From the values obtained with this code, the hydrostatic stress and stress ratio is calculated, and the bracket term (stress ratio plus the Oyane constant ‘a’) from Oyane’s fracture equation is calculated for each node. The nodal results are then averaged to give an overall result for each element and these results are stored in arrays. A comparison between these average nodal stresses and a plot of element stresses show that the values were identical and so this method was valid. Each result set, or time-step of the solution has an associated array and the corresponding results are stored in each one. These steps are repeated for each set of FEA results from the tenth set to the last. The reason the calculations begin at the tenth set of results is that

the initial stress / strain values from the first few time steps are so small that they can be considered negligible. The result arrays were then exported to excel where all the terms of the equation are gathered and the integral calculated for each element in every result set.

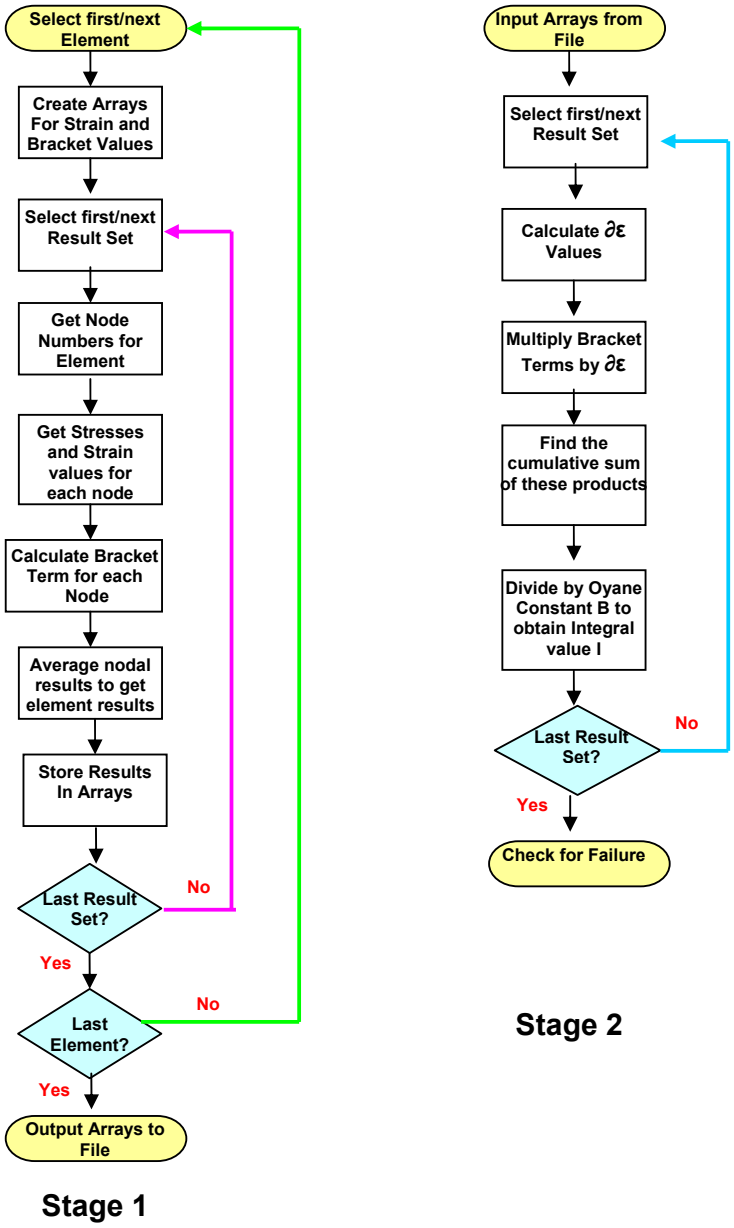

Figure 6-2: Flow chart for 2D APDL Program

The results from the simulation compared favorably from those obtained by Takuda [62] but there were many issues with the macro that needed resolving. Firstly the macro was grossly inefficient. The stress / strain terms were required for each

element, however as it was not possible to obtain them directly, the values were obtained for each node and the nodal results were then averaged to give the element result. This meant a lot more variables and calculations were included in the program than was needed, and this led to increased processing time. The overall processing time to obtain the stress-strain values was forty five minutes. Even more time was required to input and sort the data in Excel. Although the model was inefficient and required a lot of processing time, the results obtained were favourable and so this model became the basis for the next step which was to implement the ductile fracture criterion into a 3D model.

6.3 Takuda 3D Program

Figure 6-5 shows the adapted APDL macro for the 3D model of Takuda's work. Some of the methods used in the 2D macro were infeasible for a 3D model as the large increase in the number of elements to be processed would result in much greater memory consumption and an estimated processing time that could run into days. Therefore an alternative method of gathering the stress and strain terms for each element was required.

In this program the processor goes through each result set, and at every set selects each element in the blank individually and plots its various stress and strain values as shown in Figure 6-3. The values are then directly read off the plots using a macro and used to calculate the stress ratio and the bracket term (stress ratio plus Oyane constant 'a'). The bracket terms and strain values are then stored in arrays which are then output to Excel for further processing in the same way as the 2D model.

Figure 6-4 shows the code used to plot each stress and strain (highlighted in red). The GET commands succeeding each plot command are used to read the maximum stress or strain value off each plot. As each element is plotted individually there will only ever be one stress / strain value in the plot and this can be labelled as the maximum or minimum plot value. In this way there is no need to obtain stresses and strains from individual nodes, now these values can be directly obtained for each

element. It is important to note that there is no difference in element stress values obtained using this method and those obtained by averaging the nodal stresses.

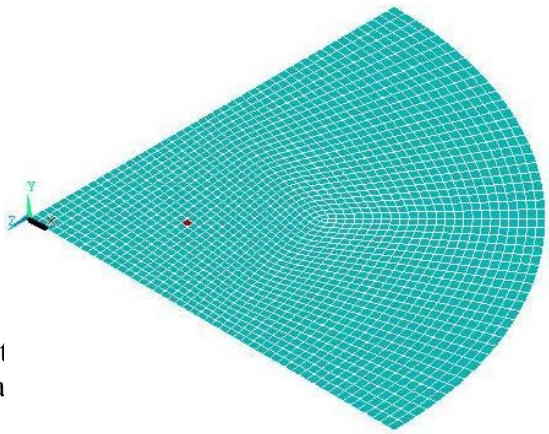

Element St
/ Strain Va

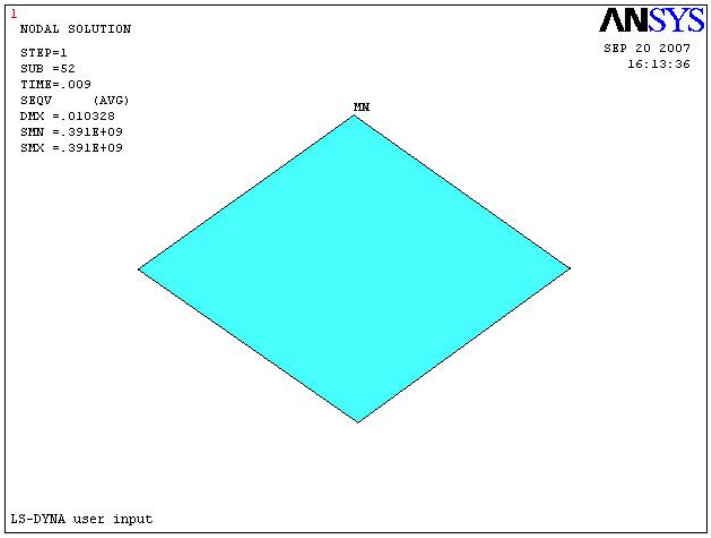

Figure 6-3: Individual element stress plots

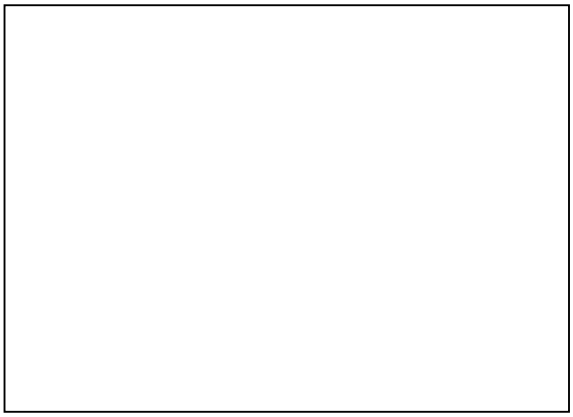

Figure 6-4: Code to obtain stress / strain values through plotting technique

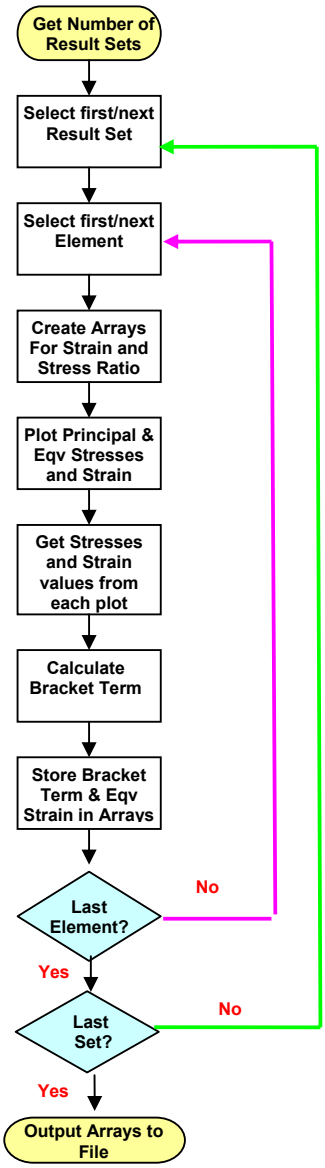

Figure 6-5: Flow Chart for Takuda 3D Program

The method of plotting the stress / strain values for each element and reading off the values from the plots greatly reduced the processing time. The same method when applied to the 2D model took 8 minutes to complete in comparison to the old method which took 45 minutes. For the 3D model the new process took almost 4 hours. The further processing of the data in Excel was also very time consuming, as each array contained thousands of rows corresponding to every element and every result set had a corresponding array. Although this program was an improvement on the previous one and the results obtained more closely matched those of Takuda, a lot more work

was required in order to further reduce the processing time. The ultimate goal was to automate the post processing stage as much as possible where the only manual involvement was to interpret the results. For this to be achieved the integral had to be calculated in the ANSYS post-processor.

6.4 Element Paths

One method of reducing processing time was to create paths of elements through the blank and solve the integral for only these elements rather than for every element in the blank. This would greatly reduce the processing time and make it easier to find the location of fracture in the blank. The numbers of the elements in the blank, with respect to their location were non-sequential, that is to say that two elements located adjacent to each other would not be numbered sequentially. This near random numbering of elements in the blank made it almost impossible to predict their location. This also meant that when failure was detected at a given element, the blank would have to be searched manually to pinpoint the exact location of fracture. Figure 6-6 shows the blank divided up into 9 paths of elements (highlighted in red). These paths were distributed in such a way as to evenly divide up the blank but also to be concentrated at the areas where failure is likely to occur; near the centre [62].

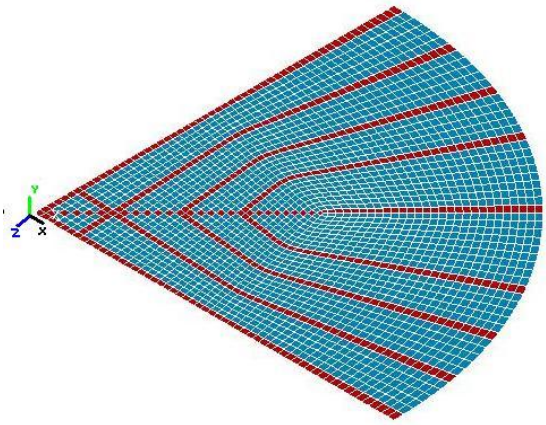

Figure 6-6: Element Paths through Blank

Figure 6-8 shows the steps involved in creating these paths. A separate program was written which starts at the element at the centre of the blank and obtains the number

of the element adjacent to it and then the number of the element adjacent to that element, and so on until the edge of the blank was reached. Every element has a number of adjacent elements surrounding it and their location can be expressed in terms of the side numbers of the original element. Each element has four sides which are numbered and there is potentially an adjacent element located at each one. To select a particular element 'B' adjacent to an original element 'A' the side 'C' that joins the two elements must be specified. In programming terms this is simply written as:

*GET,B,ELEM,A,adj,C,,

The side numbers give the direction of each element path through the blank. The direction of the element paths in the blank can be expressed in terms of being along the direction of the x axis or the z axis. Using the configuration shown in Figure 6-7, a path of elements in the x direction would be adjacent to side 2, while a path in the z direction would require elements adjacent to side 3.

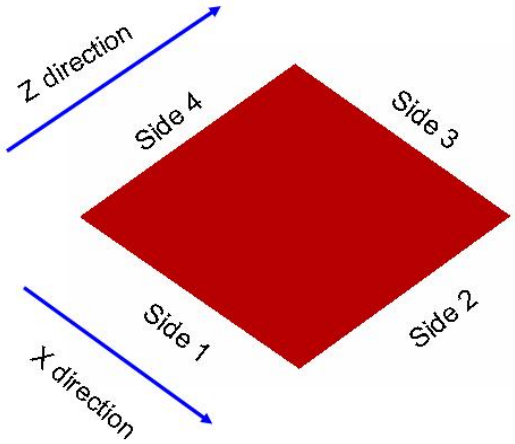

Figure 6-7: Element Configuration

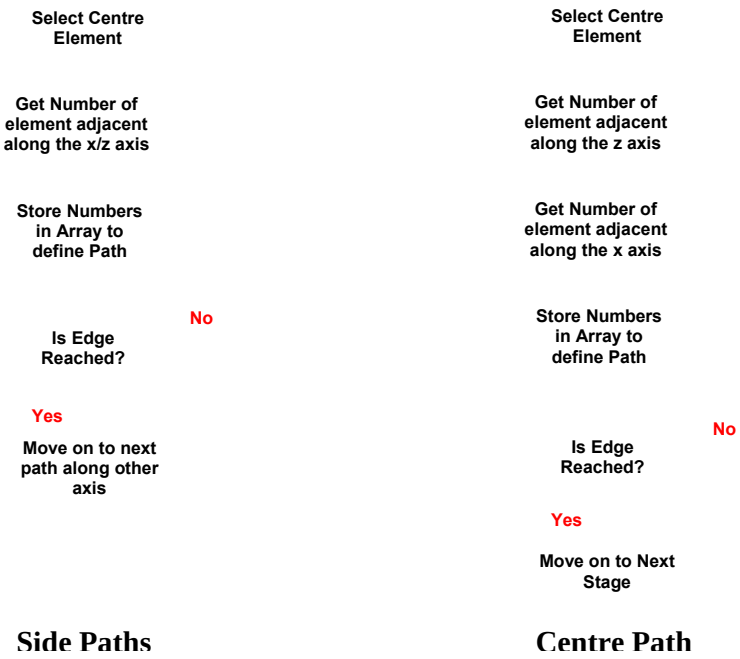

Figure 6-8: Defining Element Paths

The path through the centre of the blank consists of elements that are diamond shaped and are joined at the corners rather than the sides. A separate code had to be written to define this path. Figure 6-9 shows this technique in more detail. Beginning at the centre element, the number of the adjacent element (highlighted in blue), in the z direction is obtained and from this element the number of the adjacent element (highlighted in red), in the x direction is obtained and this value is stored in the array used to define the path.

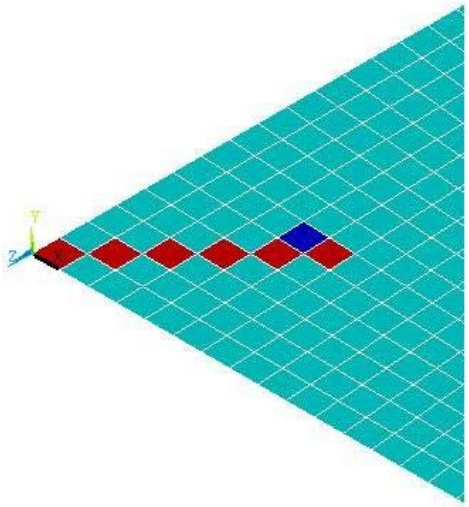

Figure 6-9: Defining the Centre Path

6.5 Distance Array

Every path through the blank contains the same number of elements, as every successive element in each path moves the path one step further out from the centre. The paths travel directly from the centre to the edge, there is no doubling back at any point. The fact that there was the same number of elements in each path made it possible to accurately measure the distance of each element from the centre. For this purpose a distance array was created which had the same dimensions as the path arrays. The blank radius was divided by the number of elements in a path and this gave the distance of a single element from the centre. This value was then used to accurately determine the distance from the centre of any element on any path. Each row in the distance array provided the corresponding distance from the blank centre for each row in the path arrays.

6.6 Modified 3D Program with Element Paths

Each path of elements through the blank was defined using an array of element numbers. These arrays were each given a name and all these names were stored in a single character array. From this character array each path of elements could be selected individually for processing by selecting the path name. Figure 6-10 shows the improved post processing program that implements the element paths and further builds on the methods of the previous program. Again the program is divided into the two processes of obtaining the data and then performing calculations, only this time the processes are all done entirely in the ANSYS post-processor. During the first stage the macro obtains the number of results in the solution. It then loops through each of these beginning at the tenth time step. Within this loop are two nested loops where each path is selected in turn, the elements defining the chosen path are then selected individually, the stresses and strain are plotted and the results read from the plots and stored in the corresponding path bracket term / strain arrays. The introduction of the element paths greatly reduced the processing time from 4 hours down to 45 minutes.

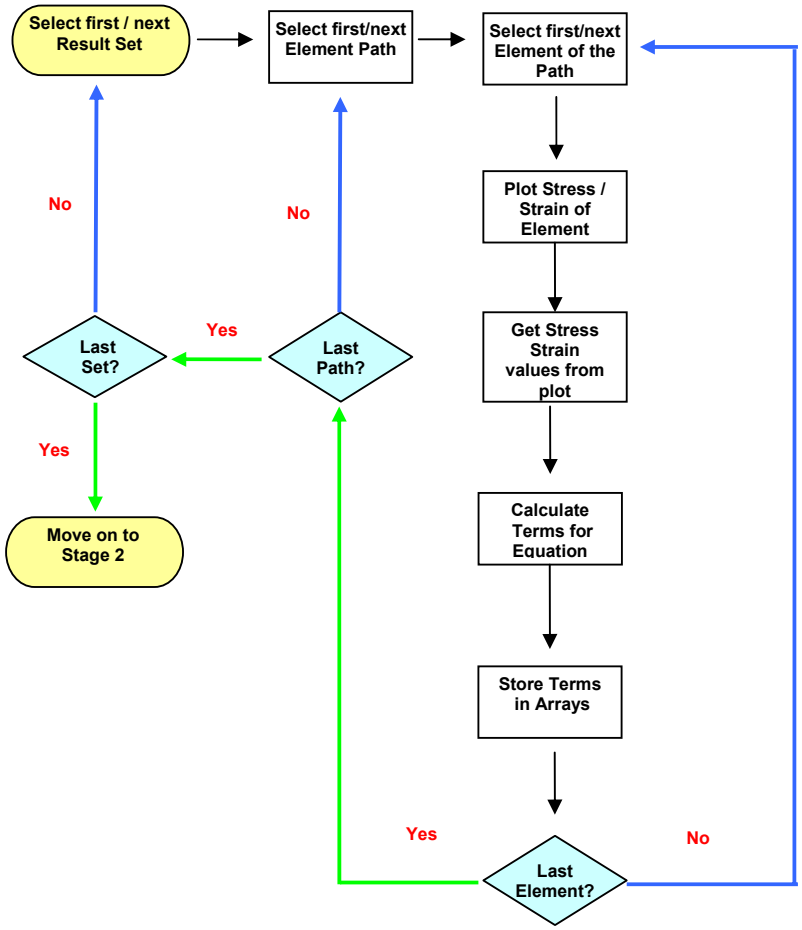

Figure 6-10: Implementing Paths into the Program

The second stage (Fig 6-11) is very similar to the manual operations carried out in Excel although now every step of the integral calculation was performed automatically in the post-processor. Further research into the APDL programming language led to the *VOPER command which would perform various mathematical operations on arrays. These operations were performed on each element path through every set of results. The overall result of the calculations were arrays of the Oyane's integral, I, for each path through every time step, which meant it was possible to study the evolution of fracture along each path at every stage of the forming process.

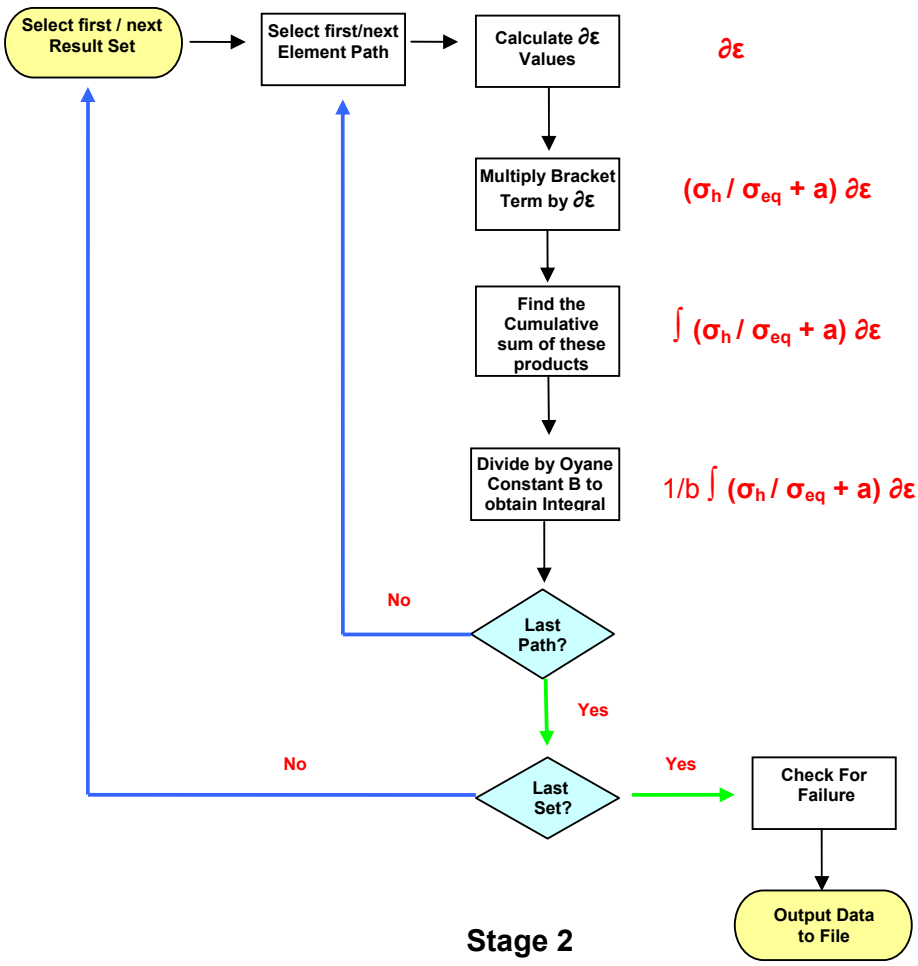

Figure 6-11: Calculation of Results using the Post-Processor

6.7 Failure Checks

Further development in the program allowed the processor to check the Oyane's integral I arrays for failure. The program looped through each path and its corresponding arrays of I values checking each one individually to see if any of its values were greater or equal to one and recording the result set of the first instance were it was detected. The row number of the array was noted and the corresponding row number in the distance array provided the location of fracture. The corresponding result set was plotted and the depth of draw at failure was recorded.

6.8 Output Data

The results from the failure checks for each path were stored in a single table which was written to file. The format of this table is shown below in Table 6.1. Each row in the table contains the failure data for each path. If failure was not detected on a particular path, then the row it would occupy in the table was filled with zeros. In the case of an analysis where failure did not occur, the entire table was filled with zeros.

Table 6.7: Result Table Format

No of Path	I Value	Element No	Distance From Centre	Result Set No	Depth of Draw
1					
I					
9					

Similar checks were performed to find the maximum I values for each path and this data was stored in an identical table. This data was very useful to examine in analysis where ANSYS did not predict failure. Once the output of data was complete the next model was automatically read in.

At this point the program was fully automatic with no manual interference. The FEA model would be solved, the post processor would calculate the Oyane's Integral, this would be checked for failure and the results for each path would be gathered in a table and written to a file bearing the model's name, before the next input file was read in. In this way many models could be run sequentially without manual interference except to review results and make necessary alterations to future models.

6.9 Element Table Method

Further investigation of APDL methods uncovered a new method of obtaining stress / strain values from the elements. This method, shown in Figure 6-14, eliminates the plotting technique used in previous programs and instead uses the element table

function. This function stores result data for any elements currently plotted on screen in a table, along with the corresponding element numbers. So instead of each element being plotted individually and the results read off the plots, every path was plotted together (Figure 6-12) and the results for each element were gathered simultaneously and stored in an element table.

The code involved to create element tables is shown in Figure 6-13. Separate element tables were needed for each type of stress and strain and these tables were created at each time step. The results from the element tables were then sorted into result arrays for each path by matching every element on each path to the corresponding results in the element table.

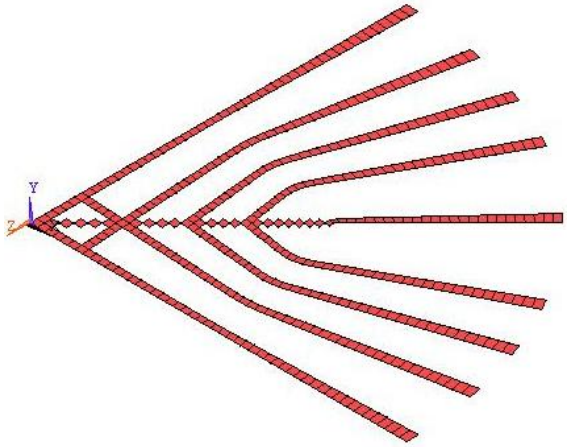

Figure 6-12: Element Paths selected for Element Tables

Figure 6-13: Code Used to Create Element Tables of Results

The other stages of the program such as integral calculation, failure checks and outputting data remained the same as the previous method. The element table method proved to be the most efficient and least time consuming of all the methods with a

processing time of just 40 seconds. With the combined time of the other stages the total post processing time was approximately 70 seconds. The results obtained with this method were identical to those obtained with previous programming techniques.

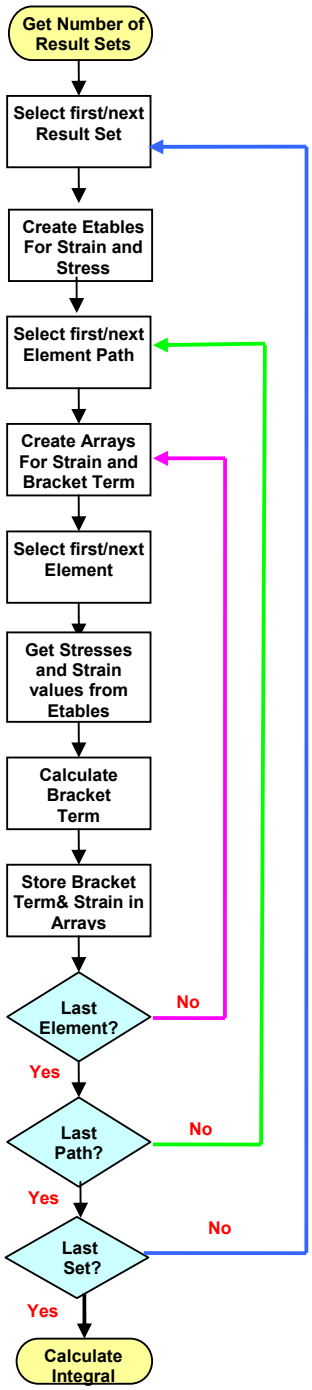

Figure 6-14: Implementing Etables into the Program

6.10 Summary of Chapter 6

This chapter examined the various programming techniques used to write an APDL program to implement Oyane's criterion into the finite element model. A number of programs were written each with the goal of calculating the integral values while reducing processing time and human involvement. Each program built further on its predecessor until a satisfactory level of automation and processing time was reached. The evolution of the programming techniques involved:

- A 2D macro that obtained the average nodal stress – strain to calculate terms for Oyane's equation.

- A 3D program that plotted the stresses and strain of each element in the blank individually and gathered the required stress – strain values from these plots to calculate the terms for the fracture criterion.

- The introduction of element paths through the blank where the integral was solved for only these elements rather than for every element in the blank. This greatly reduced processing time and made it easier to find the location of fracture in the blank.

- The introduction of the Voper command allowed the integral to be calculated entirely in ANSYS rather than exporting the stress strain terms to Excel for further calculations. Together with the failure check macro, which checked each integral result for failure, and the output macro which determined the location and depth where fracture occurred, the programs became fully automated and human involvement in the determination of fracture was minimal.

- A 3D program that replaced the previous method of plotting each blank element individually with the element table method. This method obtained stress – strain values for all the paths of elements simultaneously and stored the results in an element table. This method greatly reduced the processing time without a loss of accuracy in the results.

Chapter 7: Results and Discussion

7.1 Introduction

This chapter outlines the results from both the physical sheet bulging experiments and the finite element simulations of these experiments. The results from physical testing are compared to the FEA results in terms of prediction of depth at failure, location of fracture and the punch load curves. A failure range is employed in order to improve the accuracy of fracture prediction in the FE model, and statistical analysis is employed to examine the effects of variance in material properties on the prediction of fracture.

7.2 Experimental Sheet Bulging Results

Experimental sheet bulging of AZ31 sheets were carried out at 100° and 150° Celsius. During the experiments both the die and blank holder were heated to the forming temperatures, while the punch remained at room temperature as recommended by Yoshihara [76]. A constant punch velocity of 50mm/min was used for each test. The sheet bulging procedure and apparatus is discussed in more detail in Chapter 4.

7.2.1 Results at 100 Degrees

Figure 7-1 displays some bulged specimens of AZ31 formed at 100°C. Early samples tested showed signs of wrinkling which indicated that the blank holder force was inadequate. This wrinkling continued to appear in samples until the blank holder force was raised to the rigs maximum capacity of 20.4 kN. This value was then used continually throughout testing for both temperatures.

Figure 7-1: Bulged samples of Magnesium AZ31 formed at 100°C

Table 7.1 displays the physical test results for samples formed at 100°C in terms of the forming depth at failure and the maximum load, or load at failure. A graphical representation of these results is shown in Figure 7-2.

Table 7. 1: Experimental Sheet Bulging Results at 100°C

Sample No	Failure Depth (mm)	Max Load (kN)	Location (mm)
1	10.8	6.49	6.2
2	12.8	8.48	4.6
3	10.9	6.60	4.83
4	11.34	6.88	4.7
5	10.6	6.18	6.85
6	11	6.50	5.85
7	12.1	7.65	6.55
8	14.9	10.07	5.16
9	12.5	7.47	6.65
10	12.4	8.06	7.6
11	15.4	10.57	8.32

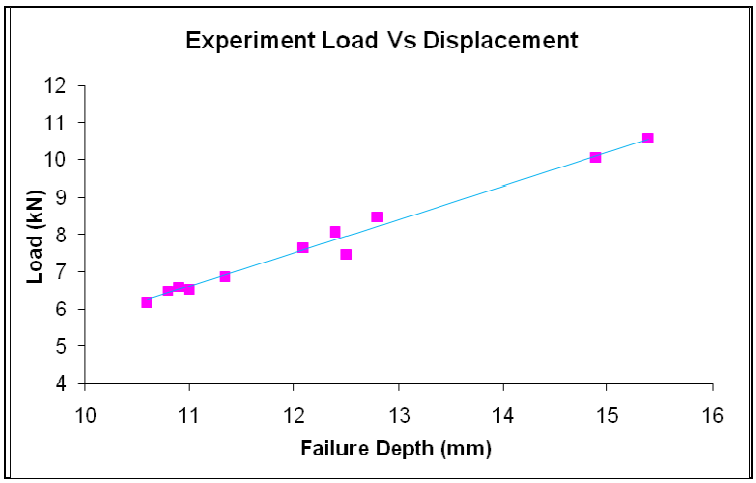

Figure 7-2: Plot of Experimental Results at 100°C

The graphical representation of the results in Figure 7-2 raises some interesting observations regarding the distribution of results. From the graph it is clear that the results are linear and there was some scatter, most notably there are two results on the right side of the plot around 15mm that are separate from the main group. The results were also concentrated in three clusters around 11mm, 12.5mm and 15mm. There are a number of possible reasons for this scatter of results and the occurrence of these clusters, namely heat transfer and the method in which the blank holder force was applied.

As described in Chapter 4, the die and blank holder were heated during testing using a heater band that covered the outer wall of the die. As the die was heated some of the heat was transferred to the blank holder and in this way it was also heated. The temperature was controlled using a thermocouple which measured the temperature in the centre of the die and a thermostat which maintained the temperature at a constant level.

Due to the thickness of the die it took approximately 25 minutes to reach 100°C. During this time, the blank holder, having a much smaller geometry than the die, reached the forming temperature first and had surpassed it by approx 10° - 15°C by the time the die reached 100°C. To combat this problem the heating apparatus was turned off completely for a few moments in between experiments to allow the blank holder to lose its excess heat. The die's extra thickness and insulation with the warm heater band meant it had a slower rate of heat dissipation than the exposed blank holder. The heating apparatus was turned back on for the experiment and temperature measurements showed that the temperatures of both components were approximately equal. The temperature of the blank holder varied slightly for each experiment and this helped to contribute to the scatter of results.

The two results on the right side of the plot were from tests where the temperature difference between the die and blank holder was high. On these occasions there was difficulty in applying the blank holder force to the blank. As previously outlined in Chapter 4 the blank holder force was applied using four springs which when under compression exerted a force on the blank holding plate. Each spring had a small steel cap on one end where a threaded bolt could press into the cap and thus compress the

spring. These caps had to be aligned correctly so that they would not interfere with the punch as it formed the blank. Usually this was achieved without difficulty but in the case of these two tests the caps were misaligned as the springs were compressed and the process had to be repeated. During this time the temperature of the blank holder had continued to rise together with that of the blank. So in actual fact the results of these two specimens were not for a forming temperature of 100° but for a higher temperature around 110°C - 115°C.

The location of fracture varied approximately between 4 – 8mm with an average of 6.1mm. Generally the location of fracture was further from the centre as the failure depth increased. This would suggest that the reason for the variance in the location of fracture was linked to the causes behind the variance in bulge depths at fracture.

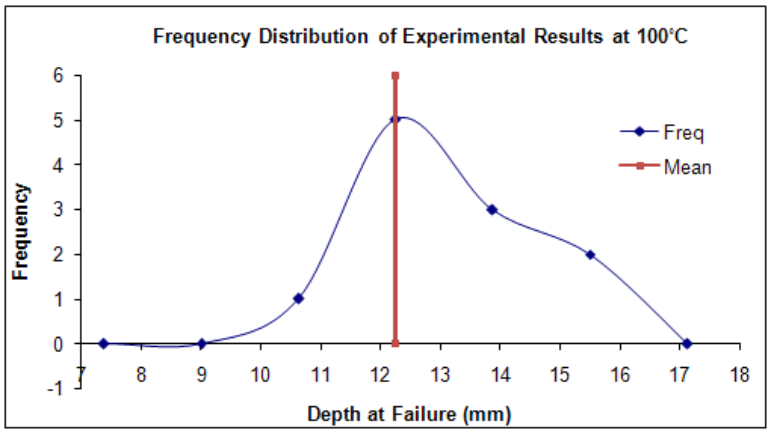

Figure 7-3: Frequency Distribution Curve of Experimental Results at 100°C

Figure 7-3 outlines the frequency distribution curve of the experimental failure depths at 100°C. The distribution of the experimental results is not normal as the curve is skewed to the right of the mean. The mean depth at failure was 12.24mm and the standard deviation was 1.62. The standard deviation was high due to the two samples formed at 110°C - 115°C which produced a large range in the results of 4.8mm. Excluding these two samples the standard deviation value is almost halved to 0.84, and this is a better indication of the spread of the results. Theoretically at least 95% of the experimental results should fall within the range of the mean plus and minus three times the standard deviation. This results in the range 7.3 – 17.1mm, in which all of the experimental results fell into. It was important to verify that the

experimental data obeyed this principle as the same empirical rule is used later on with the FE models to create a confidence level in the prediction of failure depth.

7.2.2 Results at 150 Degrees

At 150°C it was necessary to conduct two sets of experiments as the first set of results failed to produce the required fractured specimens. This set of experiments was conducted using precisely the same conditions as those for 100°C, however the increased formability of the material at the higher temperature meant that the blanks formed without fracture as they were drawn completely into the die. Only one fractured sample was produced. To counteract this increase in ductility a second set of experiments was done using no lubrication between the blank and tooling. In this set fracture was produced in all samples.

Table 7.2 lists the results from the first set of experiments. Apart from sample number 4 where failure occurred at 21.6mm, the other samples were bulged without fracture to a depth of 25mm.

Table 7. 2: Experimental Sheet Bulging Results at 150°C

Sample No	Max Depth (mm)	Max Load (kN)
1	24.99	13.66
2	24.99	14.83
3	25.00	14.70
4	21.61	13.11
5	25.00	15.96
6	25.00	15.96
7	25.00	14.87
8	25.00	15.43
9	25.00	14.44
10	25.00	13.51
11	25.00	15.10

A graphical representation of the data in Table 7.2 is shown in Figure 7-4. There was very little scatter in these results as only one specimen had failed. There was some variance in the maximum load between the samples but this can be accounted for by variances in the temperature of the blank holder and blank, while there were also small deviations in the amount of lubrication in each experiment.

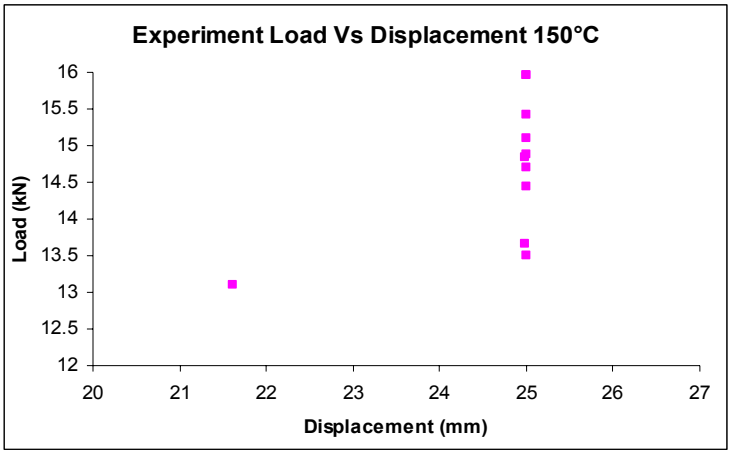

Figure 7-4: First Set of Experimental Results at 150°C

The lubricant used in each test was copper based delivered in an oil solution. The lubricant itself was suitable for temperatures up to 1100°C as the copper particles had a high melting point, but the oil solution that it was delivered in provided some problems. At 150°C the oil evaporated producing a large amount of smoke which made it infeasible to apply lubricant to the hot die or blank holder for every test as it made it very difficult to correctly centre the blank and apply the blank holder force. Both the die and blank holder components were lightly lubricated just once, at the start of testing and after the oil had evaporated the copper particles coated the tooling for the duration of the experiments. The amount of this copper coating varied slightly throughout the testing. Each blank was lubricated individually, and after forming some of the blank's lubricant would be transferred to the tooling and vice versa.

Other authors have taken this approach and have lubricated only the blank during high temperature forming of magnesium alloy. Takuda has applied various types of lubricant to AZ31 blanks such as: sprayed wax [54], Vaseline [62], and Teflon [53] while Yoshihara et al. [77, 78] applied graphite grease to the blank. All these lubricants consist of a petrochemical element that would evaporate or could even burn at high temperatures and create difficulties when applied to hot tooling.

There are a few possible reasons why one of the samples failed while the other ten did not. It is possible that the material properties of that particular blank were slightly different than the others. It is also possible that the blank was insufficiently lubricated and this resulted in high frictional forces in the process. These experiments

were similar to the experiments at 100 degrees, there was some temperature variance in the blank holder which caused the blanks to be formed at slightly different temperatures in each test and in this case it may have been formed at a slightly lower temperature than the other blanks, thus reducing its ductility and increasing the risk of fracture.

Table 7.3 displays the results from the second set of experiments done at 150°C. In this set of experiments there was no lubricant applied to the blank or tooling, and as such all tests resulted in fracture. The depths at fracture ranged from 7.75 – 11.5mm.

Table 7. 3: Experimental Sheet Bulging Results at 150°C

Sample No	Failure Depth (mm)	Max Load (kN)	Location (mm)
1	10.69	6.98	9.14
2	11.5	7.48	9.4
3	10.78	6.97	9.62
4	9.7	6.85	8.4
5	9.2	4.94	7.06
6	7.93	5.76	5.83
7	7.75	4.88	5.94
8	10.45	5.7	8.9
9	9.52	5.74	7.52
10	9.33	5.83	7.45
11	8.65	5.12	5.58

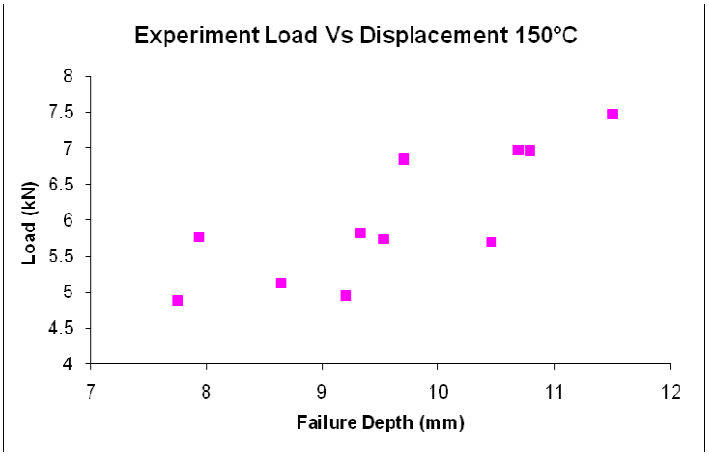

Figure 7-5: Plot of Experimental Results without Lubrication at 150°C

The distribution of the results in Table 7.3 is shown in Figure 7-5. This set of experiments produced more scatter in the results than any of the previous tests. The absence of lubrication meant that the effects of sticking were more prominent in this set. In previous sets of results (Figures 7-2 and 7-4) the maximum load increased with failure depth. In this set the maximum load fluctuated as the displacement increased rather than rising steadily as before. Sticking effects caused samples to undergo large frictional forces which resulted in early fracture. The magnitude of sticking varied from sample to sample and together with variances in blank holder temperature produced this set of scattered, variable results.

Figure 7-6 outlines the frequency distribution curve of the experimental failure depths at 150°C. Again the distribution of the experimental results is not normal but there is less skew in the distribution than at 100°C. The mean depth at failure was 9.59mm and the standard deviation was 1.19. The standard deviation was high due to the varying sticking effects present in some of the experiments which greatly influenced the depth at failure and produced a range in the results of 3.75mm. The 95% confidence limits of the mean plus and minus three times the standard deviation produced a range 6 – 13.2mm, in which all of the experimental results fell into, thus verifying that the experimental data complied with the empirical limit rule, and that a probabilistic analysis using the FE model could be conducted to improve prediction of failure among this set of data.

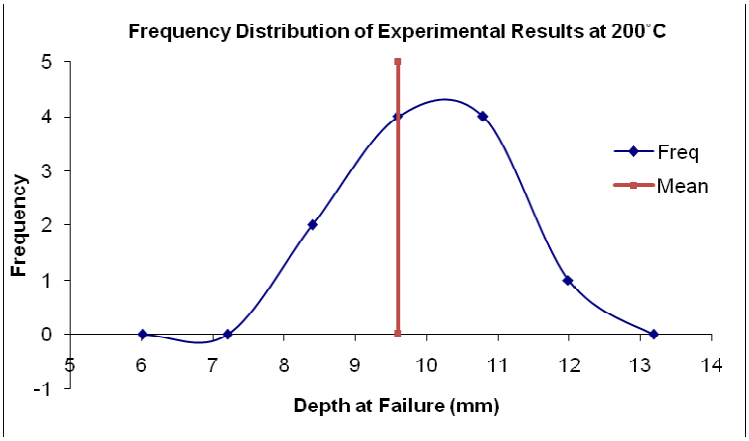

Figure 7-6: Frequency Distribution Curve of Experimental Results at 150°

The location of fracture in the samples varied from 5.5 – 9.6mm from the centre of the blank. As previously mentioned the location of fracture was influenced by the depth at which fracture occurred. In this set of experiments there was a lot of variance in the bulge depths at fracture and this was reflected in the measurements of fracture location.

7.3 Initial Finite Element Results

Three finite element models were built to simulate the sheet bulging experiments at 100°C and the two experiments at 150°C. Oyane's ductile fracture criterion [3] was implemented into the models to predict fracture for each analysis. The blank was divided into nine paths of elements along which the fracture criterion was calculated. An APDL program was written to calculate Oyane's integral and the results were stored in a table which outlined the results for each path. The paths were numbered from one to nine and their configuration is shown in Figure 7-7.

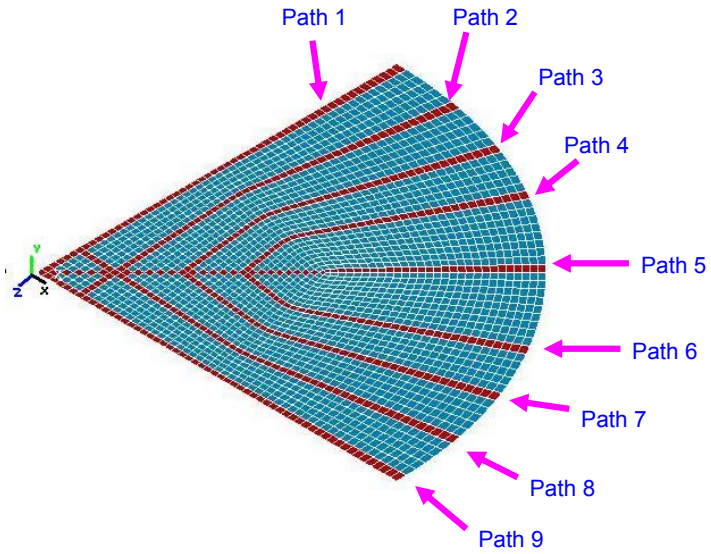

Figure 7-7: Layout of Path Numbers in the Blank

7.3.1 Results at 100 Degrees Centigrade

As previously discussed earlier in the chapter when outlining the experimental results at 100°C, heat transfer corrupted the experiments for two of the eleven specimens

and resulted in these samples being formed at a higher temperature, around 110°C - 115°C. Since these samples had already created a large deviation in the set of result data and also did not represent the behaviour of the material at 100°C it was decided to omit them from the rest of the report.

Table 7.4 shows the fracture results for each path at 100°C. At each path Oyane's integral at fracture is listed together with the predicted bulge depth at failure. The element number and its distance from the centre of the blank pinpoint the location of fracture. The result set, or time step pinpoint the earliest occurrence of fracture in the blank.

Table: 7.4: Finite Element Results at 100 degrees

Path	Integral I	Element No.	Location (mm)	Result Set	Depth (mm)
1	1.0032	3857	6.8	36	11.886
2	1.0004	3763	9.9	36	11.886
3	1.0079	3889	6.1	37	12.285
4	1.0079	3889	6.1	37	12.285
5	1.0079	3889	6.1	37	12.285
6	1.0079	3889	6.1	37	12.285
7	1.0079	3889	6.1	37	12.285
8	1.0079	3915	6.8	37	12.285
9	1.0152	4065	6.8	36	11.886

The results of the table show that Oyane's integral was greater than 1 in all cases and hence fracture was predicted on all paths. Taking the earliest occurrence of fracture it can be stated that the model predicts failure at a depth of 11.88mm along three paths. The location of fracture along these paths is at 6.8mm for two paths and 9.9mm for the third. These locations are with respect to the original unformed blank, and were determined by matching the elements where fracture was predicted with their corresponding location in the distance array, as discussed in Chapter 6. Examining the location where fracture occurred on the remaining paths it can be seen that it was around 6.1mm, so all the paths with the exception of one predict a fracture location between 6 – 7mm. Therefore the value of 9.9mm was considered an anomaly and the prediction of 6.8mm was more accurate.

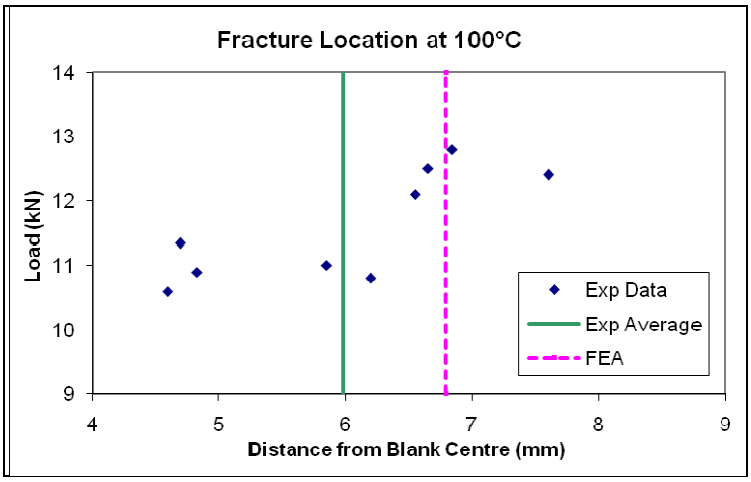

Figure 7-8: FEA & Experimental Fracture Location at 100°C

Figure 7-8 outlines the comparison of the location of fracture in the experimental results with the FEA predicted value. The green line represents the average location of fracture for the experimental results, which was 5.98mm, while the pink dashed line represents the FE predicted location; 6.8mm. The FE model provided an accurate prediction for the location of fracture which was 13.7% off the average experimental result. Again there was some scatter in the experimental data but this was due to the varying depths where failure occurred which had a large influence on the location of fracture. Generally the location of fracture was further from the centre as the failure depth increased and in the experiments at 100°C there was some variance in the failure depth of the samples which led to scatter in the fracture location measurements.

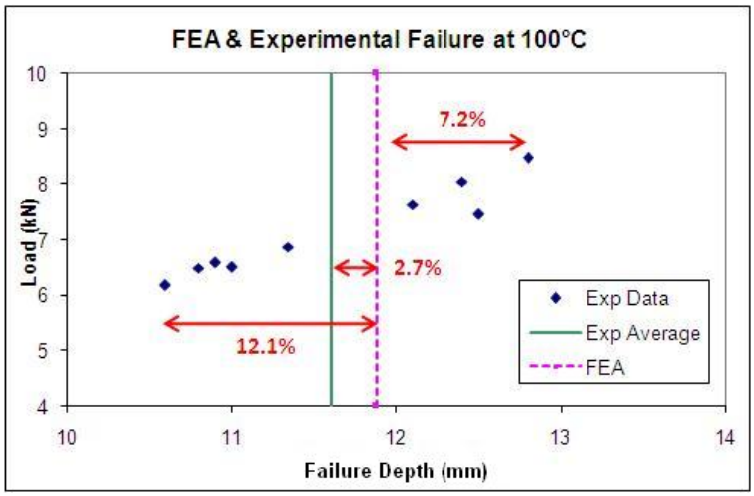

Figure 7-9: Accuracy of FEA Predicted Fracture in Comparison to Experimental Results

Figure 7-9 displays the distribution of failure from the experimental results at 100°C. The pink dashed line represents the FEA predicted failure at 11.88mm, while the green line is the average failure depth of the experimental results; 11.6mm. As previously discussed during the analysis of the experimental test results, the results conjugate into clusters around 11mm and 12.5mm. The FEA predicted fracture was within 12.1% of the experimental values in the first cluster and 7.2% of results in the second cluster. The FE model accurately predicts fracture with a predicted value that is just 2.3% off the average of the experimental test results.

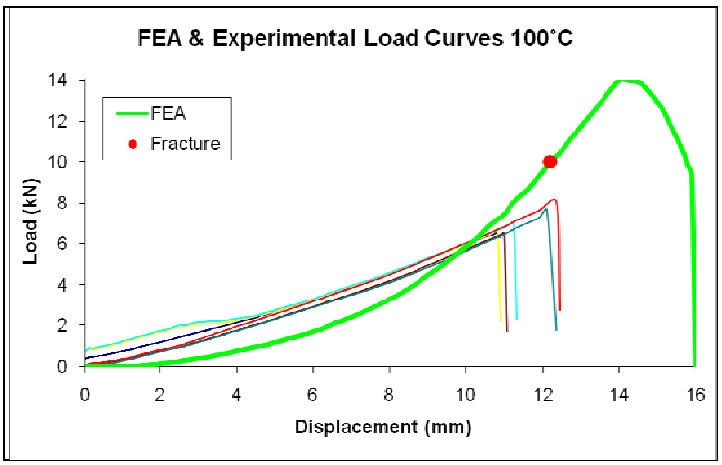

Figure 7-10: Comparison of FEA & Experimental Load Curves at 100°C

Figure 7-10 outlines the evolution of the FEA calculated punch load curve in comparison to those measured during the experiments. The thick green line outlines the FEA punch load curve while the remaining lines display the punch load curves for each experimental sample. The most apparent observation is that in the FE model the load continues to increase even after fracture has been detected. This is simply because, unlike reality, there is no link between fracture and punch load in the model. Oyane's criterion was applied separately in the post processor and had no influence on the load curve. The punch load curve was instead dictated by the load profile that was applied to the punch.

Figure 7-11 shows the load profile used to apply displacement to the punch. The amount of displacement applied was determined by the largest failure depth from experimental results. The load profile had a soft start - soft finish approach to reduce

dynamic effects in the model [73]. These effects and the method for applying the displacement are outlined in more detail in Chapter 6. In the load profile there were three stages; the first where the load was applied gradually at the beginning, then the second stage where it sharply increased after 2mm and finally the soft finish after 14mm. The pattern of the load profile was reflected in the FE predicted punch load curve in Figure 7-10. The load dissipates at 16mm, not because of failure but because no more displacement was applied to the punch at that point and hence the load was zero.

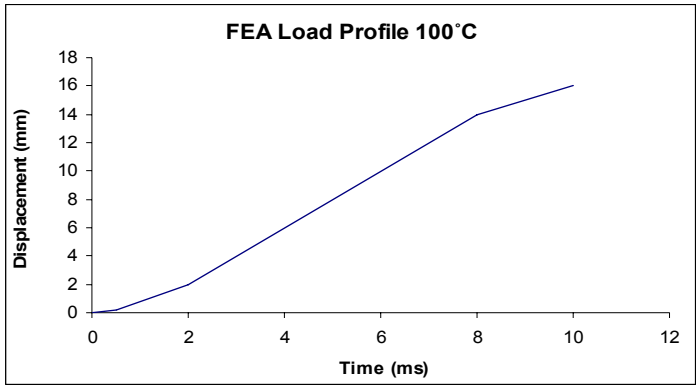

Figure 7-11: Punch Load Profile at 100°C

Because of the limitations of the load profile when modeling suddenly applied loads it is difficult for the FEA punch curve to completely reflect what occurs in reality. Instead it is more beneficial to examine the FEA predicted load at fracture which was 9.05 kN. This compares reasonably well to the average experimental failure load of 7.43 kN which was an offset of 17.9%.

7.3.2 Results at 150 Degrees

There were two finite element models built for analysis at 150°C, one under normal friction conditions ($\mu = 0.2$) and the other with a high friction coefficient ($\mu = 0.6$) to simulate the experiments where no lubrication was used. Table 7.5 shows the finite element results under normal friction conditions i.e. with lubricant. The integral reached unity only on path 1, at a depth of 24.26mm. The other paths were close to fracture with integral values around 0.9.

Table 7.5: Finite Element Results for Normal Friction at 150°C

Path	Integral I	Element No.	Location (mm)	Result Set	Depth (mm)
1	1.025	4705	20.5	49	24.26
2	0.8611	3788	9.1	42	21.62
3	0.944	3768	9.9	44	22.78
4	0.9362	3889	6.1	41	21.04
5	0.9362	3889	6.1	41	21.04
6	0.9362	3889	6.1	41	21.04
7	0.9362	3889	6.1	41	21.04
8	0.8801	3921	11.4	41	21.04
9	0.8468	4069	9.9	40	20.46

The location of fracture was 20.5mm from the blank centre which was extremely far from the centre in comparison to the other paths, however it accurately predicted the location in fracture of the experimental sample which was at 20.76mm. Upon closer examination of the results it was discovered that a wrinkle had occurred on this path at the exact point where fracture was predicted (Figure 7-12)

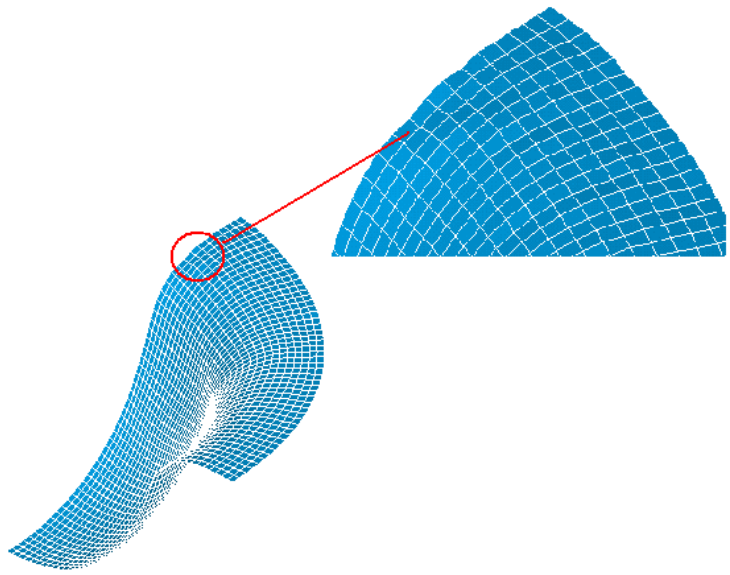

Figure 7-12: Location of Wrinkle in the Blank

This wrinkle meant that there was large deformation of the blank at this point which implied that a high strain value was present. This was confirmed by a plot of the equivalent strain (Figure 7-13) which showed an intense concentration of high strain at the point of fracture. This meant that the $\delta\varepsilon$ value in Oyane's equation was greatly

amplified by the wrinkle and resulted in an artificially high value of Oyane's integral at this point. A check of the other elements on the path outside the wrinkle showed that fracture had not occurred at any other location, therefore this prediction of fracture was inaccurate, and the results from the other paths were considered instead. This false prediction of fracture also highlights some discontinuities that can be associated with boundary conditions. The wrinkle predicted by the FE model did not occur in the experimental samples and could be a result of discontinuities associated with the constraints placed along the blank edges, although no such problems were encountered during the other simulations.

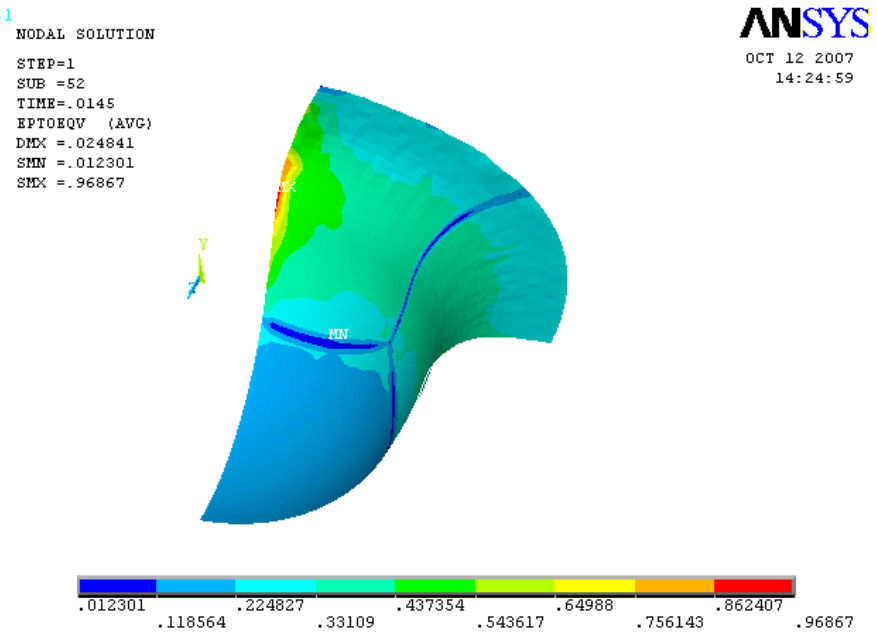

Figure 7-13: Concentration of Equivalent Strain in the Wrinkle Region

From the integral values on the other paths the model predicted that failure did not occur but the blank came close to fracture with a maximum value of 0.94 on path 3. This compares well to the experimental results where out of eleven samples only one failed at a depth of 21.6mm. The depth where the integral reached its maximum value was 22.78mm which was 5.18% in excess of the experimental fracture depth. The model correctly predicted that the most likely place for fracture, should it occur, was around this depth, however the location where fracture was most likely to occur was 9.9mm from the centre which was considerably far from the actual location of fracture of the failed sample (20.76mm from the centre).

Figure 7-14 compares the evolution of the punch load curves from the experimental and FEA results. As previously stated, the punch load curve from the FE model was governed by the loading profile which determined the shape of the curve. The punch load curve from the finite element model underestimated the forces involved in the experiments at every stage. Apart from the influence of the load profile, this deviation between the finite element and experimental load curves could have been caused by an incorrect modeling of sticking effects and frictional forces. Experimental results showed that at 150°C sticking effects became more prominent in the tests and this was reflected with larger punch force values particularly in the early stages of forming. Despite this the difference between the maximum FEA and average maximum experimental punch force was just 2.61kN which was a variation of 17%.

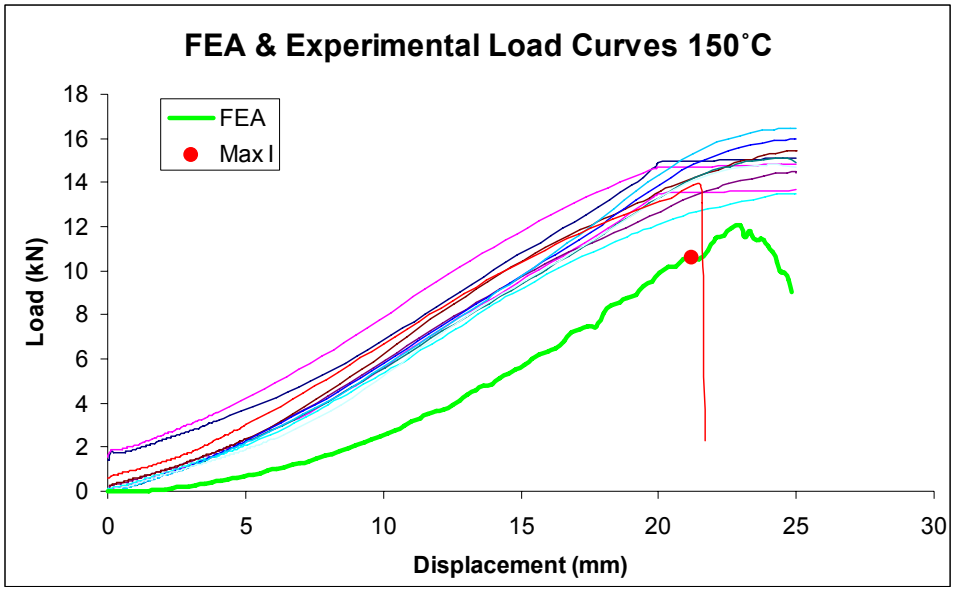

Figure 7-14: FEA & Experimental Load Curves for Results with Lubrication at 150°C

Table 7.6 shows the fracture results for the FE model at 150°C under high friction conditions where no lubrication was used in the experimental testing. The results show that the earliest occurrence of fracture was predicted on path 9 at a depth 10.76mm.

Table 7.6: FEA Fracture Predictions for second set of results at 150°C

Path	Integral I	Element No.	Location (mm)	Result Set	Depth (mm)
1	1.0196	3732	10.6	45	10.92
2	1.0007	3763	9.9	45	10.92
3	1.009	3817	8.4	48	11.40
4	1.009	3817	8.4	48	11.40
5	1.009	3817	8.4	48	11.40
6	1.009	3817	8.4	48	11.40
7	1.009	3817	8.4	48	11.40
8	1.0028	3919	9.9	47	11.24
9	1.0002	4069	9.9	44	10.76

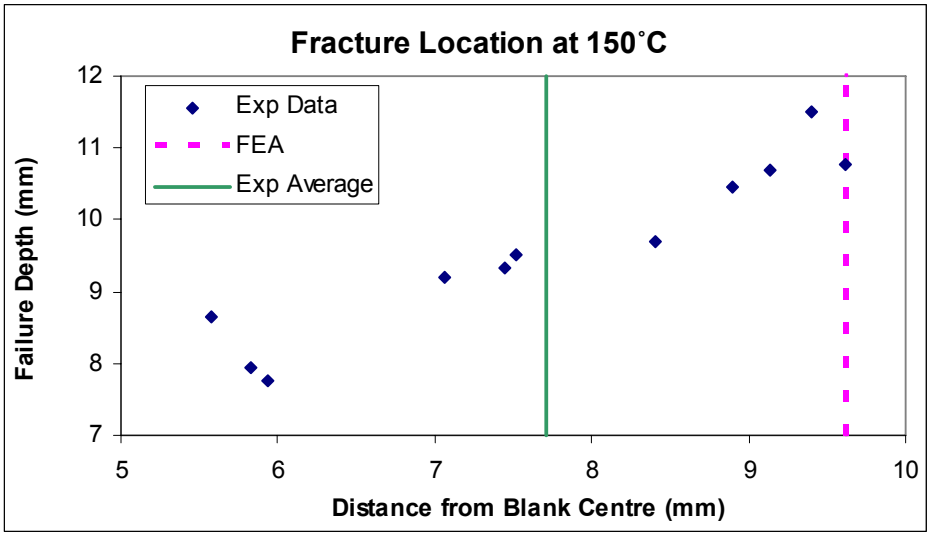

Figure 7-15: Comparison of FEA & Experimental Fracture Location at 150°C

The location of fracture along this path was 9.9mm from the centre of the blank. This value was supported by the fracture location values along the other paths which were similar. Figure 7-15 displays the distance from the centre of the blank where fracture occurred for both the experimental and FEA results. The green line represents the average location of fracture for the experimental results, which was 7.71mm, while the pink dashed line represents the FE predicted location; 9.9mm. The deviation between these two values was 22%. This is quite high but it is important to note that there was a lot of scatter among the experimental results with a deviation of 41% between the highest and lowest values. With this amount of variance it is very difficult to have an accurate finite element prediction of fracture location.

Figure 7-16 compares the punch depths at fracture from the FEA and experimental results at 150°C. The pink dashed line represents the FEA predicted failure at 10.76mm, while the green line is the average failure depth of the experimental results; 9.59mm. The FE model predicted fracture with a 7.5% offset from the highest experimental value and an offset of 27.5% from the lowest. Despite the large difference between the offsets from the highest and lowest experimental values with the FE predicted fracture, the offset between the average experimental failure depth and the FE value was just 10.3%, which was very reasonable considering the scatter in the experimental results. The absence of lubrication meant that the effects of sticking were more prominent in this set of experiments. The magnitude of sticking varied from sample to sample, and together with variances in blank holder temperature created this scatter in the results. The fact that the FE prediction was 27.5% offset from the lowest experimental result and just 10.3% off the average shows that the samples which failed at very low depths were an extreme example of sticking effects in the testing.

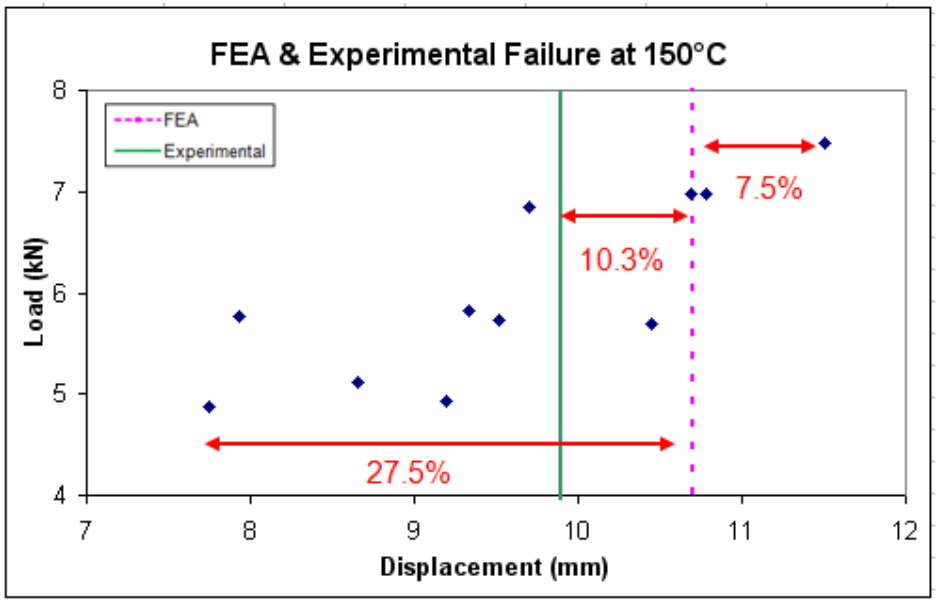

Figure 7-16: FEA & Experimental Punch Depths at Fracture at 150°C

Figure 7-17 illustrates the load curves for the experimental and FEA results. The FE load curve has underestimated the sticking forces in this set of results. The coefficient of friction for the FE model was set very high, 0.6, to simulate the

absence of lubrication, but could not take the sticking effects that occur at high temperatures into account as this was not a feature of the material model. Again the shape of the curve was dictated by the loading profile which needed to apply the load softly at first to reduce the influence of dynamic effects. This did not reflect the experimental results where various amounts of sticking occurred in many cases at the start of the process which resulted in immediate large punch forces.

Apart from the slow start the rest of the profile of the FE curve was similar to the experimental curves but offset at a lower level of force. On average the FEA load at fracture was 17% off the experimental values. Although the load decreased immediately after fracture was detected by the model, it was not true that the occurrence of fracture caused the drop in punch force as it did in reality. The decay of the load curve was determined by the reduction of load applied to the punch by the load profile.

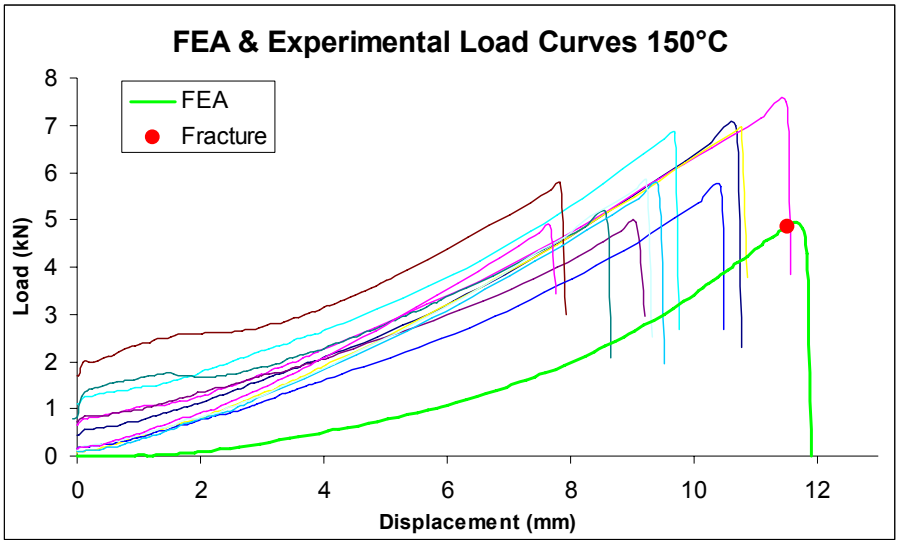

Figure 7-17: FEA & Experimental Load Curves for Results without Lubrication at 150°C

7.4 Implementation of a Failure Range

In experimental work there is usually some variance between the results obtained from multiple tests. The experimental sheet bulging tests performed at both temperatures in this current study were no different. This issue of repeatability with results raises some problems with the finite element method. A finite element model,

when run repeatedly under the same conditions, will produce the same result every time. The FEA model can only predict fracture at a single draw depth, at the point where I reaches unity. In reality each test will result in failure at slightly varying draw depths, so the FEA model cannot correctly predict failure for every single test. Also slight variations in the material properties obtained from numerous tensile tests can also affect the FEA results. For example, using material properties obtained by one tensile test could result in failure being detected (I =1) while using properties from another test could result in borderline failure (I = 0.97). Using the average results from the tensile tests will not eliminate this problem. The only way to allow for all these variances in the FEA model is for the model to detect failure over a range of I values, and not just at a single threshold where I = 1. Therefore it was determined that the FEA model would detect failure where the integral was between 0.9 and 1. This range would introduce a 10% variance in the integral value where fracture could be detected.

7.4.1 Failure Range at 100 Degrees Celsius

Table 7.7 lists the result data where the integral value reached 0.9 at 100°C. This value was detected on paths 1 and 9 at a depth of 10.6mm. It was predicted on the other paths immediately after this depth in the next result set. The element where the integral reached 0.9 was located 6.8mm from the centre of the blank, which is the same location where fracture was predicted in the earlier results for 100°C.

Table7.7: Results where Integral reached 0.9 at 100°C

Path	Integral	Element No.	Location (mm)	Result Set	Depth (mm)
1	0.9168	3857	6.8	33	10.687
2	0.9445	3763	9.9	34	11.087
3	0.933	3889	6.1	34	11.087
4	0.933	3889	6.1	34	11.087
5	0.933	3889	6.1	34	11.087
6	0.933	3889	6.1	34	11.087
7	0.933	3889	6.1	34	11.087
8	0.9215	3915	6.8	34	11.087
9	0.9345	4065	6.8	33	10.687

The depth where the integral reached 0.9 was combined with the fracture results to create a failure range where fracture was predicted between the two depths. The failure range at this temperature was 10.6 – 11.8mm.

The area between the two dashed lines in Figure 7-18 represents the failure range at 100°C and its prediction of fracture in the experimental results. In this case the failure range predicted fracture in 5 out of the 9 experimental samples which is a 55% success rate. This is quite low, but there are various reasons why it was not more successful. Firstly there were deviations in the experimental results due to varying heat transfer effects which influenced the formability of the samples. The effects of heat transfer could not be eliminated from the experiments entirely and hence some samples were formed at slightly different temperatures around 100°C. This meant that the results were scattered and concentrated around two clusters. Secondly the tensile tests for AZ31 at 100°C produced a range of values for the material properties but only single values could be entered as material properties in the finite element model. This meant that the true behaviour of the material could not be entirely represented in the model.

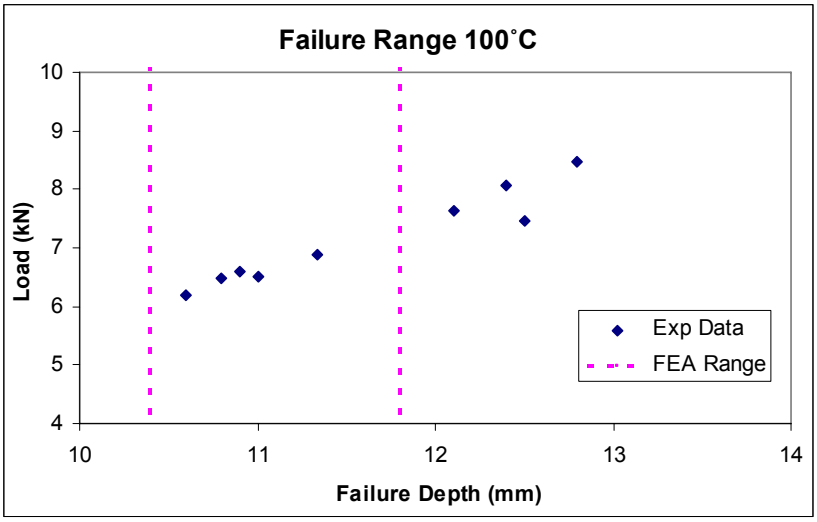

Figure 7-18: Prediction of Fracture using a Failure Range at 100°C

Technically any sample whose depth exceeded the FE model's threshold of failure can be deemed to have fractured according to the model and in this case all the samples have exceeded the threshold value of 10.6mm. But it would be wrong to

then conclude that the model is 100% accurate as it does not give any indication of the depths where these samples eventually fracture. Being able to state that fracture has occurred after a given point is one thing, but to predict a range of failure and to state with confidence that fracture will occur within those limits is a much more accurate prediction and will help to improve the formability of the material.

7.4.2 Failure Range at 150 Degrees Celsius

The first set of experiments at 150°C produced only one failed sample out of eleven which failed at 21.6mm. The FE model did not predict failure but indicated that the threshold of failure was close with a maximum integral value of 0.94 at 22.78mm. With the application of the failure range this now meant that the FE model predicted failure in those samples. It was pointless however to examine a failure range for this set of experiments for two reasons; firstly only one sample failed and there was no failure data available to analyse for the other ten and secondly the integral value in the finite element model did not reach unity, its maximum value was only 0.944.

Table 7.8 lists the FEA results for the second set of experiments at 150°C where the integral threshold of 0.9 was reached. The results show that an integral value of 0.9 was first reached on path number 9 at a depth of 9.96mm, and was located 9.9mm from the centre of the blank. This was the same element where fracture was detected in the earlier set of results where the integral reached unity.

Table 7.8: Results where Integral reached 0.9 at 150°C

Path	Integral I	Element No.	Location (mm)	Result Set	Depth (mm)
1	0.9065	3757	9.9	40	10.12
2	0.9105	3763	9.9	41	10.28
3	0.9012	3889	6.1	42	10.44
4	0.9012	3889	6.1	42	10.44
5	0.9012	3889	6.1	42	10.44
6	0.9012	3889	6.1	42	10.44
7	0.9012	3889	6.1	42	10.44
8	0.9042	3919	9.9	42	10.44
9	0.9379	4069	9.9	39	9.96

Combining the depth where the integral reached 0.9 with the depth where the integral reached unity resulted in a failure range of 9.96 – 10.76mm. This range is shown in Figure 7-19 along with the distribution of the experimental results. The plot shows that the failure range predicted fracture in only 3 out of the 11 samples, and even one of those samples was on the limit. This meant that the range had just a 27% success rate. This was mainly due to the large scatter in the experimental results caused by sticking effects. Although the coefficient of friction in the FE model was very high in order to simulate the lack of lubrication ($\mu = 0.6$), the load profile prevented the model from accurately simulating the effects of sticking between the blank and tooling.

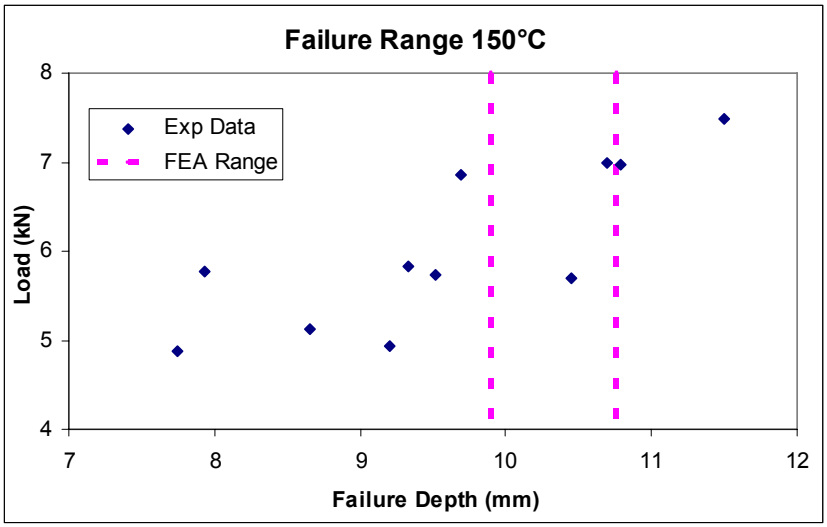

Figure 7-19: Prediction of Fracture using a Failure Range at 150°C

As previously stated the load profile applied the load slowly at the very beginning of the simulation in order to eliminate dynamic effects or "chatter" from the solution. The problem in this case was that in the experiments sticking effects were prominent at the beginning of the process and resulted in high punch forces being exerted on the blank from the very start. (Figure 7-17). This could not be accurately simulated as applying such high loads immediately would make the model unstable. Therefore the simulation did not experience high loads until later on in the process resulting in a late fracture prediction. This was also reflected in Figure 7-19 where 7 out of the 11 samples had failed even before the fracture threshold of 0.9 was reached.

7.5 Statistical Analysis

Previous work by Dar et al. [8] into probabilistic analysis in FEA examined statistical methods that allowed uncertainty and variance to be incorporated in a finite element model. Quite often it is necessary during the design of a component to determine the effects of changing various model parameters on its performance. Material properties are one example of parameters that can have a wide variation of values associated with them and can affect the outcome of an analysis. In finite element modeling however, these properties can only be assigned a unique value that cannot represent the true behaviour of the material over its range of properties. The material properties for the magnesium AZ31 sheets used in this study were determined from tensile tests and produced a range of values whose averages were used in the finite element model. Due to the cumulative nature of the ductile fracture criterion, slight adjustments to these values would result in variations in the prediction of fracture. It was important to examine the response of the model over the entire range of material properties obtained from testing at both temperatures, as it could be determined from the results which property had the greatest influence on the prediction of fracture. Once the most influential material property was determined, a new failure range would then be created using a probabilistic analysis, and this would reflect a more accurate response of the magnesium AZ31 sheets.

In order to determine which property had the most influence on the results it was necessary to perform a factorial analysis to examine the levels of variance of each property on the model. A factorial analysis is a statistical method by which a large number of variables can be analysed efficiently rather than varying one at a time while the others remain fixed. There are a number of factorial analyses available but one of the best known and widely used is the Taguchi Method [79].

7.5.1 Sensitivity Analysis

Using The Taguchi Method, a sensitivity analysis was performed at 100°C and 150°C. In this method the different input parameters are known as factors. Each factor consists of levels which equally divide the range of each factor. Table 7.9 shows the input factors and their corresponding levels at 100°C.

Table 7.9: Input levels and factors used in the factorial analysis at 100°C

100˚C	Level 1	Level 2	Level 3	Level 4
Young's Mod (GPa)	16.9	34.3	51.8	69.2
Yield Stress (MPa)	36.5	69.0	101.5	134.0
Tan Mod (MPa)	984.8	1694.4	2404.0	3113.6

There were three input factors, Young's modulus, yield stress and the tangent modulus which were divided over four levels. These particular properties were chosen as factors as they were key parameters used to define the FE material model. The values used for levels 1 and 4 were the respective lowest and highest values obtained from the tensile tests, while levels 2 and 3 were interpolated values between levels 1 and 4.

Table 7.10: Four level factorial analysis at 100°C

Model	Young's Modulus	Yield Stress	Tan Mod	Max I
1	1	1	1	1.24
2	1	2	2	1.05
3	1	3	3	0.93
4	1	4	4	0.83
5	2	1	2	1.08
6	2	2	1	1.28
7	2	3	4	0.9
8	2	4	3	1.06
9	3	1	3	1.086
10	3	2	4	0.966
11	3	3	1	1.176
12	3	4	2	1.228
13	4	1	4	1.03
14	4	2	3	1.156
15	4	3	2	1.293
16	4	4	1	1.54

In order to study the effects of variance across the four levels, sixteen FE models were built and solved with the configuration and results displayed in Table 7.10. This table represents a Taguchi L16 orthogonal array. In this array each factor level from 1 to 4 appears equally frequently and all combinations of factor levels occur only once in every pair of columns. For a full factorial design it would require 64 simulations to analyse the various combinations between the 3 factors and 4 levels,

but using Taguchi's orthogonal array this is done much more efficiently at a fraction of the computation time.

The effect of varying the material properties affected the prediction of fracture and in some cases fracture was not predicted at all. Therefore it was necessary to study the variance in the maximum integral results rather than the depth at which fracture occurred. The right hand column of Table 7.10 shows the corresponding maximum integral result from each simulation for each different combination of levels.

Table 7.11 shows the transformed maximum integral values, I, for each material property at each level. In this table the maximum integral results for each material property at each level were averaged and transformed using a logarithmic function which transferred the integral values into decibels, which allowed factor effects to be added in an unbiased manner. For example for Young's Modulus level 2, the four integral results from all the models where this level was used (models 5 - 8) were averaged and the result transformed using the transformation function in Equation 7.1 to give a value of -0.33. The transformation from the average maximum integral values ($I_{avg.}$) to the transformed integral (I_T) was given as:

$$I_T = -10 \log_{10} (I_{avg.}^{\ 2}) \qquad (7.1)$$

Table 7.11: Transformed Integral Results at 100°C

100°C	Young's Modulus	Yield Stress	Tan Mod
Level 1	-0.05	-0.45	-1.17
Level 2	-0.33	-0.46	-0.65
Level 3	-0.47	-0.31	-0.24
Level 4	-0.99	-0.66	0.31

The results from Table 7.11 were plotted in Figure 7-20. Each line represents a different factor and the distribution of its results over each level, while the mean of all the transformed results is shown as the dashed line. It should be noted that a less negative number denotes a lower integral value.

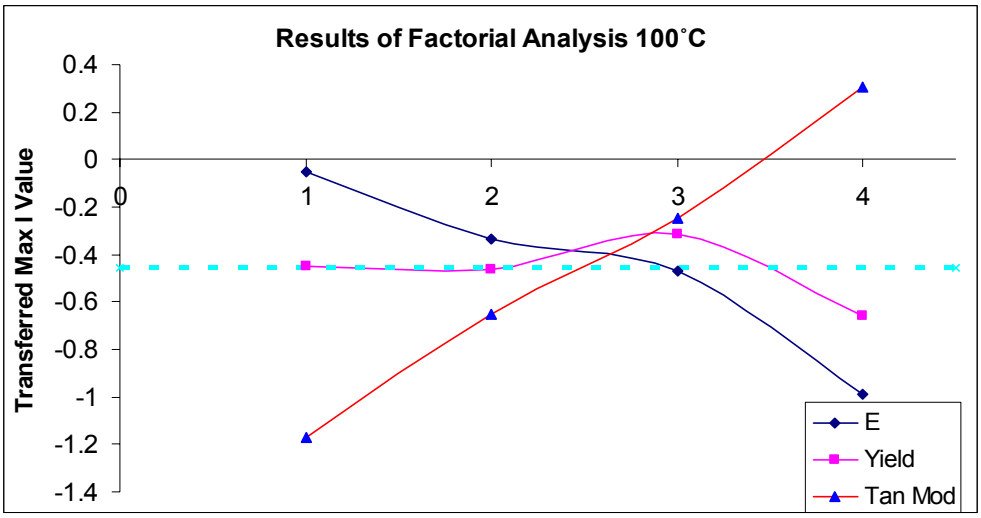

Figure 7-20: Results of the factorial analysis at 100°C

The reasoning behind a factorial analysis is to determine which factor produces the greatest variance from the mean, and it is this factor that has the largest influence on the response of the FE model. From the graph it is clear that the tangent modulus provides the greatest variation from the average results and hence is the most influential property at 100°C. The yield stress provided the least amount of variation and it can be concluded that this property had little effect on the outcome of fracture prediction. It is not surprising that the tangent modulus was the most influential property in terms of fracture prediction as it was used in the finite element model to define the slope of the plastic region of magnesium AZ31.

A factorial analysis was also conducted at 150°C. Table 7.12 lists the factors and levels for the analysis. In a similar fashion to the analysis at 100°C the same material properties were examined here also, but the ranges of values throughout all the levels were much smaller. Once again the highest and lowest levels corresponded to the highest and lowest results from the tensile tests.

Table 7.12: Input levels and factors used in the factorial analysis at 150°C

150˚C	Level 1	Level 2	Level 3	Level 4
Young's Mod (GPa)	24.6	31.1	37.5	44.0
Yield Stress (MPa)	46.0	58.3	70.7	83.0
Tan Mod (MPa)	690.2	853.3	1016.4	1179.5

Table 7.13: Four level factorial analysis at 150°C

Run	Young's Modulus	Yield Stress	Tan Mod	Max I
1	1	1	1	0.784
2	1	2	2	0.9868
3	1	3	3	1.0214
4	1	4	4	0.9961
5	2	1	2	1.0599
6	2	2	1	1.12
7	2	3	4	0.99
8	2	4	3	1.11
9	3	1	3	1.083
10	3	2	4	0.985
11	3	3	1	1.18
12	3	4	2	1.12
13	4	1	4	1.055
14	4	2	3	1.064
15	4	3	2	1.144
16	4	4	1	1.278

Table 7.13 lists the configuration and results from the factorial analysis at 150°C. Once again there were some instances were fracture was not detected in the model and therefore it was more appropriate to compare the maximum integral results rather than the depth at which fracture occurred.

Table 7.14 outlines the transformed maximum integral values, I, for each material property at each level. Similarly to the analysis at 100°C, the maximum integral results for each material property at each level were averaged and transformed using a logarithmic function which transferred the integral values into decibels using the transformation shown in Equation 7.1. The results from Table 7.14 are plotted in Figure 7-21 which illustrates the level of influence of each material property on the response of the FE model.

Table 7.14: Transformed Integral Results at 150°C

150°C	Young's Modulus	Yield Stress	Tan Mod
Level 1	0.23	0.02	-0.37
Level 2	-0.29	-0.16	-0.32
Level 3	-0.38	-0.34	-0.29
Level 4	-0.55	-0.51	-0.028

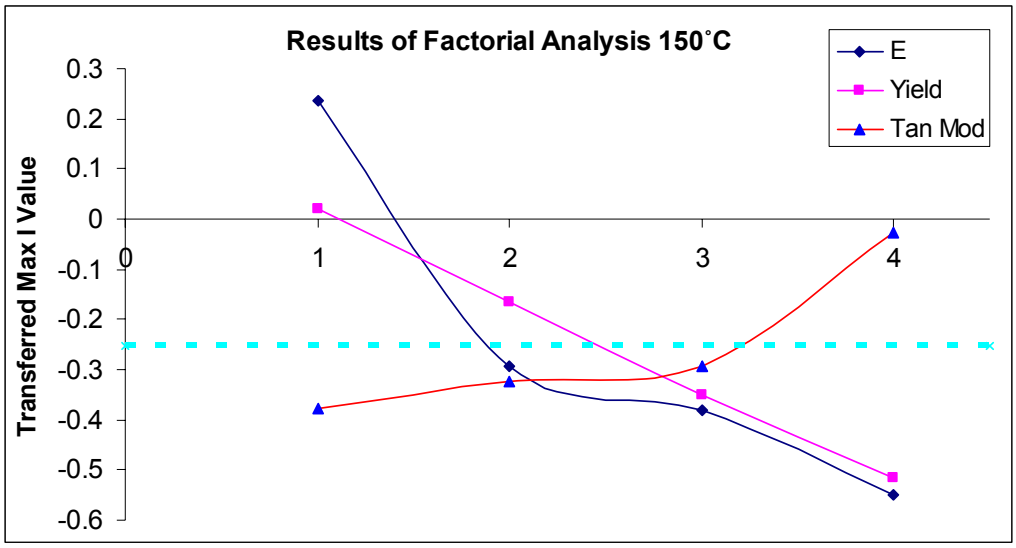

Figure 7-21 Results of the factorial analysis at 150°C

Unexpectedly the results of the factorial analysis show that Young's Modulus was the source of greatest variance in the integral value. The tangent modulus was expected to be the main source of variance again as it represents the slope of the plastic region, which is where fracture will occur. It is important to observe however that the range of values for the tangent modulus at 150°C was considerably smaller than the range at 100°C and this may have contributed to the reduced level of variance in the results. By contrast the range of Young's Modulus values was also reduced, but the level of variance had still increased dramatically when compared to the levels at 100°C. The analysis at 150°C was done under high friction conditions to simulate the absence of lubricant and this may also have increased the influence of Young's Modulus, but generally ductility improves as the temperature increases which means that the plastic region should be more prominent at this temperature, and hence the tangent modulus should become more influential.

7.5.2 Probabilistic Analysis

Probabilistic analysis involves creating a range of inputs for a particularly influential parameter, in this case the tangent modulus at 100°C and Young's Modulus at 150°C, and determining a probabilistic or confidence level in the results based on the response of the model over the range of inputs. At each temperature the model is

solved repeatedly using various input values from the range and the result would provide a statistical distribution of failure at various values. From this distribution a mean ($\bar{x}$) and standard deviation (σ) could be calculated. The standard deviation would provide confidence limits on the range of failure at each temperature. For a confidence level of at least 95%, the data values are between $\bar{x} - 3\sigma$ and $\bar{x} + 3\sigma$. In this instance, over the given range of tangent modulus or Young's modulus values from the tensile tests, there is at least a 95% chance of failure occurring at the draw depths between the two limits.

The application of this method to the current problem was further complicated by the inclusion of the original failure range, where fracture was predicted when I was between 0.9 and 1. So the model was solved repeatedly over the range of input values, and the draw depths where I equaled 0.9 and 1 were recorded. The mean and standard deviation of these values were obtained and the confidence limits were calculated. There were then two sets of confidence levels, one for the draw depths of where I = 0.9 and the other for draw depths where I = 1. Taking the lower limit $\bar{x} - 3\sigma$ where I = 0.9 and the higher limit $\bar{x} + 3\sigma$ where I = 1 provides a confidence level of at least 95% in the failure range itself. It can then be concluded that there is at least a 95% chance that failure will occur when the blank is drawn to a depth within these limits.

Table 7.15 displays the results at 100°C. The column on the left shows the eleven input values for the tangent modulus beginning with the lowest value obtained from tensile testing and ending with the highest. Each value in between was an equal division of the difference between the two. For each simulation the depths were I equaled 0.9 and 1 were recorded together with the location of fracture. The depth where the maximum integral value occurred together with the maximum integral value itself were also recorded. The averages and standard deviations of these results were then calculated and from these the confidence limits were determined.

Table 7.15: Results of Probabilistic Analysis at 100°C

Tan Mod (MPa)	Depth 0.9 (mm)	Depth 1 (mm)	Depth Max (mm)	Max I	Location (mm)
984	10.45	10.81	12.8	1.08	10.6
1197	9.73	10.45	12.6	1.26	9.9
1410	10.07	10.79	12.75	1.21	9.9
1623	10.1	10.81	12.46	1.16	9.9
1836	10.44	11.16	12.21	1.13	8.4
2049	10.81	11.5	12.23	1.04	6.8
2262	10.79	11.8	12	1.02	7.6
2475	11.5		12.05	0.98	10.6
2687			11.8	0.88	7.6
2900			12	0.85	8.4
3113	11.15		12	0.95	6.1
Averages	10.56	11.05	12.26	1.05	8.71
Std Dev	0.176180323	0.16411615	0.097449056		
Con Limits	10.03	11.54	12.56		

The results show that the average depth were the integral reached 0.9 was 10.56mm and where the integral reached unity was 11.05mm. Applying the formulae $\bar{x} - 3\sigma$ to the average depth for 0.9 and $\bar{x} + 3\sigma$ to the average depth where the integral reached unity resulted in a set of confidence limits of 10.03 – 11.54mm. Upon closer examination however it was determined that these limits did not truly reflect the response of the input range. It can be seen from the table that four of the inputs did not result in failure and hence this upper limit did not reflect their response. Examining the maximum integral values it can be seen that the average depth where the maximum occurred was 12.26mm for an average maximum integral value of 1.05. This set of data was more appropriate as it included results from every input, and the average maximum integral value was just over the threshold of failure, 1. Calculating the confidence limit for this set of data and combining it with the result for 0.9 resulted in a set of confidence limits of 10.03 – 12.56mm.

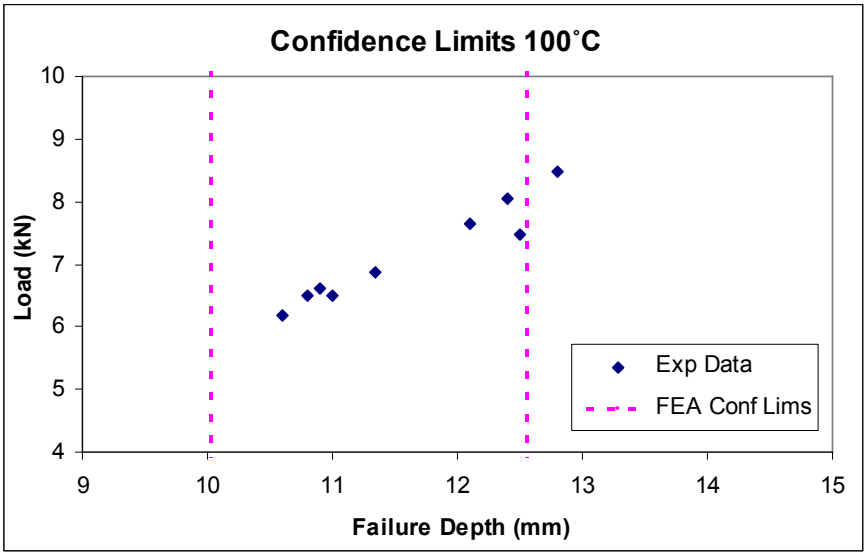

Figure7-22 Confidence Limits at 100°C

Figure 7-22 displays the confidence limits of 10.03 – 12.56mm and their prediction of fracture for the experimental results at 100°C. From the graph it can be seen that fracture was predicted in 8 out of 9 experimental results which was a success rate of 89%. This prediction is a large improvement on the original failure range which predicted fracture in 55% of the samples, but it still does not match the theoretical success rate of 95% that was expected when using the two probabilistic formulae. There are various reasons for this. Firstly the range of input values obtained from the tensile tests may have contained tangent modulus values that were excessively high or low and resulted in an inaccurate range of input values for the probabilistic analysis. Since only one experimental value was not predicted within the confidence limits there is a large probability that increasing the amount of experimental data would reduce the effect of the inaccurate result, thus increasing the percentage of successful fracture prediction.

The average location of fracture predicted by the probabilistic analysis in Table 7.15 was 8.71mm which was 47% in excess of the average experimental fracture location of 5.98mm. The prediction of fracture location in the original FE model was significantly more accurate with a value of 6.8mm which was 13.7% off the average experimental value. The reason the probabilistic analysis produced such an inaccurate value for fracture location was because the location of fracture was

recorded at depths where the maximum integral value was reached. This was done because some inputs did not result in fracture. Some integral values were quite high and occurred at high bulge depths, which in turn increased the distance from the centre where fracture was detected. These values were excessive and influenced the average fracture location value resulting in an inaccurate prediction. Taking the average maximum integral value, 1.05, and calculating the average fracture location where the maximum integral values were less than this number, resulted in an average fracture location of 7.85mm which was 31% off the average experimental value. This value was much more accurate and better reflected the FE models prediction.

Table 7.16 outlines the probabilistic results at 150°C. This time the Young's Modulus was varied over a range of inputs determined by the highest and lowest values from the tensile tests. The results show that fracture was predicted in all the simulations so the results concerning the maximum integral were irrelevant in determining the confidence limits.

Table 7.16: Results of Probabilistic Analysis at 150°C

E (GPa)	Depth 0.9 (mm)	Depth 1 (mm)	Depth Max (mm)	Max I	Location (mm)
24	9.97	11.09	11.57	1.11	9.1
26	9.97	10.7	11.57	1.09	10.6
28	10.6	11.57	11.57	1	8.4
30	9.97	10.7	11.57	1.07	9.9
32	9.73	10.4	11.57	1.09	7.6
34	10.4	11.25	11.57	1.02	10.6
36	9.73	10.29	11.57	1.2	9.9
38	9.73	10.13	11.57	1.13	7.6
40	10.13	10.77	11.57	1.08	8.4
42	9.73	10.29	11.57	1.16	9.9
44	9.74	10.3	11.57	1.11	9.9
Averages	9.973	10.681	11.570	1.096	9.264
Std Dev	0.086	0.132	0.000		
Con Limits	9.715	11.078	11.570		

The average depth where the integral reached 0.9 was 9.97mm while the average depth where fracture was predicted was 10.68mm. The standard deviations show that

there was little scatter in the results from the various inputs. Applying the formulae $\bar{x} - 3\sigma$ to the average depth for 0.9 and $\bar{x} + 3\sigma$ to the average depth where fracture was predicted resulted in a set of confidence limits of 9.715 – 11.078mm.

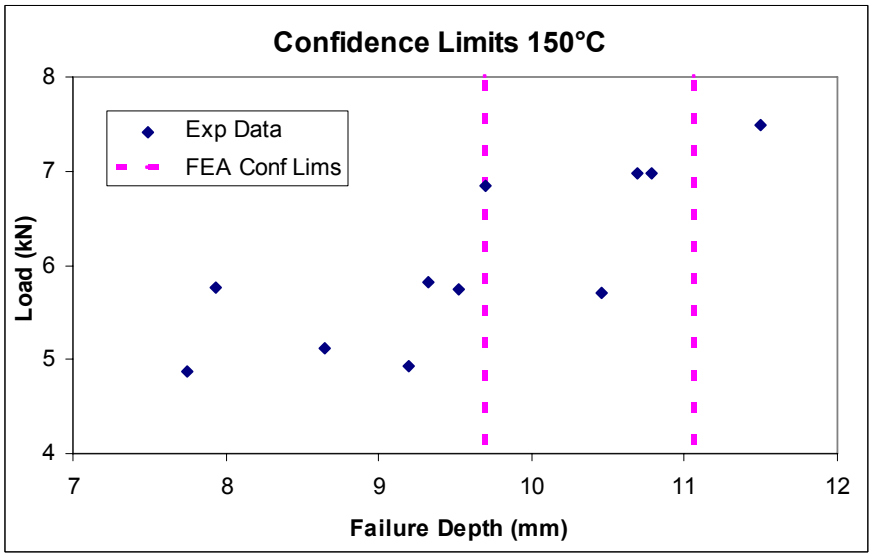

Figure 7-23 Confidence Limits at 150°C

Figure 7-23 illustrates the confidence limits and their prediction of fracture at 150°C. The graph shows that the confidence limits predicted just 4 out of the 11 experimental samples, which is a success rate of only 36%. Although this is an improvement on the original failure range which only predicted fracture in 27% of the samples, this was still a very poor prediction. There were however a number of problems in accurately modeling the experimental conditions.

As discussed previously there was a large scatter among the experimental test results at this temperature due to the varying influence of sticking effects on the samples. In many cases during the experiments at 150°C sticking was observed and there were large frictional forces acting on the blank at the start of the sheet bulging process (Figure 7-18). Due to the nature of the loading profile of the finite element model it was not possible to model the sudden increase in force that resulted from sticking. In this way the finite element model incorrectly calculated stress and strain values which were in fact much higher in reality, and resulted in fracture of the sample, while the FE calculated stress / strain values did not reach a critical level in the finite

element simulation until much later on in the process. That is why many of the experimental samples had already failed before the FE model predicted fracture. Therefore it can be concluded that although the prediction of fracture was inaccurate at this temperature, it was not because of the fracture criterion but by the inability of the FE model to simulate the initial sudden application of forces to simulate sticking effects resulting in excessively low calculations for stress and strain.

The average location of fracture was 9.26mm which was 20% in excess of the average experimental location of fracture, 7.71mm. This was slightly more accurate than the initial finite element model prediction which was 22% off the experimental value. But with the inaccuracies in the prediction of fracture in these models it is irrelevant to draw any conclusions from the comparisons of fracture location. As previously observed, the location of fracture was influenced by the bulge depth, where the fracture occurred further from the centre of the blank as the bulge depth increased. Due to the inability of the FE model to simulate the effects of sticking early in the process, fracture was predicted later than it should have been and thus the distance from the centre where fracture was located was also greater than it would have been in reality.

Chapter 8: Conclusions and Recommendations

Circular blanks of magnesium alloy AZ31 were bulged at 100°C and 150°C. The die was heated using a heater band which transferred heat to the blank holder thus heating that also, while the blanks were heated separately in an oven. There were two key factors which influenced the results of the experimental sheet bulging; heat transfer and sticking.

The temperature of the die was controlled using a thermocouple, while the temperature of the blank holder varied slightly throughout the experiments. It was found that the temperature of the blank holder could exceed the temperature of the die by up to 15°C. The effects of heat transfer were more visible in the results at 100°C where the forming depths at fracture of the samples were concentrated into three clusters (Figure 7-2) two of which were reasonably close to each other while the third was significantly higher. It was noted that the samples which fractured at a higher punch depth had been in the rig longer than the other samples, thus allowing the temperature of the blank holder to rise above 100°C and so influence the result. The samples in the third cluster were formed at temperatures around 110°C - 115°C and hence did not demonstrate the behaviour of the material at 100°C. These samples were omitted from the comparisons with the FEA results.

The results at 100°C demonstrate some shortcomings in the experimental apparatus and the sensitivity of magnesium AZ31. Although in some of the experiments the temperature of the blank holder was only a few degrees higher than that of the die its effects were clearly visible. Magnesium AZ31 has a high coefficient of thermal conductivity (96 W/m-k) [3] which make it more sensitive to any changes in temperature. It is therefore recommended that any hot forming of magnesium AZ31 have very tight temperature control. While it is impossible to eliminate the effects of heat transfer entirely, it is possible to reduce it to an acceptable level. In the case of the sheet bulging apparatus used in this study the heater band was turned off in between experiments to enable the blank holder to lose its excess heat. This method worked reasonably well with the majority of results being within 2mm of each other. The more extreme results were from experiments were the blank holder mechanism

was not aligned properly and required adjustment thus increasing the length of time the blank was in the rig.

Two sets of sheet bulging experiments were conducted at 150°C. The first set of experiments produced only one fractured sample and hence a second set of experiments using different conditions was required. The magnesium blanks could be bulged up to 24mm before they were fully drawn into the die and it is interesting to note that a temperature increase of 50°C could dramatically improve the formability of the material to such an extent that it would not fracture. But it is specious reasoning to assume that the formability of magnesium alloy is improved drastically at 150°C as this improved formability is only true for the apparatus used in this current study with its particular dimensions, and such a dramatic increase in formability may not be observed if a different punch or die diameter had been used in the experiments.

A second set of experiments at 150°C were conducted without lubrication to induce fracture in the samples. Sticking of the blank to the blank holder was observed during the experiments and this was reflected in the results which showed large initial punch forces indicating high friction and sticking. The magnitude of the sticking effects varied from sample to sample and this produced a large scatter in the results).

The sheet bulging experiments were simulated using the finite element software ANSYS LS-DYNA. ANSYS incorporates various yield criteria such as Von Mises which can accurately predict yield in a material but are extremely ineffective in predicting fracture. Therefore Oyane's ductile fracture criterion was implemented into the FE model to predict fracture in the blank. Fracture was detected at the point where Oyane's integral was equal to one.

The initial results at 100°C compared favourably with the experimental results with just a 2.3% deviation between the average experimental result and the FEA prediction of fracture (Fig 7-9). The FEA prediction was also within 12.1% of all the experimental results. This implies very good accuracy in the FE model, however five samples failed before the FE model predicted fracture and so technically the FE model only predicted that six out of the eleven samples had failed.

Two FE models were built to simulate the two sets of experiments at 150°C; one set with lubrication and the other set without. The first model which simulated the sheet bulging with lubrication predicted that fracture would not occur, which is validated by the experimental results where only one out of the eleven samples failed. The model initially gave a prediction of fracture which when further investigated proved to be a wrinkle in the blank, although no wrinkling occurred in any of the experimental samples. The high strains involved in the wrinkling of the blank exaggerated the value of the Oyane's integral and gave a false impression that fracture had been predicted. This anomaly was detected when comparing the results from the different paths on the blank. The results of the path where the wrinkle occurred stood out from the other results in terms of its location and the late stage of its occurrence in the draw. This model shows the importance of having multiple paths in the blank to compare results against. Had the elements not been organised into paths where the location of fracture could be easily determined it would have been very difficult to spot the wrinkle and it would have been assumed that fracture had occurred.

The results from the second FE model, which simulated the experiments conducted without lubricant at 150°C, appear to compare favourably to the experimental results, with a 10% deviation between the FE prediction of fracture and the average experimental result. This comparison however was very misleading as the FE model was largely very liberal with its fracture prediction with eight out of the eleven experimental samples failing before the FE model predicted that they would. This was due to the initial sticking effects observed in the experiments which could not be modelled properly in ANSYS LS-DYNA, which led to the FE model underestimating the stresses and strains involved with sticking, and therefore the model predicted failure later than it had occurred in reality. Further research in this area could examine the limitations of load profiles in finite element software and devise methods on how to model suddenly applied forces.

A failure range based on a 10% variation on the threshold of fracture was introduced where failure was detected in the blank when the integral value was between 0.9 and 1. The objective of the failure range was to determine an upper and lower limit of

failure in between which it was predicted that fracture would occur. This range provided a more conservative threshold of failure at I = 0.9, which technically predicted failure in all the samples at 100°C as their failure depths exceeded the depth at which the integral reached 0.9, yet it is wrong to conclude from this that the range was completely accurate as only 55% of the samples failed within the range itself (Fig 7-18).

The problems with modeling sticking effects at 150°C were still apparent as only 27% of the samples failed within the predicted failure range. Even with the conservative failure threshold at I = 0.9, seven samples had already failed before this threshold was reached. Although the failure range made a poor prediction of fracture it would be unwise to make any decisive conclusions regarding the ability of the FE model to predict fracture. The inability of the FE model to accurately model the initial sticking effects which were observed throughout this set of experiments has greatly affected the models prediction of fracture. Ironically the first set of experiments, conducted with lubrication, where only one sample failed provides a better insight into the performance of the fracture prediction of the FE model.

The definition of a material model in ANSYS is limited by the fact that only one specific value can be entered for each material property. The results from the tensile tests produced a range of values for each property at each temperature. Varying these values in the FE model could have a large impact on the prediction of fracture. A factorial or sensitivity analysis was conducted at 100°C and 150°C to determine which material property had the greatest influence on the FE model. The Taguchi Method was employed to create an orthogonal array of input models which would greatly reduce the number of simulations required to solve each permutation of the various material property values.

At 100°C it was found that the tangent modulus provided the greatest variation in the calculation of the Oyane integral. This seemed logical as fracture generally occurs in the plastic region of a material's stress strain curve, and the tangent modulus was used to define this region in the FE model. At 150°C the Young's Modulus was found to be the most influential property. It was expected that the tangent modulus would again be found to be the most influential property at this temperature, however

the range of values for the tangent modulus used in the analysis at 150°C was much smaller than that used at 100°C, and reduced the variation in the results.

The most influential properties as determined by the sensitivity analysis were then used in a probabilistic analysis at each temperature. From the probabilistic analysis a new failure range was created which would provide a theoretical confidence level of 95% in the results. Although the probabilistic analysis showed an improvement in the prediction of fracture from the original failure range at both temperatures, 89% at 100°C and 36% at 150°C, the theoretical confidence level of 95% successful prediction was not reached at either temperature. Although it can be argued that at 100°C since only one experimental result did not fall within the confidence limits, it is probable that with more experimental data the 95% confidence level could be reached.

The location of fracture in the blank was reasonably predicted at both temperatures. At 100°C the FE model predicted fracture at 6.8mm from the centre of the blank, which was 11% off the average experimental value of 6.1mm. At 150°C the FE model predicted the location of fracture as being 9.59mm from the centre of the blank which was 22% greater than the average experimental value, 7.71mm. Results for fracture location from the probabilistic analysis show that at 100°C the results were less accurate, 42% off the experimental value, while at 150°C the results were approximately the same, 20%. After examining the results of the probabilistic analysis it was concluded that the fracture location from the initial FE models were more accurate.

8.1 Recommendations for Future Work

The following suggestions are based on observations made during the experimental testing and finite element modeling of the sheet bulging process:

- A copper based lubricant delivered in an oil solution was applied to the samples to reduce friction during forming. Although the lubricant was suitable for temperatures up to 1100°C the oil base would evaporate at 150°C

producing a large amount of smoke that would make it very difficult to centre the blank holder plate and apply the blank holder force (BHF). Other authors [53-54, 62, 77-78] have applied various lubricants to AZ31 blanks but no recommendation for a specific lubricant has yet been made. Perhaps a further investigation into the performance of various lubricants at high temperatures would produce a good recommendation.

- Design a blank holder mechanism that is self centering and can apply a force to the blank very quickly, perhaps through fluid pressure, with the ability to vary the BHF during forming. This would eliminate the visibility problems caused by the evaporating lubricant base and help reduce the effects of heat transfer as seen in the experiments at 100°C where critical time was wasted aligning the blank holder plate.

- Develop a load profile to model the sudden application of high loads that simulate sticking effects in high temperature forming. This would be similar to the work of Maker and Zhu [73] who developed a load profile to simulate the deep drawing process.

- Perform friction testing of magnesium AZ31 at high temperatures, under dry and lubricated conditions, to determine the coefficient of friction at various forming temperatures. These values can be used to more accurately model the contact conditions between the blank and tooling at each temperature.

- Examine alternative methods for establishing a range of failure, possibly basing the lower limit on a percentage of the forming depth at fracture.

- Build a material database documenting the formability of magnesium AZ31 under various geometric and loading parameters. By implementing a ductile fracture criterion together with a failure range and statistical methods, this database should help reduce the unpredictability surrounding the high temperature forming of magnesium alloys.

References

[1] Chandrasekin, M. and Yong, J.M.S. "Effect of Materials and Temperature on the Forward Extrusion of Magnesium Alloys" Journal Materials & Sci Eng A 381 (2004) pp 308-319.

[2] Luminium Alum. and Mg Info Centre, [Online]. Chemical Composition of AZ31B, (2007) <http://www.luminum.com/data/dcompositionmg.html>, (accessed 28 October 2007)

[3] Matweb Material Property Database, [Online]. Material Properties AZ31, (1996 – 2007) <http://www.matweb.com/search/DataSheet.aspx?MatID=12315&ckck=1> (accessed 25 September 2007)

[4] Wang, X.Y. "Sheet Bulging Experiment With a Viscous Pressure-Carrying Medium" Journal of Materials Processing Technology, Vol. 151 (2004) pp. 340–344.

[5] Namoco, C.S., Iizuka, T., Sagrado, R.C., Takakura, N., Yamaguchi, K. "Experimental and Numerical Investigation of Restoration Behavior of Sheet Metals Subjected to Bulging Deformation" Journal of Materials Processing Technology, Vol. 177 (2006) pp. 368–372.

[6] Oyane, M., Sato, T., Okimoto, K., Shima, S. "Criteria for Ductile Fracture and Their Applications", Journal. Mech. Work. Technology, Vol. 4 (1980) pp. 65-81.

[7] Han, H.N. and Kim, K.H. "A Ductile Fracture Criterion in Sheet Metal Forming Process" Journal of Materials Processing Technology, Vol. 142 (2003) pp. 231–238.

[8] Dar, F.H., Meakin, J.R., Aspden, R.M. "Statistical Methods in Finite Element Analysis" Journal of Biomechanics, Vol. 35 (2002) pp. 1155–1161.

[9] Mordike, B.L. and Ebert, T. "Magnesium Properties—Application—Potential", Journal of Materials Science and Engineering A302 (2001) pp.37–45.

[10] Furuya, H., Kogiso, N., Matunaga, S., Senda, K. "Applications of Magnesium

Alloys for Aerospace Structure Systems", Materials Science Forum, Vol. 350 (2000) pp.341–348.

[11] Chen, F.K., Huang, T.B., Chung, C.K. "Deep Drawing of Square Cups with Magnesium Alloy AZ31 Sheets", Journal Mach. Tools & Manuf., Vol. 43 (2003) pp. 1553-1559.

[12] Watanabe, H., Tsutsui, H., Mukai, T., Kohzu, M., Tnabe, S., Higashi, K. "Deformation Mechanism in a Coarse-grained Mg–Al–Zn Alloy at Elevated Temperatures", International Journal of Plasticity, Vol.17 (2001) pp.387–397.

[13] Kaneko, J., Sugamata, M., Numa, M., Nishikawa, Y., Takada, H. "Effect of Texture On the Mechanical Properties and Formability of Magnesium Wrought Materials", Journal of Japan Institute of Metals, Vol. 64 (2000) pp. 141–147.

[14] Mwembela, A., Konopleva, E.B., McQueen, H.J. "Microstructural Development in Mg Alloy AZ31 During Hot Working", Scripta Materialia, Vol. 37 (1997) pp. 1789–1795.

[15] Takuda, H., Fujimoto, H., Hatta, N. "Modeling on Flow Stress of Mg–Al–Zn Alloys At Elevated Temperatures", Journal of Materials Processing Technology, Vol. 80 (1998) pp. 513–516.

[16] Doege, E. and Droder, K. "Sheet Metal Forming of Magnesium Wrought Alloys-Formability and Process Technology", Journal of Materials Processing Technology, Vol. 115 (2001) pp. 14–19.

[17] Gaines, L., Cuenca, R., Stodolsky, F., Wu. S. "Potential Applications of Wrought Magnesium Alloys for Passenger Vehicles", US Government Report, Argonne National Laboratory, Illinois, USA (1995)

[18] Song, G. "Recent Progress in Corrosion and Protection of Magnesium Alloys", Advance Engineering Materials, Vol. 7 (2005) pp. 563-586.

[19] Shi, Z., Song, G., Atrens, A. "Control of Biodegradation of Biocompatable

Magnesium Alloys", Journal of Corrosion Sci., Vol. 48 (2006) p. 1939.

[20] Birss, V., Xia, S., Yue, R., Rateick, R.G. "Characterization of Oxide Films Formed On Mg-based WE43 Alloy Using AC/DC Anodization in Silicate Solutions", J. Electrochem. Soc., Vol. 151 (2004). Pp. 1-10.

[21] Montemor, M.F., Simoes, A.M., Ferreira, M.G.S., Carmezim, M.J. "Composition And Corrosion Resistance of Cerium Conversion Films on the AZ31 Magnesium Alloy and its Relation to the Salt Anion", Journal Applied Surface Science, (2007)

[22] Rudd, A.L., Breslina, C.B., Mansfeld, F. @The Corrosion Protection Afforded by Rare Earth Conversion Coatings Applied to Magnesium", Corrosion Sci., Vol. 42 (2000) p275.

[23] Montemor, M.F., Simoes, A.M., Carmezim, M.J. "Characterization of Rare-Earth Conversion Films Formed on AZ31 Magnesium Alloy and its Relation with Corrosion Protection", Applied Surface Science, Vol. 253, (2007) pp. 6922-6931

[24] International Magnesium Association, [Online]. (2007), <http://www.intlmag.org> (accessed 3 October 2007)

[25] Barnes. L., Communication with Lee Barnes, Spectrulite Consortium (Nov.16, 1994)

[26] Yoshihara, S., MacDonald, B.J., Nishimura, H., Yamamoto, H., Manabe, K. "Optimisation of Magnesium Alloy Stamping with Local Heating and Cooling Using the Finite Element Method" Journal of Materials Processing Technology, Vol. 153 – 154 (2004) pp. 319–322

[27] El-Morsy, A. and Manabe, K. "Finite Element Analysis of Magnesium AZ31 Alloy Sheet in Warm Deep-Drawing Process Considering Heat Transfer Effect" Materials Letters, Vol. 60 (2005) pp. 1866-1870.

[28] Samekto, H., Roll. K. “Finite Element Analysis of Superplastic Forming Process Using LS-DYNA”, 4th European LS-DYNA Users Conference, Germany, (2003)

[29] Higashi K. et al. “An Experimental Investigation of the Superplastic Forming Behaviour of a Commercial Al-bronze”, Metallurgical Transaction, Vol. 21A (1990) pp. 2957-2966.

[30] Draugelates, U. and Schram A. “Superplasticity of Magnesium Base Alloys” Mater. wissen. Werkst.tech. ISSN 0933-5137, Vol. 30 (1999) pp. 628-632.

[31] Senthil Kumar, V.S., Viswanathan, D., Natarajan S. “Theoretical Prediction and FEM Analysis of Superplastic Forming of AA7475 Aluminium Alloy in Hemispherical Die” Journal of Materials Processing Technology, Vol. 173 (2006) pp. 247–251.

[32] Liew, K.M., Tan, H., Tan. M.J. “Finite Element Modeling of Superplastic Sheet Metal Forming for Cavity Sensitive Materials” Journal of Engineering Materials and Technology, Vol. 125 (2003) pp. 256–259.

[33] Bampton, C. C. and Raj. R. “Influence of Hydrostatic Pressure and Multiaxial Straining on Cavitation in a Superplastic Aluminium Alloy” Acta Metall., Vol. 30 (1982) pp. 2043-2053.

[34] Bampton, C. C. et al. “Control of Superplastic Cavitation by Hydrostatic Pressure”, Metall. Trans. A, Vol. 14 (1983) pp. 583-591.

[35] Lian, J. and Suery, M. “Effect of Strain Rate Sensitivity and Cavity Growth Rate on Failure of Superplastic Material” Mater. Sci. Technol. Vol. 2 (1996) pp. 1093-1098.

[36] Zhou, D.J. and Lian, J. “Numerical Analysis of Superplastic Bulging for Cavity Sensitive Materials” Int. J. Mech. Sci., Vol. 29 (1987) pp. 565-576.

[37] Du, Z., Li, M., Wu, S. “Numerical Computation of Cavity Damage and Failure

During the Superplastic Deformation of Sheet Metal" Journal of Materials Processing Technology, Vol. 57 (1996) pp. 298-303.

[38] Freudenthal, A.M. "The Inelastic Behaviour of Engineering Materials and Structures", John Wiley & Sons, New York, (1950)

[39] Rice, J.R. and Tracey, D.M. "On Ductile Enlargement of Voids in Triaxial Stress Fields", Journal of the Mechanics and Physics of Solids, Vol. 17 (1969) pp. 201–217.

[40] Cockroft, M.G. and Latham, D.J. "Ductility and the Workability of Metals", J. Inst. Met. Vol. 96 (1968) pp.33-39.

[41] Clift, S.E., Hartley, P., Sturgess, C.E.N., Rowe. G.W. "Fracture Prediction in Plastic Deformation Processes", Int. J. Mech. Sci. Vol. 32 (1990) pp. 1-17.

[42] Brozzo, P., Deluca, B., Rendina, R. "A New Method for the Prediction of Formability in Metal Sheets", Proceedings of the Seventh Biennial Conference of IDDRG on Sheet Metal Forming and Formability, (1972).

[43] Bressan, J.D. and Williams, J.A. "The Use of a Shear Instability Criterion to Predict Local Necking in Sheet Metal Deformation", Int. J. Mech. Sci. 25, (1983) p.155

[44] Yang, Y.Y. and Yu, Z.Q. "A New Ductile Fracture Criterion and its Application to the Prediction of Forming Limit in Deep Drawing" ICPNS'04, Shanghai, (2004) pp. 1507-1510.

[45] Dey, S., Borvik, T., Hopperstad, O.S., Langseth, M. "On the Influence of Fracture Criterion in Projectile Impact of Steel Plates" Journal of Computational Materials Science, Vol. 38 (2006) pp. 176–191.

[46] Johnson, G.R. and Cook, W.H. "Fracture Characteristics of Three Metals Subjected to Various Strains, Strain Rates, Temperatures and Pressures", Engineering Fracture Mechanics, Vol. 21 (1985) pp. 31–48.

[47] Børvik, T., Hopperstad, O.S., Berstad, T., Langseth, M. "Computational Model of Viscoplasticity and Ductile Damage for Impact and Penetration", European Journal of Mechanics & Solids Vol. 20 (2001), pp. 685–712.

[48] Dey, S., Børvik, T., Hopperstad, O.S., Leinum J.R. Langseth, M. "The Effect of Target Strength on the Perforation of Steel Plates Using Three Different Projectile Nose Shapes", International Journal of Impact Engineering, Vol. 30 (2004) pp. 1005–1038.

[49] Bai, Y. and Dodd, B. "Adiabatic Shear Localization. Occurrence, Theories and Applications", Pergamon Press, Oxford (1992).

[50] Dodd, B. and Bai, Y. "Ductile Fracture and Ductility with Applications to Metalworking", Academic Press Inc., London (1987).

[51] Hosford, W.F. and Caddell, R.M. "Metal Forming (Mechanics and metallurgy)", Prentice Hall Inc., New Jersey (1993).

[52] Goijaerts, A. M., Govaert, L. E., Baaijens, F. P. T. "Prediction of Ductile Fracture in Metal Blanking", Journal of Manufacturing Science and Engineering, Vol. 122 (2000) pp. 476–483.

[53] Takuda, H., Mori, K., Fujimoto, H., Hatta, N. "Prediction of Forming Limit in Bore-Expanding of Sheet Metals Using Ductile Fracture Criterion", J. Mater. Process. Tech., Vol. 92-93 (1999) pp.433-438.

[54] Takuda, H., Mori, K., Hatta, N. "The Application of Some Criteria for Ductile Fracture to the Prediction of the Forming Limit of Sheet Metals", J. Mater. Process. Tech., Vol. 95 (1999) pp. 116-121.

[55] Ozturk, F. and Lee, D. “Analysis of Forming Limits Using Ductile Fracture Criteria” J. Mater. Process. Tech., Vol. 147 (2004), pp. 397- 404.

[56] Keeler, S.P. and Backofen, W.A. “Plastic Instability and Fracture in Sheets Stretched Over Rigid Punches”, Trans. Am. Soc. Met. Vol. 56, (1963) pp. 25-48.

[57] Chen, F.K. and Huang T.B. “Formability of Stamping Magnesium Alloy AZ31 Sheets”, Journal Mater. Process Tech. Vol. 142 (2003) pp 643-647.

[58] Goodwin, G.M. “Application of Strain Analysis in Sheet Metal Forming Problems”, Metall. Ital. 60 (1968) pp. 767-771

[59] Mielnik, E.M. “Metalworking Science and Engineering”, McGraw Hill, New York, (1991)

[60] Hosford, W.F. and Duncan, J.L. “Sheet Metal Forming, A Review”, J.O.M. Vol. 51 (1999) pp. 39- 44

[61] Siegert, K., Jager, S., Vulacn, M. “Pneumatic Bulging of Magnesium AZ31 Sheet Metals at Elevated Temperature”, CIRP Ann. Manufact. Technol. Vol. 52 pp. 241– 244.

[62] Takuda, H., Yoshii, T., Hatta, N. “Finite Element Analysis of the Formability of a Magnesium-based Alloy AZ31 Sheet”, J. Mater. Process. Tech., Vol. 89 - 90 (1999) pp.135-140

[63] Manabe, K. 2005 Personal communication with Ken-ichi Manabe, Tokyo Metropolitan University (2005)

[64] Takuda, H., Mori, K., Takakura, N., Yamaguchi, K. “Finite Element Analysis of Limit Strains in Biaxial Stretching of Sheet Metals Allowing for Ductile Fracture”, Int. J. Mech. Sci., Vol. 42 (2000) pp. 785-798.

[65] MacDonald, B.J, "Finite element Simulation of Complex Bulge forming Processes", PhD. Thesis, (2000) Dublin City University, Ireland.

[66] Bathe, K.J., "Finite Element Procedures", Prentice-Hall International, UK, (1996).

[67] ANSYS Home, [Online]. ANSYS Release Notes, (2007) <http://www.kxcad.net/ansys>, (accessed 26 May 2007)

[68] Hill, R., "The Mathematical Theory of Plasticity", Oxford University Press, (1950), p. 318

[69] ShoDor Computational Science Ed., (1996 – 2007), [Online] The Stress Strain Curve, <http://www.shodor.org/~jingersoll/weave/tutorial/node4.html> (accessed 10 October 2007)

[70] Yoshihara, S., (2007) "Test Result Data", [E-mail] Message to D. Hunt (david.hunt3@mail.dcu.ie), 24th June 2006.

[71] Galvin, E. "An Experimental and Numerical Investigation into a Deep Drawing Process", M.Sc. Thesis, (2006), Dublin City University, Ireland.

[72] Browne, M.T. "Optimisation of the Variables Present in the Deep-Drawing Process", PhD. Thesis, (2000), University of Limerick, Ireland.

[73] Maker, B.N. and Zhu, X., "Input Parameters for Metal Forming Simulation using LS- DYNA", Livermore Software Technology Corporation, (April 2000).

[74] RoyMech, (2007), [Online] Coefficients of Friction, < http://www.roymech.co.uk/Useful_Tables/Tribology/co_of_frict.htm#coef> (accessed 20 September 2007)

[75] Nielsen, K.B., “Sheet Metal Forming Simulation using Explicit Finite Element Methods”, PhD. Thesis, (1997), Aalborg University, Denmark.

[76] Yoshihara, S., Yamamoto, H., Manabe, K., Nishimura, H. “Formability Enhancement in Magnesium Alloy Deep Drawing by Local Heating and Cooling Technique”, J. Mater. Process. Tech., Vol. 143 (2003) pp. 612-615.

[77] Yoshihara, S., Manabe, K., Nishimura, H. “Effect of Blank Holder Force Control in Deep-Drawing Process of Magnesium Alloy Sheet”, J. Mater. Process. Tech., Vol. 170 (2005) pp. 579-585.

[78] Yoshihara, S., Nishimura, H., Yamamoto, H., Manabe, K. “Formability Enhancement in Magnesium Alloy Stamping Using a Local Heating and Cooling Technique: Circular Cup Deep Drawing Process”, Mater. Process. Tech., Vol. 142 (2003) pp. 609-613

[79] Taguchi, G. “System of Experimental Design”, UNIPUB Kraus International Publications, New York (1987).